

https://dspace.org/

Preparation of Cu2ZnSnS4/N-MWCNTs nano-hybrid systems for potential application in dye-sensitized solar cells as counter electrode

Mxakaza, Lineo Florence

2020

https://hdl.handle.net/10539/30983

Mxakaza, Lineo Florence (2020) Preparation of Cu2 ZnSnS 4/N MWCNTs nano-hybrid systems for potential application in dye-sensitized solar cells as counter electrode, University of the Witwatersrand, Johannesburg, <http://hdl.handle.net/10539/30983>

Downloaded from a DSpace repository. https://dspace.org/

Preparation of Cu_2ZnSnS_4/N-MWCNTs nano-hybrid systems for potential application in dye-sensitized solar cells as counter electrode



WITS UNIVERSITY

LINEO FLORENCE MXAKAZA

A dissertation submitted to the Faculty of Science, University of the Witwatersrand, in partial fulfilment of the requirements for the degree of Master of Science in Chemistry

Supervisors: Dr. Zikhona Tetana & Prof. Nosipho Moloto

March, 2020

Declaration

I declare that this dissertation is my own, unaided work. It is being submitted for the degree of Master of Science at the University of the Witwatersrand, Johannesburg. This work has not been submitted previously for any degree or examination at any other University.



_____ 28/08/2020_____

Lineo Mxakaza (Candidate) Date



_____ 28/08/2020_____

Dr. Zikhona Tetana (Supervisor) Date



_____ 28/08/2020_____

Prof. Nosipho Moloto (Co-Supervisor) Date

Abstract

Solar energy is deemed as one of the best alternative energy sources to fossil fuels because it is abundant and renewable. Dye-sensitized solar cells (DSSCs) are one of the photovoltaic devices that have attracted much of attention due to easy fabrication methods and relatively low-cost of production. DSSC architecture includes a photoanode sensitized with an organic dye, an electrolyte and a counter electrode (CE). Platinum is a common CE material because of it has high catalytic activity and conductivity. However, platinum is a noble metal and has a low surface area and alternative materials that result in comparable or even higher power conversion efficiencies are sort after. Cu_2ZnSnS_4 (CZTS) has been extensively studied as an absorber layer in p-n junction solar cells because it exhibits high absorption coefficient and low band gap. CZTS has recently been reported to have promising electro-catalytic activity properties that can be utilized in DSSC as CE material to facilitate the reduction of the electrolyte. However, poor results have been obtained thus far. Several articles have attributed the poor performance of CZTS as a CE material to its poor electron transport properties since it is a semiconductor. To counteract this shortcoming, CZTS can be coalesced with other high electron conductivity materials such as carbon nanotubes. Nitrogen doped multi-walled carbon nanotubes (N-MWCNTs) have been reported to exhibit high electron conductivity although they are poor electro-catalysts, due to defects caused by the nitrogen atoms and these defects can also be utilized in the formation of CZTS/N-MWCNTs hybrid systems. To counteract the poor catalytic behaviour of MWCNTs and poor conductivity of CZTS, a nanocomposite mixture of CZTS/N-MWCNT can be employed to provide good catalytic activity and electron transfer. Herein, we report on the colloidal synthesis and characterization of CZTS nanoparticles in oleylamine (OLA). The successful synthesis of CZTS was confirmed by X-ray diffraction (XRD) and Raman spectroscopy where the kesterite phase was obtained. The X-ray photoelectron spectroscopy (XPS) also confirmed the formation of CZTS. The transmission electron microscope (TEM) images showed polydispersed particles. To overcome the polydispersity, digestive ripening was undertaken. Ripening for 2hrs resulted in a more monodispersed sample. To ensure good anchoring of nanoparticles on the surface of the N-MWCNTs, ligand exchange was done where shorter and bidentate ligands were used namely pyridine (py), mercaptopropionic acid (MPA) and ethanedithiol (EDT). The py was used as it a traditionally use exchange ligand while MPA and EDT with two functional groups could bind to the nanoparticle surface with one group and have the other available for anchorage to the N-MWCNTs. The XRD and

TEM images showed that the long-chained OLA capped particles were far better than the py, MPA and EDT capped particles. The N-MWCNTs were synthesized using the chemical-vapour deposition method. The nitrogen doping was confirmed by XPS and the bamboo morphology observed on the TEM images. Raman spectroscopy also showed that more defects were present after doping. The ex-situ synthesis method that involves sonicating the CZTS and N-MWCNTs in dimethyl formamide was employed to prepare the nanocomposites. Raman spectroscopy and the TEM images confirmed the interaction between these two materials hence the formation of the nano-hybrids/nanocomposites. Cyclic voltammetry using nanocomposite ink fabricated on glassy carbon electrode in the I^-/I_3^- electrolyte was run to determine the maximum reduction peak current of the various weight percent ratios of CZTS and N-MWCNTs in the CZTS/N-MWCNTs nanocomposites. The CZTS/NMWCNTs (0.3 ratio) was found to exhibit the highest reduction peak current, and relatively low potential and was therefore deemed as the best of all the ratios and a possible Pt CE material alternative.

Dedication

For my gorgeous daughter, Lesedi Makoae

Acknowledgments

- My greatest thanks are due to my supervisors, Dr. Tetana and Prof. Moloto, in equal measure for giving me an opportunity to be part of their incredible research groups, for their instrumental advice, guidance and for pushing me to realize my outmost capabilities, both as a researcher and an individual. Being led by such young and ambitious black women is sure to rub off on anyone that comes within their vicinity.

- I would also like to thank African Materials and Engineering Network (AMSEN) for funding this research work, the consistent financial support you granted me made this work far less stressful than it would have otherwise been. Thank you for also sponsoring the conferences I attended during this research, which without any doubt have helped me grow through interacting with other young researchers.

- This work is the fruit of the input of my fellow colleagues and seniors, particularly Ms. Ngubeni, Mr. Ndala, Dr. Machogo-Phao, Dr. Airo, Ms. Kolokolo, Mr. Shimbuwa and Mr. Nkabinde, who showed me the way around the lab, gave me ideas on how to improve my work and helped me with analysis and data interpretation of my samples.

- I would also like to express my gratitude to Dr. Rudolf Erasmus, Mr. Thomas Mongwe and Dr. Mbuso Mlambo for Raman analysis, and Wits MMU for training and access to their TEM, XRD, SEM and AFM characterization instruments. I would also like to thank the School of Chemistry, Dow Company and NRF for settling my Honours fees, if not for that, I would not have been able to register for Master`s degree.

- Lastly, my sincerest gratitude goes to my family, both in Lesotho and South Africa, for their prayers, consistent support and encouragement during this period, particularly my grandmother. A special thanks to my partner, Khali Makoae, for encouraging and pushing me to register for postgraduate degree and the unwavering support he showed me during my studies. I am highly indebted to the Almighty God for the gift of life and health he has granted me, and for sparing my life in a car accident I was involved in during my research period.

List of presentations

- Oral presentation at the Catalysis and Materials (CATMAT) seminar on 6 April 2018 held at the University of the Witwatersrand, School of Chemistry.

- Poster presentation at the NanoSMAT Africa conference held in Cape Town from the 19th-23rd November 2018. Awarded second price for the NanoSMAT Africa and Springer Nature poster competition.

- Poster presentation at the 43rd National Convention of South African Chemical Institute (SACI) conference held at CSIR-ICC, Pretoria from the 2nd-7th December 2018.

- Oral presentation at the CATMAT seminar held on 8 February 2019 at the School of Chemistry, University of the Witwatersrand.

- Poster presentation at the DST-NRF Centre of Excellence in Strong Materials student presentation workshop held at the University of the Witwatersrand on 21st May 2019.

- Poster presentation at the South African Institute of Physics (SAIP) conference held in Limpopo from the 8th - 12th July 2019.

- One-minute flash presentation at the 10th Cross-Faculty Postgraduate Symposium held at the University of the Witwatersrand on the 3rd September 2019.

- Poster presentation at the SANi 9thNanoscience`s Young Researcher`s Symposium (NYRS) held at Future Africa, University of Pretoria, Pretoria on the 12th November 2019. Awarded second best poster under MSc category.

- Oral presentation at the 10th International Conference of the African Material Research Society (AMRS) conference held at Nelson Mandela African Institute of Science and Technology, Arusha, Tanzania from the 10th – 13th December 2019.

Table of contents

Declaration i
Abstract ii
Dedication iv
Acknowledgments v
List of presentations vi
Table of contents vii
List of figures x
List of abbreviations xiii
Structure of thesis xv
Chapter 1 : General background 1
1.1 Introduction 1
1.2 Problem statement 1
1.3 Rationale 3
1.4 Aims and objectives 3
1.5 References 4
Chapter 2 : Literature review 7
2.1 Dye-sensitized solar cells 7
2.1.1 Architecture 7
2.1.1.1 Photoanode 8
2.1.1.2 Electrolyte 9
2.1.1.3 Counter electrode 9
2.1.2 Working principle of dye-sensitized solar cells 14
2.1.3 Characterization of dye-sensitized solar cells 15
2.1.4 CZTS/MWCNTs nanocomposites in DSSCs 16
2.2 References 16
Chapter 3 : Preparation and acid treatment of N-MWCNTs 23
3.1 Doped carbon nanotubes 23
3.2 Synthesis methods of carbon nanotubes 24
3.3 Growth mechanism of carbon nanotubes 25
3.4 Materials and methods 26
3.4.1 Chemicals 26
3.4.2 Catalyst synthesis 26

3.4.3 Preparation and acid functionalization of N-MWCNTs 27
3.4.4 Characterization 28
3.5 Results and discussion 28
3.5.1 Phase composition and thermal stability of Fe-Co/$CaCO_3$ 28
3.5.2 Structural analysis of as prepared N-MWCNTs and fN-MWCNTs 30
3.5.3 Thermal stability and purity analysis of N-MWCNTs and functionalized N-MWCNTs 32
3.5.4 Morphology evaluation of N-MWCNTs and functionalized N-MWCNTs 33
3.5.5 Elemental composition analysis of functionalized N-MWCNTs 34
3.6 Conclusions 36
3.7 References 37
Chapter 4 : Colloidal synthesis, surface and structural modification of Cu_2ZnSnS_4 41
4.1 Introduction 41
4.1.1 Colloidal synthesis 41
4.1.2 Digestive ripening 42
4.1.3 Ligand exchange 43
4.2 Materials and methods 44
4.2.1 Chemicals 44
4.2.2 Colloidal synthesis of CZTS 44
4.2.3 Digestive ripening of CZTS 45
4.2.4 Ligand exchange of OLA capped CZTS 45
4.2.5 Characterization 46
4.3 Results and discussion 47
4.3.1 Structural properties of CZTS 47
4.3.2 Surface evaluation of CTZS 49
4.3.3 Elemental composition of as-synthesized CZTS 51
4.3.4 Morphology evaluation of CZTS 54
4.3.5 Digestive ripening of CZTS 55
4.3.6 Ligand exchange 57
4.3.7 Effect of ligand exchange on the morphology and structural properties of CZTS 60
4.4 Conclusions 62
4.5 References 63

Chapter 5 : Preparation of Cu_2ZnSnS_4/fN-MWCNTs nanocomposites and their electrochemical properties 68
5.1 Introduction 68
5.1.1 Hybrid materials 68
5.1.2 Cyclic voltammetry 69
5.2 Materials and methods 70
5.2.1 Chemicals 70
5.2.2 Preparation of Cu_2ZnSnS_4/fN-MCNTs nanocomposites 71
5.2.3 Counter electrode fabrication 71
5.2.4 Electrochemical measurements 71
5.2.5 Characterization 72
5.3 Results and discussion 72
5.3.1 Structural, morphology and elemental composition of nanocomposites 72
5.3.2 Proposed mechanism for interaction of fN-MWCNTs and CZTS 78
5.3.3 Electrochemical properties of CE materials 79
5.3.4 Composite charge transmission model 85
5.4 Conclusions 85
5.5 References 86
Chapter 6 : Conclusions and future work 90
Appendix 92

List of figures

Chapter 1

Figure 1.1: South African electricity generation from various energy sources [11]. 2

Chapter 2

Figure 2.1: Schematic diagram showing components of the dye-sensitized solar cell [10]. 8

Figure 2.2: (a) Schematic diagram illustrating basis of CZTS development and (b) kesterite and (c) stannite tetragonal crystal structures of $Cu_2ZnSn(S/Se)_4$ [45]. 11

Figure 2.3: Some of the carbon allotropes: (a) graphene, (b) graphite (c) carbon nanotube, (d) fullerene (C_{60}) and (e) fullerene (C_{90}) (Structures generated by Nanotube Modeler). 13

Figure 2.4: Common carbon nanotubes (a) single-walled carbon nanotube (b) multi-walled carbon nanotubes (generated by Nanotube Modulator). 14

Figure 2.5 : Typical photocurrent-voltage (*J-V*) curve of a dye-sensitized solar cell. 16

Chapter 3

Figure 3.1: Bonding configurations of nitrogen in multi-walled carbon nanotubes post doping [10]. 24

Figure 3.2: Probable growth processes for carbon nanotubes on metal particles; (a) tip and (b) base growth [27]. 26

Figure 3.3: Schematic diagram depicting the microwave synthesis procedure for the catalyst. 27

Figure 3.4: CVD method set-up used to prepare N-MWCNTs. 28

Figure 3.5: (a) X-ray diffraction pattern and (b) Thermogram of Fe-Co catalyst supported on $CaCO_3$. 30

Figure 3.6: X-ray diffraction patterns of acid treated and as-synthesized N-MWCNTs. 31

Figure 3.7: Raman spectra of acid treated and as-synthesized N-MWCNTs. 32

Figure 3.8: (a) Thermograms and (b) corresponding derivative profiles of acid treated and as-prepared N-MWCNTs. 33

Figure 3.9: (a) and (b) SEM images and (c), (d) and (e) TEM micrographs of nitrogen doped multi-walled carbon nanotubes prior and post acid functionalization. 34

Figure 3.10: (a) XPS survey spectrum of acid treated N-MWCNTs and (b)-(d) high-resolution spectra of carbon, nitrogen and oxygen, respectively. 36

Chapter 4

Figure 4.1: Growth mechanism of the nanoparticles during hot injection colloidal synthesis. 41
Figure 4.2: Schematic diagram depicting preparation procedure of CZTS and color change upon addition of precursors. 45
Figure 4.3: Schematic diagram depicting target ligand switching. 46
Figure 4.4: X-ray diffraction pattern of CZTS. 48
Figure 4.5: Raman spectrum of as-synthesized CZTS. 49
Figure 4.6: FTIR spectra of (a) OLA capped CZTS and (b) pure OLA. 50
Figure 4.7: ^{1}H NMR spectrum of (a) pure OLA and (b) OLA capped CZTS. 51
Figure 4.8: XPS survey spectrum of CZTS nanoparticles synthesized in OLA. 52
Figure 4.9: XPS high-resolution spectra of (a) copper, (b) zinc, (c) tin and (d) sulfur. 53
Figure 4.10: XPS high-resolution spectra of (a) carbon, (b) zinc, (c) oxygen and (d) nitrogen. 54
Figure 4.11: (a) TEM and (b) SEM images of the as-synthesized CZTS. 55
Figure 4.12: EDX spectrum and corresponding SEM image of CZTS. 55
Figure 4.13: Effect of digestive ripening time on the shape and size distribution of CZTS. ..56
Figure 4.14: FTIR spectra of OLA capped CZTS and CZTS after ligand exchange. 57
Figure 4.15: (a) ^{1}H NMR of spectra of pure pyridine and (b) corresponding pyridine capped CZTS. 58
Figure 4.16: ^{1}H NMR spectra of (a) pure EDT and corresponding (b) EDT capped CZTS. ..59
Figure 4.17: ^{1}H NMR spectra of pure MPA and MPA capped CZTS. 60
Figure 4.18: XRD patterns of CZTS nanoparticles before and after ligand exchange. 61
Figure 4.19: TEM images of (a) OLA-CZTS, (b) MPA-(CZTS), (c) py-CZTS and (d) EDT-CZTS. 62

Chapter 5

Figure 5.1: (a) Electrode fabrication by drop casting and (b) electrochemical measurement set up. 72
Figure 5.2: X-ray diffraction patterns of CZTS and CZTS/fN-MWCNTs with increasing fN-MWCNT concentration. 73
Figure 5.3: TEM micrographs of CZTS/fN-MWCNTs with increasing carbon nanotube mass ratio of (a) 0.15, (b) 0.2 (c) 0.25 and (d) 0.3. 74
Figure 5.4: Raman spectra of as synthesized (a) CZTS, (b) fN-MWCNTs and (c) CZTS/fN-MWCNTs (0.15) nanocomposite. 75
Figure 5.5: XPS survey spectrum of CZTS/fN-MWCNTs (0.15). 76

Figure 5.6: XPS high-resolution spectra of (a) copper, (b) zinc, (c) tin and (d) sulfur. 77
Figure 5.7: XPS high-resolution spectra of (a) carbon, (b) oxygen and (c) nitrogen. 78
Figure 5.8: Cyclic voltammograms of Pt at increasing scan rate. 79
Figure 5.9: Cyclic voltammograms of CZTS/fN-MWCNTs nanocomposites at increasing scan rates. 80
Figure 5.10: Stability evaluation of the prepared composites in iodide/triiodide-based electrolyte after 60 cycles at 100 mV/s. 81
Figure 5.11: Relationship between the number of CV scans of the composites at the obtained current density. 82
Figure 5.12: Change in reducing ability of the CZTS/fN-MWCNTs with increasing carbon nanotube concentration at 50 mV/s. 82
Figure 5.13: Electrochemical performance comparison of CZTS/fN-MWCNTs (0.3) with (a) CZTS and fN-MWCNTs and (b) bare-GC and Pt. 84
Figure 5.14: A schematic diagram depicting the possible electron transport route in the CZTS/N-MWCNTs nanocomposite CE [27]. 85

Appendix

Figure A4.1: Full ^{1}H NMR spectrum of pyridine capped CZTS. 92

List of abbreviations

CE	Counter electrode
CHNS	Elemental analysis
CV	Cyclic voltammetry
CVD	Chemical vapor deposition
Cu	Copper
Cu_2ZnSnS_4	Copper zinc tin sulfide
CZTS	Cu_2ZnSnS_4
Deg.	Degrees
DMF	*N*, *N*-Dimethyl formamide
DMSO	Dimethyl sulfoxide
DRA	Digestive ripening agent
DSSCs	Dye-sensitized solar cells
EDS	Energy Dispersive X-ray spectroscopy
EDT	1, 2-Ethanediamine
FF	Fill factor
fN-MWCNT	Functionalized nitrogen doped multi-walled carbon nanotube
FTIR	Fourier-transform infrared spectroscopy
FTO	Fluorine doped tin oxide
HOMO	Highest occupied molecular orbitals
^1H	Proton
I^-	Iodide
I_3^-	Triiodide
A_D/A_G ratio	Raman peak area ratio of D band to G band
LUMO	Lowest unoccupied molecular orbitals
MPA	3-Mercaptopropionic acid
N-MWCNT	Nitrogen doped multi-walled carbon nanotube
NMR	Nuclear magnetic resonance
OLA	Oleylamine
PXRD	Powder X-ray diffraction
ppm	parts per million
Pt	Platinum
QDSSCs	Quantum dot sensitized solar cells

SEM	Scanning electron microscopy
TEM	Transmission electron microscopy
TGA	Thermal gravimetric analysis
4IR	Fourth industrial revolution
PCE	Power conversion efficiency
PV	Photovoltaic
α	alpha
β	beta
γ	gamma

Structure of thesis

- **Chapter 1** provides the basis and motivation behind preparation of CZTS/N-MWCNTs nanocomposite materials as possible platinum free counter electrodes in dye-sensitized solar cells with the aim of addressing the current and future energy demands by exploiting the solar radiation.

- **Chapter 2** is a detailed description of the individual components of dye-sensitized solar cells as well as various materials that can be employed in each component to assist in the maximum photon to energy conversion. The properties of CZTS and N-MWCNTs are explained in detail and how these properties make them suitable candidates for DSSCs counter electrodes. Finally, the working principle of DSSCs as well as how the performance parameters of the cell can be evaluated is described.

- **Chapter 3** firstly details the chemical vapor deposition technique as a synthesis procedure for N-MWCNTs including the proposed growth mechanism of the nanotubes when this method is employed and ultimately the conditions used to prepare the nanotubes. The effectiveness of acid washing the prepared N-MWCNTs to remove the catalyst is then determined by comparison of the structural and composition analysis results of N-MWCNTs before and post washing.

- **Chapter 4** describes the colloidal hot injection growth mechanism of CZTS nanoparticles in OLA. This chapter also describes post synthesis modification of the structure and surface of the OLA capped CZTS by digestive ripening and ligand exchange, respectively.

- **Chapter 5** presents the importance and benefits that come about mixing two materials with different properties to utilize both their properties in order to counteract the shortcomings of another. The preparation procedure for CZTS/N-MWCNTs nanocomposites of various ratios is highlighted followed by their corresponding electrochemical measurements.

- **Chapter 6** underlines the conclusions deduced from this research work and likely future work that can be done in line with the exploitation of CZTS/N-MWCNTs nanocomposites as possible Pt free dye-sensitized solar cell counter electrodes.

Chapter 1 : General background

1.1 Introduction

The escalating global energy demand, probable depletion of fossil fuels and climate change due to global warming has rendered vast research towards alternative, renewable and environmentally benign energy sources [1]. Biomass, hydropower, geothermal, solar and wind energies are such renewable energy resources with solar energy reported to be the cheapest and most abundant [2]. The challenge that still stands for scientists is to develop photovoltaic (PV) devices that are both cost-effective and have high power conversion efficiency (PCE) to harvest the solar radiation. Currently, commercial PV devices with 26 % efficiency are based on monocrystalline and polycrystalline silicon wafers [3] and are referred to as first generation solar cells. Silicon is an indirect band gap material, therefore; a thick layer of its perfect crystals is mandatory for such efficiencies, thus effecting a high production cost of these solar cells [4].

The high cost of first-generation solar cells then prompted the development of thin film solar cells based on semiconductors deposited on various substrates as alternative PV devices and are referred to as second generation solar cells. The semiconductor materials known include $CuIn(Ga)Se_2$ (CIGS), CdTe/CdS and amorphous-silicon and these show a higher energy absorption efficiency relative to monocrystalline and polycrystalline silicon [5]. Thin film second generation solar cells require far less material, however, they have low PCE, are made from toxic and limited materials resulting in restricted commercialization [6]. Third generation solar cells are aimed at improving the efficiency while reducing the production cost of PV devices. Indium and tellurium in second generation solar cell materials are rare while gallium is toxic, therefore third generation solar cells are designed to replace these elements with abundant, low toxic elements such as Zn and Sn in $Cu_2(ZnSn)S_4/Se$. Dye-sensitized solar cells (DSSCs) are one of the third generation solar cells that offer vast advantages over other solar cells due to their relatively easy manufacturing technologies, acceptable efficiency, lower cost and printable fabrication methods [7], [8]. The first DSSC was reported in 1991 by Grätzel and O`Regan with PCE of 7.1 % [9] and since then, many improvements on DSSC components aimed at elevating their efficiency have surfaced.

1.2 Problem statement

In the recent years, South Africa has been awakened to the danger of its major reliance of the energy sector on fossil fuel following power cuts. In his report, the regional managing

director of SENER Southern Africa, Siyabonga Mbanjwa highlighted the need for South Africa to have a balanced energy mix from all energy sources [10]. As of 2016, 85.7 % of the electricity generated in South Africa came from fossil fuel combustion as shown in **Figure 1.1** [11]. To meet the energy demand as the economic growth improves and prevent future power cuts due to limited coal, the energy supply should therefore be diversified across all the energy sources [12].

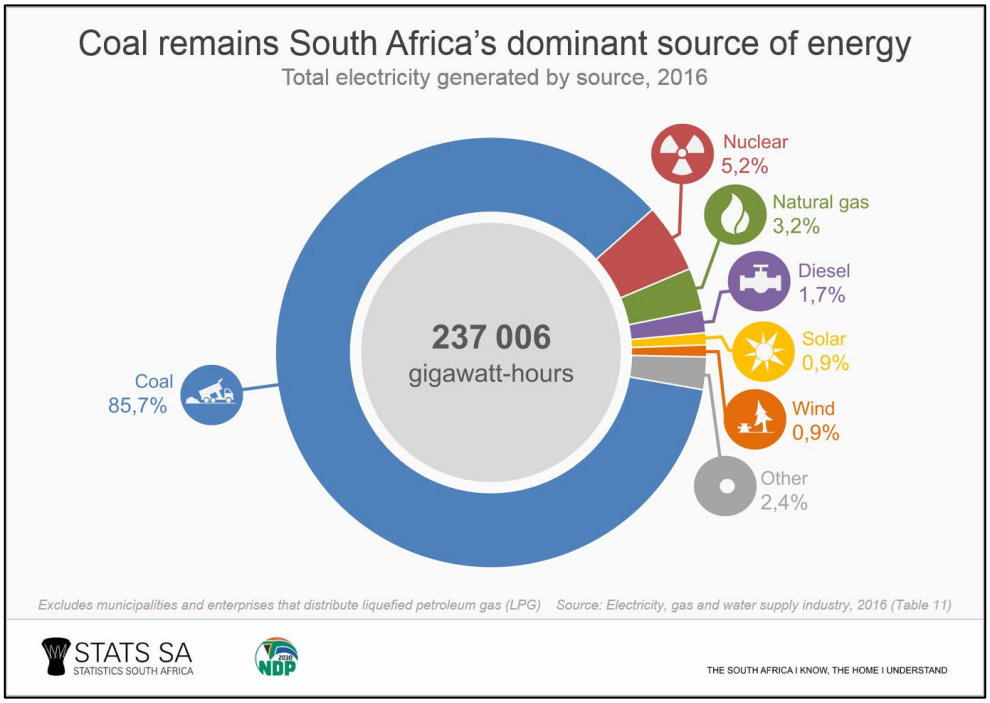


Figure 1.1: South African electricity generation from various energy sources [11].

Coal based energy also poses a threat to the environmental health of the planet by emitting greenhouse gases and land reform resulting in climate change and damage to the natural bionetwork of the planet [13]. One approach of answering this shift in energy supply chain can be through harvesting the solar radiation to produce usable energy. The earth receives a total energy of around 3×10^{26} J/year which is free for utilization by photovoltaic (PV) technology. Current PV devices that are in the market are based on monocrystalline and polycrystalline silicon and are quite costly. To make commercialization of PV devices economically feasible, optimizing thin film based solar cells is crucial. DSSCs offer easy fabrication methods and replacing the platinum (Pt) counter electrode (CE) in DSSCs with a material that has comparable or a higher electro-catalytic ability, while offering more chemical stability and cost-effective constituent elements could in fact render them economically sustainable.

1.3 Rationale

Fourth industrial revolution (4IR/ Industry 4.0) first surfaced in Germany in 2011 and is a phenomenon that targets the introduction of high technology policies of robots that mimic human behaviour, automated cars and passive machinery to moderate CO_2 discharge, usage of raw materials and their cost [14], [15]. This shift aims to preserve the earth for future generations [16] and discussions such as alternative, environmentally friendly energy sources such as solar exploitation to produce energy are at the forefront. DSSCs are a plausible solution to the existing energy demand if their production cost can be lessened while also improving their power-to-energy conversion. One such approach can be swapping the conventional noble Pt counter electrode with more abundant, yet harmless material that has similar properties to Pt. Pt has a reasonable catalytic activity towards the common I^-/I_3^- DSSCs electrolyte, however, it is not without any flaws. Pt is oxidized to PtI_4 upon exposure to I^-/I_3^- [17], [18]. Carbides [19], conducting polymers [20], [21], inorganic and carbon-based materials as well as composites made from either of these compounds have shown potential as optional CE materials because of their good conducting and reducing abilities [22]–[26]. Chalcogenides, in particular Cu_2ZnSnS_4 (CZTS) , has earth abundant, relatively cheap constituent elements, good electron transport, easily optimizable synthesis methods and decent electro-catalytic activity [27], [28]. However, only 4.5% PCE was obtained when this material was employed as a CE in a study conducted by Nemala et al. and attributed this to the not so good conductivity of CZTS [27]. Coalescing CZTS with highly conductive carbon compounds such as graphene and carbon nanotubes improved the DSSC efficiency [25], [27], [29]. To counteract the poor conductivity of CZTS and poor catalytic behaviour of N-MWCNTs, CZTS/MWCNT hybrid can be employed as a CE to provide phenomenal catalytic activity and electron transfer in DSSCs. For this research, a hybrid of CZTS and highly conductive and defected nitrogen-doped multi-walled carbon nanotubes (N-MWCNTs) CE was prepared and corresponding reducing capacity on the DSSC electrolyte was evaluated.

1.4 Aims and objectives

The prime goal of this study was to prepare nanocomposite materials of various weight percentages of Cu_2ZnSnS_4 and nitrogen-doped multi-walled carbon nanotubes, evaluate and compare their reduction capabilities towards the I^-/I_3^- electrolyte to Pt counter electrode.

These aims were achieved by implementation of the following objectives:

- Microwave synthesis of bimetallic Fe-Co/$CaCO_3$ catalyst using iron and cobalt nitrate salts.
- Synthesis of N-MWCNTs by chemical vapor deposition (CVD) method using acetonitrile and acetylene as nitrogen and carbon sources, respectively, over Fe-Co/$CaCO_3$ catalyst.
- Colloidal synthesis of Cu_2ZnSnS_4 using oleylamine (OLA) as the reaction medium and surfactant.
- Optimize digestive ripening time of the Cu_2ZnSnS_4 nanoparticles in excess digestive ripening agent (OLA).
- Perform ligand exchange of OLA with 3-Mercaptopropionic acid (MPA), ethanedithiol (EDT) and pyridine on OLA capped Cu_2ZnSnS_4.
- Prepare CZTS/N-MWCNTs nanocomposite systems through sonication in *N, N*-dimethyl formamide (DMF).
- Study and compare the reduction performance of the composite materials deposited on glassy carbon electrode towards the I^-/I_3^- to Pt using cyclic voltammetry.

1.5 References

[1] J. Gong, J. Liang, and K. Sumathy, "Review on dye-sensitized solar cells (DSSCs): Fundamental concepts and novel materials," *Renewable and Sustainable Energy Reviews*, vol. 16, no. 8, pp. 5848-5860, 2012.

[2] R. Eisenberg and D. G. Nocera, "Preface: Overview of the forum on solar and renewable energy," *Inorganic Chemistry*, vol. 45, no. 4, pp. 1880-1880, 2006.

[3] M. A. Green, K. Emery, Y. Hishikawa, W. Warta, and E. D. Dunlop, "Solar cell efficiency tables (version 45)," *Progress in Photovoltaics: Research and Applications*, vol. 23, pp. 1-9, 2013.

[4] M. P. Suryawanshi, G. L. Agawane, S. M. Bhosale, S. W. Shin, P. S. Patil, J. H. Kim and A. V. Moholkar, "CZTS based thin film solar cells: A status review," *Materials Technology*, vol. 28, no. 1–2, pp. 98-109, 2012.

[5] S. Sharma, Bulkesh Siwach, S. K. Ghoshal, and D. Mohan, "Dye sensitized solar cells: From genesis to recent drifts," *Renewable and Sustainable Energy Reviews*, vol. 70, pp. 529-537, 2017.

[6] B. E. Hardin, H. J. Snaith, and M. D. McGehee, "The renaissance of dye-sensitized solar cells," *Nature Photonics*, vol. 6, no. 3, pp. 162-169, 2012.

[7] M. Ye, X. Wen, M. Wang, J. Iocozzia, N. Zhang, C. Lin and Z. Lin, "Recent advances

in dye-sensitized solar cells: From photoanodes, sensitizers and electrolytes to counter electrodes," *Materials Today*, vol. 18, no. 3, pp. 155-162, 2015.

[8] M. Grätzel, "The advent of mesoscopic injection solar cells," *Progress in Photovoltaics*, vol. 14, pp. 156-172, 2013.

[9] B. O. Regan and M. Grätzel, "A low-cost, high-efficiency solar cell based on dye-sensitized colloidal TiO_2 films," *Nature*, vol. 353, pp. 737-740, 1991.

[10] S. Mbanjwa, "Diversification of SAS energy energy mix is the answer to future coal shortarges," *News24*, 2018. Accessed on 4th March, 2020

[11] Electricity, gas and water supply industry. Statistics South Africa, 2016. Accessed on 4th March, 2020

[12] V. Ndlovu and R. Inglesi-Lotz, " Positioning South Africa`s energy supply mix internationally: Comparative and policy review analysis," *Journal of Energy in Southern Africa*, vol. 30. no. 2, pp. 14-27, 2019.

[13] Modi, V., McDade, S., Lallement, D. and and Saghir, J. (2005). Energy services for the millennium development goals. World Bank: New York, NY.

[14] R. Berger, "Industry 4.0: The new industrial revolution-How Europe will succeed," 2014.

[15] V. Zamagni, "Franco Mosconi, The new European industrial policy: Global competitiveness and the manufacturing renaissance," 2016.

[16] N. Carvalho, O. Chaim, E. Cazarini, and M. Gerolamo, "Manufacturing in the fourth industrial revolution: A positive prospect in sustainable manufacturing," *Procedia Manufacturing*, vol. 21, pp. 671-678, 2018.

[17] E. Olsen, G. Hagen, and S. Eric Lindquist, "Dissolution of platinum in methoxy propionitrile containing LiI/I_2," *Solar Energy Materials and Solar Cells*, vol. 63, no. 3, pp. 267-273, 2000.

[18] A. Kay and M. Grätzel, "Low cost photovoltaic modules based on dye sensitized nanocrystalline titanium dioxide and carbon powder," *Solar Energy Materials and Solar Cells*, vol. 44, no. 1, pp. 99-117, 1996.

[19] M. Wu, X. Lin, T. Wang, J. Qiu, and T. Ma, "Low-cost dye-sensitized solar cell based on nine kinds of carbon counter electrodes," *Energy and Environmental Science*, vol. 4, no. 6, pp. 2308-2315, 2011.

[20] H. Sun, Y. Luo, Y. Zhang, D. Li, Z. Yu, K. Li and Q. Mang, "In situ preparation of a flexible polyaniline/carbon composite counter electrode and its application in dye-sensitized solar cells," *Journal of Physical Chemistry C*, vol. 114, no. 26, pp. 11673-

11679, 2010.

[21] Q. Li, J. Wu, Q. Tang, Z. Lan, P. Li, J. Lin and L. Fan, "Application of microporous polyaniline counter electrode for dye-sensitized solar cells," *Electrochemistry Communications*, vol. 10, no. 9, pp. 1299-1302, 2008.

[22] T. Hino, Y. Ogawa, and N. Kuramoto, "Preparation of functionalized and non-functionalized fullerene thin films on ITO glasses and the application to a counter electrode in a dye-sensitized solar cell," *Carbon*, vol. 44, no. 5, pp. 880-887, 2006.

[23] S. Cingarapu, Z. Yang, C. M. Sorensen, and K. J. Klabunde, "Synthesis of indium nanoparticles: Digestive ripening under mild conditions," *Inorganic Chemistry*, vol. 50, no. 11, pp. 5000-5005, 2011.

[24] R. Bajpai, S. Roy, P. Kumar, P. Bajpai, N. Kulshrestha, J. Rafiee, N. Koratkar and D. S. Misra "Graphene supported platinum nanoparticle counter-electrode for enhanced performance of dye-sensitized solar cells," *ACS Applied Materials and Interfaces*, vol. 3, no. 10, pp. 3884-3889, 2011.

[25] H. Chen, J. Wang, C. Jia, J. Mou, and L. Zhu, "Highly efficient dye-sensitized solar cell with a novel nanohybrid film of Cu_2ZnSnS_4-MWCNTs as counter electrode," *Applied Surface Science*, vol. 422, pp. 591-596, 2017.

[26] Z. F. Ren, Z. P. Huang, D. Z. Wang, J. G. Wen, J. W. Xu, J. H. Wang, L. E. Calvet, J. Chen, J. F. Klemic and M. A. Reed, "Growth of a single freestanding multiwall carbon nanotube on each nanonickel dot," *Applied Physics Letters*, vol. 75, no. 8, pp. 1086-1088, 1999.

[27] S. S. Nemala, K. Mokurala, P. Bhargava, and S. Mallick, "Cu_2ZnSnS_4/CNT composites as Pt free counter electrodes for dye sensitized solar cells with improved efficiency," *Materials Today: Proceedings*, vol. 3, no. 6, pp. 1808-1814, 2016.

[28] P. Dai, G. Zhang, Y. Chen, H. Jiang, Z. Feng, Z. Lin and J. Zhan, "Porous copper zinc tin sulfide thin film as photocathode for double junction photoelectrochemical solar cells," *Chemical Communications*, vol. 48, no. 24, pp. 3006-3008, 2012.

[29] L. Bai, J. N. Ding, N. Y. Yuan, H. W. Hu, Y. Li, and X. Fang, "Cu_2ZnSnS_4/graphene composites as low-cost counter electrode materials for dye-sensitized solar cells," *Materials Letters*, vol. 112, pp. 219-222, 2013.

Chapter 2 : Literature review

2.1 Dye-sensitized solar cells

2.1.1 Architecture

The DSSC set-up has three major components; an anode material of a dye anchored on a wide band gap semiconductor, an electrolyte and a cathode, otherwise known as counter electrode (CE) as depicted in **Figure 2.1** [1], [2]. The dye facilitates photon absorption and electron injection into the semiconductor, which then transports the electron to the external circuit and ultimately, the electron is collected by the CE [3]. Since the discovery of the DSSC by O`Regan and Gräzel in 1991, TiO_2, Ru (II) polypyridyl dyes [4] and Pt [5] were found as suitable and promising oxide semiconductor, sensitizer and CE materials, respectively, resulting in a PCE of 7.9% [6]. The question that remains therefore is why these devices have not been commercialized yet. Several factors have contributed to this setback and include the low power to electricity conversion, long term instability and expensive materials used in their construction [7]–[9].

Each component of the DSSC contributes to this limitation in one way or another. For instance, Ru (II) polypyridyl based dyes are commonly used as sensitizers because they can absorb a wider range of the solar spectrum and their energy levels are compatible with those of TiO_2 while the common electrolyte redox couple is I^-/I_3^- [4], [10]. However, precursors of these dyes are expensive, scarce and toxic [11]. Platinum, on the other hand, is a noble metal and degrades after extended exposure to the I^-/I_3^- electrolyte [12]. The high cost, limited availability of Pt and Ru dye precursors and corresponding low efficiency have rendered DSSCs commercially unviable. Extensive studies on maximizing the conversion efficiency of DSSCs by studying and trying to optimize the individual components are currently underway, globally. Such attempts include trying to increase the photon extraction by increasing the number of layers of dye which was proven worthless in this regard. Recently, researchers have shown that alternatively, quantum dots can be exploited for increased solar absorption thereby giving them the name quantum dot sensitized solar cells (QDSSCs) [13].

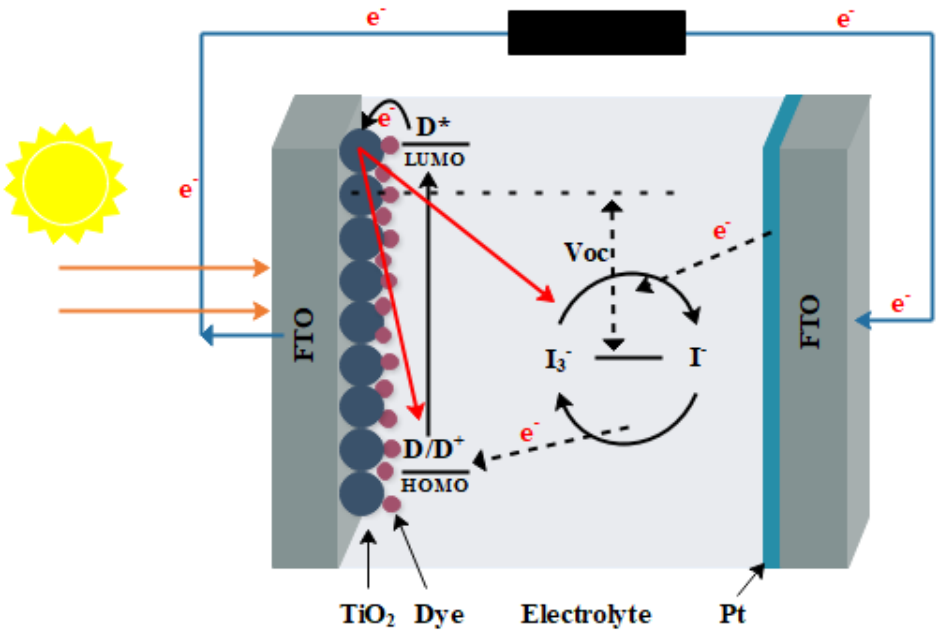


Figure 2.1: Schematic diagram showing components of the dye-sensitized solar cell [10].

2.1.1.1 Photoanode

Photoanode is one of the major components of a DSSC. It is made up of a dye spread on an oxide semiconductor deposited on conductive glass substrate of fluorine doped tin oxide (FTO) or indium doped tin oxide (ITO). The dye, semiconductor and substrate are responsible for photon harvesting, electron injection and electron extraction, respectively [14]. High surface area, good electron transport mobility, a conduction band that has energy lower than the lowest unoccupied molecular orbital (LUMO) of the dye to allow good dye loading and good electron collection are some of the crucial properties the oxide should possess [11]. ZnO and TiO_2 are some of the suitable oxide materials employed in DSSCs to accelerate electron transfer to the external circuit because they are abundant, biocompatible and have low toxicities [15]. Additionally, these semiconductors have conduction bands that are lower in energy than the LUMO of the dye, a factor that promotes electron extraction from the photo-excited dye. Several factors should be considered when selecting the dye and the oxide material. Firstly, the dye should have a strong interaction with the oxide material, a high absorption efficiency in the visible region and its oxidized from should be easily reduced by the electrolyte [16]. Several studies have shown that multilayer dye does not increase the photon absorption of the dye [17]. Alternatively, high surface area oxide can be employed to unsure a better coverage by the mono layer dye. Various morphologies of these oxides including nanorods, nanowires, nano-rings and nanobelts have thus been studied [18].

2.1.1.2 Electrolyte

An electrolyte constitutes of a redox couple dispersed in an organic solvent and conveys electrons from the CE to the anode to facilitate dye-regeneration. Dye recombination occurs if electron transfer from the electrolyte to the oxidized dye is not fast enough while electrolyte recombination occurs if electron extraction from the anode and electrolyte regeneration are not fast enough [14]. Therefore, the choice of electrolyte plays a key role in the overall efficiency of the DSSC. Some of the vital properties that the redox duo should possess include high ionic mobility and good solubility in the solvent of interest, slow recombination rate with the ejected electron as well as accelerated electron handover at the electrolyte-CE interface [19]. There are three electrolyte systems that can be employed in DSSCs, namely; liquid [20], quasi-solid [21] and solid-state hole conducting [22], [23] electrolytes. Iodide/triiodide (I^-/I_3^-) liquid based electrolytes are the most popular in DSSCs because the rate at which I_3^- reduces the oxidized dye is faster than the rate at which I_3^- can be reduced by the semiconductor anode material thus limiting the chance of recombination [5]. Redox compounds that have a more positive potential that the I^-/I_3^- are sort after to increase the open circuit voltage of the DSSC. Recently, cobalt complexes were studied as alternative electrolytes and demonstrated easily adjustable redox potentials although their ionic diffusion is limited because of their large size [5], [24].

2.1.1.3 Counter electrode

The DSSC CE plays a major role in the device set-up. The CE collects and transfers the external circuit electron to the oxidation half of the electrolyte [11]. For the electron transport to occur and be used to reduce the electrolyte, the CE material must have a few ideal characteristics. These characteristics include, high electron conductivity, high porosity to allow maximum electrolyte-CE material interaction for efficient catalysis, stability during extended exposure to the electrolyte as well as reducing ability to the electrolyte [25], [26]. Since the development of DSSCs, Pt has been found to be an ideal CE material because of its high catalytic activity towards the common DSSC electrolyte of I^-/I_3^- as well as high surface area of its nanoparticles [10], [27], [28]. Nonetheless, Pt is a rare earth metal, therefore expensive and it dissolves in the I^-/I_3^- electrolyte to form PtI_4 [29]. These shortcomings of Pt have prompted research studies towards alternative CE materials that have high surface area, good electron conductivity and comparable, if not better, catalytic activities than Pt. Such CE materials include carbon nanomaterials [30], [31] and chalcogenides [32].

Carbon materials such as carbon black, carbon nanotubes and graphite offer interesting properties like high conductivity and surface area, chemical stability and low-cost [33]. Chalcogenides, on the other hand, offer good catalytic properties towards the electrolyte, low-cost as well as ample constituent elements in the earth crust [34]. This study will be focused on combining the electron transport and surface area of the carbon nanotubes and the promising catalytic ability of quaternary Cu_2ZnSnS_4 chalcogenide in a hybrid system with the aim of achieving comparable DSSC power conversion efficiency (PCE) using cheap and easily synthesized materials.

2.1.1.3.1 Transition metal chalcogenides

Solar cells based on thin films of organic, inorganic and hybrid semiconductors have shown potential as alternatives to high cost, high efficiency silicon solar cells because they possess high absorption coefficients [35], [36]. Chalcogenides are inorganic compounds that are made up of sulfides, selenides or tellurides (chalcogens) and at least one electropositive transition metal element [13]. Binary, ternary and quaternary chalcogenide are composed of one chalcogen and one, two and three positively charged atoms, respectively. Binary and ternary nanoparticles such as CdSe/Te, PbS(Se), $CuInS_2$, Cu(In,Ga)(Se,S), and $CuInSe_2$ have been employed as absorber layers in photovoltaic devices to replace conventional silicon in conventional photovoltaic devices, and yielded promising power conversion efficiencies because of their high absorption coefficients and ideal band gap [35], [37]. Mass production of devices based on these compounds is hindered by the inadequate supply and elevated cost of indium, gallium and tellurium and cadmium toxicity. Quaternary nanoparticles such as Cu_2ZnSnS_4 (CZTS) are reported to exhibit better corrosion resistance, higher absorption coefficients and tunable band gap over their counter-parts due to optical bowing effect [38].

2.1.1.3.2 Copper zinc tin sulfide

Cu_2ZnSnS_4 (CZTS) is a quaternary p-type chalcogenide semiconductor with a tunable band gap and a high absorption coefficient of about 10^{-4} cm^{-1} [39]. Its constituent elements are abundant and have relatively low toxicity. These properties have rendered vast studies on CZTS as a light harvesting layer in p-n junction solar cells. Additionally, CZTS has been reported by Dai and coworkers as a catalytic material, thereby diversifying its development from an absorber layer to a reducing material in DSSC CE [32]. This compound is derived from $CuInS_2$ upon replacing In with Zn and Sn atoms as shown in **Figure 2.2 (a)**. Cu_2ZnSnS_4 exhibits three major crystal structures, cubic, tetragonal (kesterite and stannite)

and hexagonal form [40]–[43]. In the cubic crystal unit cell, metal atoms are positioned randomly while Cu and Zn atoms either conform to their positions in an ordered or disordered manner whereas the Sn atoms take fixed position in hexagonal crystal structure. For kesterite tetragonal crystal structure, in particular, CuSn, CuZn cation-ionic layers alternate positions while the ZnSn and CuCu layers [44] alternate positions in the stannite crystal structure as seen from **Figure 2.2 (b) & (c)** below. Kesterite CZTS is thermodynamically more stable than the stannite form. Thin film technology through ink fabrication on various substrates is a major part of solar cell development aimed at reducing the cost of production and increasing the sustainability solar technology.

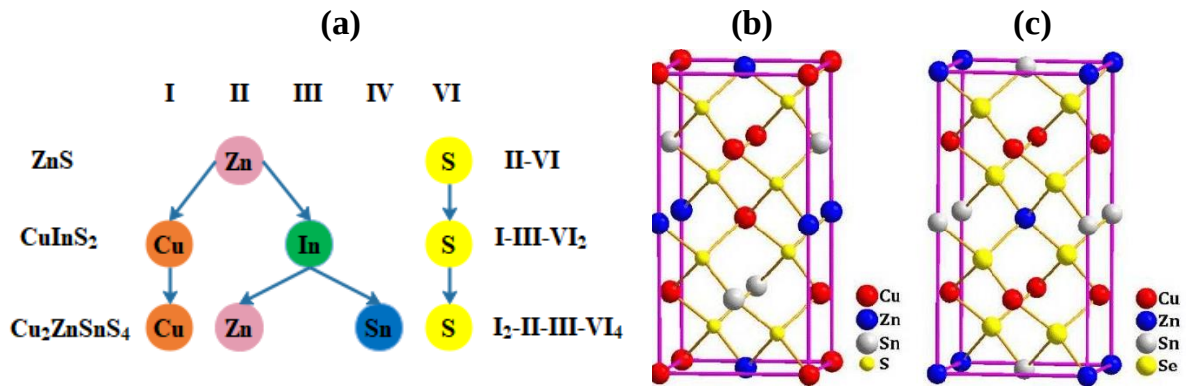


Figure 2.2: (a) Schematic diagram illustrating basis of CZTS development and (b) kesterite and (c) stannite tetragonal crystal structures of $Cu_2ZnSn(S/Se)_4$ [45].

2.1.1.3.3 CZTS ink fabrication

Fabrication of PV devices can be achieved by either depositing an ink of the compound of interest or electrodeposition of the precursor metallic ions on a conductive substrate by employing either vacuum or non-vacuum based methods. Vacuum processing techniques include sputtering (argon beam, ion beam and magnetron), evaporation (co-evaporation, electron beam and thermal evaporation) and pulsed laser deposition of the target compound atoms under controlled temperature and pressure [39], [46]–[48]. The two former procedures follow the same approaches of either simultaneously depositing the metal sources followed by sulfurization of the films or, sequential deposition of the metal precursors. The procedures offer advantages of high film reproducibility as well as optimal element composition of the film [49]. The urge to reduce the cost of PV devices under all aspects has rendered a shift to less costly non-vacuum deposition procedures such as spray pyrolysis, electrodeposition, sol-gel and doctor blading [50]. Alternatively, the inorganic nanomaterials can be prepared by solvothermal, hydrothermal, sol-gel and colloidal synthesis and an ink solution prepared and

then deposited on substrates by spin coating, drop casting and doctor blade technology [51]–[55]. In hydrothermal and solvothermal methods, the metal and chalcogenide sources are dissolved in water and organic solvent, respectively and exposed to high temperature and pressure usually by an autoclave or microwave. Colloidal synthesis is a solution-based approach that offers the advantage of morphology, shape and size control [53]. Due to the ease and low temperature requirements for the preparation of inorganic materials, colloidal synthesis of CZTS will be employed in this research. These colloids can be coalesced with carbon materials for application as CEs in DSSCs.

2.1.1.3.4 Carbon nanomaterials

Carbon is a group 14 element with electronic configuration of $1s^2$, $2s^2$, and $2p^2$ [56]. Carbon can bond with another carbon to form sp, sp^2 and sp^3 hybridizations, resulting in carbon having up to eight allotropic forms. These include diamond which is made up of a three-dimensional network of sp^3 hybridized carbon, graphite, a two-dimensional network of sp^2 hybridized carbons and fullerenes which are composed of sp^2 carbon units forming hollow spheres, ellipsoid and tubular structures [57], [58]. The chemical and physical properties of the different forms of carbon are extremely diverse and have thus prompted vast amount of research rendering carbon as one of the most studied elements. Some of these carbon forms are shown in **Figure 2.3** below. Of these, carbon nanotubes are vastly researched because of their diverse properties.

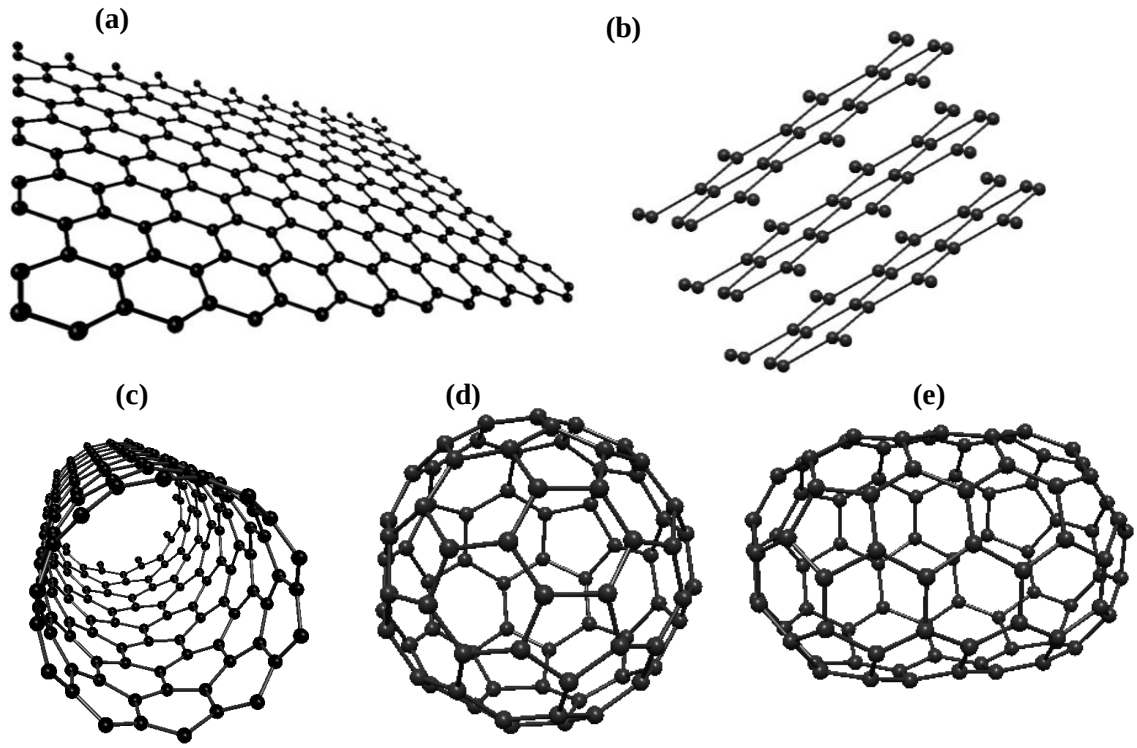


Figure 2.3: Some of the carbon allotropes: (a) graphene, (b) graphite (c) carbon nanotube, (d) fullerene (C_{60}) and (e) fullerene (C_{90}) (Structures generated by Nanotube Modeler).

2.1.1.3.5 Carbon nanotubes

Carbon nanotubes (CNTs) are rolled up graphene sheets and fall under the fullerene clan. They exist in two main classes: single-walled carbon nanotubes (SWCNTs) (**Figure 2.4 (a)**) and multi-walled carbon nanotubes (MWCNTs) (**Figure 2.4 (b)**). SWCNTs are single layered, rolled up graphene sheets and have diameters ranging from 0.4 to 3 nm, while MWCNTs have several layers of these cylinders with outer diameter varying from 2 to 30 nm [56]. CNTs hold remarkable properties and have thus found applicability in catalysis [59], sensors, photovoltaics [60], and energy storage [61]. These characteristics include but are not limited to high thermal stability in vacuum at temperatures up to 2800 °C, high electrical and thermal conductivities and excellent mechanical properties. These properties however, depend on the detailed structure of the nanotube, such as the diameter, the length, twisting ability of the tube and the type of the nanotube [62]. In SWCNTs, for example, the chiral vector, an integer that determines the direction of rolling a graphene sheet, expressed by **Equation 2.1** below, predicts the electrical conductivity nature of the nanotubes. When n-m is a multiple of three, the SWCNT is metallic in nature, otherwise it is semi-conducting [56].

$$\mathbf{C = na_1 + ma_2}$$ ----------**Equation 2. 1**

Where C is chiral vector, n & m are indices that describe chiral vector and a_1& a_2 are base cell vectors of graphite.

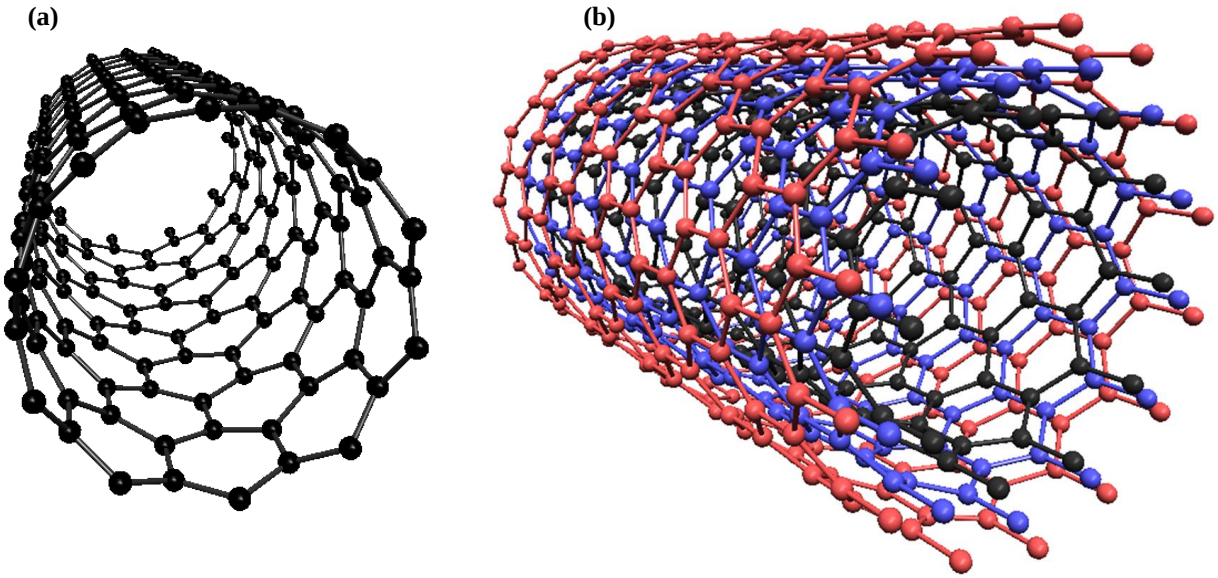


Figure 2.4: Common carbon nanotubes (a) single-walled carbon nanotube (b) multi-walled carbon nanotubes (generated by Nanotube Modulator).

2.1.2 Working principle of dye-sensitized solar cells

The dye molecule can exist in either the ground state or the excited state with an energy gap between the states. The highest energy state in the ground state is referred to as the highest occupied molecular orbital (HOMO) while the lowest energy state in the excited state is known as the lowest unoccupied molecular orbital (LUMO). Upon exposure of the cell to radiation, photons penetrate the conductive glass and are absorbed by the dye molecules. Absorbed photons that have the same or higher energy than the energy gap between the HOMO and the LUMO, result in electrons being injected into the LUMO of the dye (**Equation 2.2**) [29]. Thereafter, the excited electron can be transferred into the conduction band of the TiO_2 semiconductor (**Equation 2.3**). This process results in a positively charged dye molecule and to avoid electron recombination with the dye, and facilitate dye regeneration, three iodide ions diffuse to the dye-electrolyte interface and reduce two previously oxidized dye molecules, generating two neutral dye molecules and a triiodide ion [63]. The triiodide then diffuses to the electrolyte-CE interface, where it gets reduced by electrons from the external circuit that were collected by the CE material [64], [65]. Chemical reactions within DSSC following photo-absorption:

$$D \xrightarrow[\text{photo-excitation}]{} D^* \text{----------Equation 2.2}$$

$$D^* \xrightarrow[\text{electron injection}]{} D^+ + e^- \text{---------- Equation 2.3}$$

$$2D^+ + 3I^- \xrightarrow[\text{dye regeneration}]{} 2D + I_3^- \text{----------Equation 2.4}$$

$$I_3^- + 2e^- \xrightarrow[\text{electrolyte regeneration}]{} 3I^- \text{----------Equation 2.5}$$

Recombination mechanism:

$$e^- + D^+ \xrightarrow[\text{dye recombination}]{} D \text{----------Equation 2.6}$$

$$e^- + I_3^- \xrightarrow[\text{electrolyte recombination}]{} 3I^- \text{----------Equation 2.7}$$

2.1.3 Characterization of dye-sensitized solar cells

Generally, the photon to electricity conversion transformation of the DSSC relies on the open circuit voltage (V_{oc}) which is the distance between the energy of the redox pair in the electrolyte and the Fermi-level of the anode semiconductor and cell current density. V_{oc} is the maximum voltage that a cell can produce [66]. Cell current density depends on the diffusion rate of the electron through the anode material and is shown to improve if the anode material is highly crystalline and the inter-particle distance is minimal, thus allowing a smoother electron movement [67], [68]. Photocurrent-voltage (*J-V*) (**Figure 2.5**) and electrochemical measurements of the cell or anode, cathode and electrolyte are carried out to evaluate the stability level or cell component optimization [2]. The *J-V* curve gives the short circuit current density (J_{sc}), open circuit voltage whose product magnitude is used to calculate the power conversion efficiency (η) of the cell as shown in **Equation 2.8**. The fill factor (FF) (**Equation 2.8)**, ratio of the maximum device power to theoretical maximum power demonstrates how close to a rectangular shape the *J-V* curve is. Reducibility of the electrolyte and reducing ability of the counter electrode towards the electrolyte redox pair can be determined by cyclic voltammetry (CV), while the electrochemical impedance spectroscopy (EIS) assesses electronic and ionic resistance of the electrolyte, electronic mobility resistance and recombination in the anode semiconductor, and resistance to electron movement in the CE [2].

$$\eta\,(\mathbf{PCE}) = \frac{\text{Device } P_{max}}{\text{light power}} = \frac{V_{oc} \times J_{sc} \times FF}{P_{in}} \times 100\,\% \text{----------Equation 2.8}$$

$$FF = \frac{\text{Device } P_{max}}{\text{Theoretical } P_{max}} = \frac{V_{max} \times J_{max}}{V_{oc} \times J_{sc}}$$ ----------Equation 2.9

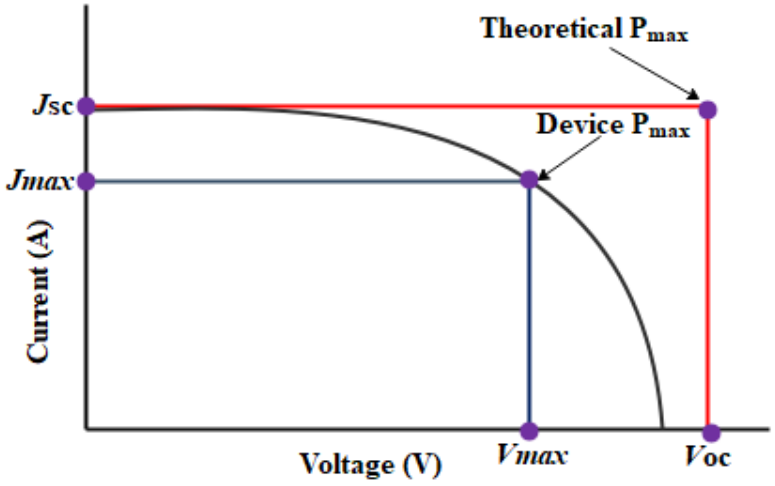


Figure 2.5 : Typical photocurrent-voltage (*J-V*) curve of a dye-sensitized solar cell.

2.1.4 CZTS/MWCNTs nanocomposites in DSSCs

A few articles report on the use of CZTS nanoparticles/carbon nanotube composites counter electrode based DSSCs. Nemala and co-workers studied the effect of adding 1 weight % of CNTs to CZTS on the short circuit current density of DSSC. Jsc of DSSC increased from 10.6 $mAcm^{-2}$ when using CZTS CE to 14.2 $mAcm^{-2}$ for DSSC based on CZTS/CNT nanocomposite resulting in 6.3 % PCE. The improved surface area and porosity due induced by carbon nanotubes which improves accessibility of active sites to the electrolyte solution was reported as one of the factors that resulted in this increase in current density [34]. The same trend was observed on CZTS/MWCNTs nanocomposites CE based DSSCs developed by Chen et al [69]. J_{sc} of the DSSC increased from 14.33 $mAcm^{-2}$ when CZTS was employed as a CE DSSC to 16.62 $mAcm^{-2}$ for CZTS/MWCNT CE.

2.2 References

[1] J. Gong, J. Liang, and K. Sumathy, "Review on dye-sensitized solar cells (DSSCs): Fundamental concepts and novel materials," *Renewable and Sustainable Energy Reviews*, vol. 16, no. 8, pp. 5848-5860, 2012.

[2] S. J. Fonash, "Dye-sensitized solar cells," *Chemical Reviews*, vol. 110, pp. 295-309, 2010.

[3] S. Sharma, Bulkesh Siwach, S. K. Ghoshal, and D. Mohan, "Dye sensitized solar cells: From genesis to recent drifts," *Renewable and Sustainable Energy Reviews*, vol. 70,

pp. 529-537, 2017.

[4] B. E. Hardin, H. J. Snaith, and M. D. McGehee, "The renaissance of dye-sensitized solar cells," *Nature Photonics*, vol. 6, no. 3, pp. 162-169, 2012.

[5] M. Wang, C. Grätzel, S. M. Zakeeruddin, and M. Grätzel, "Recent developments in redox electrolytes for dye-sensitized solar cells," *Energy & Environmental Science*, vol. 5, no. 11, pp. 9394-9405, 2012.

[6] B. O. Regan and M. Grätzel, "A low-cost, high-efficiency solar cell based on dye-sensitized colloidal TiO_2 films," *Nature*, vol. 353, pp. 737-740, 1991.

[7] A. Fakharuddin, R. Jose, T. M. Brown, F. Fabregat-Santiago, and J. Bisquert, "A perspective on the production of dye-sensitized solar modules," *Energy Environmental Science*, vol. 7, no. 12, pp. 3952-3981, 2014.

[8] H. Matsui, K. Okada, T. Kitamura, and N. Tanabe, "Thermal stability of dye-sensitized solar cells with current collecting grid," *Solar Energy Materials and Solar Cells*, vol. 93, no. 6-7, pp. 1110-1115, 2009.

[9] J. M. Kroon, N. J. Bakker, H. J. P. Smit, P. Liska, K. R. Thampi, P. Wang, S. M. Zakeeruddin, M. Grätzel, A. Hinsch, S. Hore, U. Würfel, R. Sastrawan, J. R. Durrant , E. Palomares, H. Pettersson , T. Gruszecki , J. Walter , K. Skupien and G. E. Tulloch "Nanocrystalline dye-sensitized solar cells having having maximum performance," *Progress in Photovoltaics: Research and Applications*, vol. 15, pp. 1-18, 2013.

[10] A. Jena, S. P. Mohanty, P. Kumar, J. Naduvath, V. Gondane, P. Lekha, J. Das, H. K. Narula, S. Mallick and P. Bhargava, "Dye sensitized solar cells: A review," *Transactions of the Indian Ceramic Society*, vol. 71, no. 1, pp. 1-16, 2012.

[11] M. Ye, X. Wen, M. Wang, J. Iocozzia, N. Zhang, C. Lin and Z. Lin, "Recent advances in dye-sensitized solar cells: From photoanodes, sensitizers and electrolytes to counter electrodes," *Materials Today*, vol. 18, no. 3, pp. 155-162, 2015.

[12] E. Olsen, G. Hagen, and S. Eric Lindquist, "Dissolution of platinum in methoxy propionitrile containing LiI/I_2," *Solar Energy Materials and Solar Cells*, vol. 63, no. 3, pp. 267-273, 2000.

[13] H. Zhang, K. Cheng, Y. M. Hou, Z. Fang, Z. X. Pan, W. J. Wu, J. L. Hua and X. H. Zhong "Efficient CdSe quantum dot-sensitized solar cells prepared by a postsynthesis assembly approach," *Chemical Communications*, vol. 48, no. 91, pp. 11235-11237, 2012.

[14] E. Palomares, J. N. Clifford, S. A. Haque, T. Lutz, and J. R. Durrant, "Control of charge recombination dynamics in dye sensitized solar cells by the use of conformally

deposited metal oxide blocking layers," *Journal of the American Chemical Society*, vol. 125, no. 2, pp. 475-482, 2003.

[15] J. Guan, J. Zhang, T. Yu, G. Xue, X. Yu, Z. Tang, Y. Wei, J. Yang, Z. Li and Z. Zou, "Interfacial modification of photoelectrode in ZnO-based dye-sensitized solar cells and its efficiency improvement mechanism," *RSC Advances*, vol. 2, no. 20, pp. 7708-7713, 2012.

[16] M. Grätzel, "Dye-sensitized solar cells," *Journal of Photochemistry and Photobiology C: Photochemistry Reviews*, vol. 4, pp. 145-153, 2015.

[17] R. C. Nelson, "Minority carrier trapping and dye sensitization," *The Journal of Physical Chemistry*, vol. 69, no. 3, pp. 714-718, 1965.

[18] C. Bhakat and P. P. Singh, "Zinc oxide nanorods: Synthesis and its applications in solar cell," *International Journal of Modern Engineering Research*, vol. 2, no. 4, pp. 2452-2454, 2012.

[19] T. W. Hamann and J. W. Ondersma, "Dye-sensitized solar cell redox shuttles," *Energy and Environmental Science*, vol. 4, no. 2, pp. 370-381, 2011.

[20] N. Yamanaka, R. Kawano, W. Kubo, T. Kitamura, and Y. Wada, "Ionic liquid crystal as a hole transport layer of dye-sensitized solar cells," *Chemical Communications*, vol. 6, pp. 740-742, 2005.

[21] A. F. Nogueira, J. R. Durrant, and M. A. De Paoli, "Dye-sensitized nanocrystalline solar cells employing a polymer electrolyte," *Advanced Materials*, vol. 13, no. 11, pp. 826-830, 2001.

[22] T. Stergiopoulos, I. M. Arabatzis, G. Katsaros, and P. Falaras, "Binary polyethylene oxide/titania solid-state redox electrolyte for highly efficient nanocrystalline TiO_2 photoelectrochemical cells," *Nano Letters*, vol. 2, no. 11, pp. 1259-1261, 2002.

[23] D. Li, D. Qin, M. Deng, Y. Luo, and Q. Meng, "Optimization the solid-state electrolytes for dye-sensitized solar cells," *Energy and Environmental Science*, vol. 2, no. 3, pp. 283-291, 2009.

[24] M. Wang, N. Chamberland, L. Breau, J. Moser, R. Humphry-Baker, B.Marsan, S. M. Zakeeruddin and M. Grätzel, "An organic redox electrolyte to rival triiodide/iodide in dye-sensitized solar cells," *Nature Chemistry*, vol. 2, no. 5, pp. 385-389, 2010.

[25] X. Sun, J. Dou, F. Xie, Y. Li, and M. Wei, "One-step preparation of mirror-like NiS nanosheets on ITO for the efficient counter electrode of dye-sensitized solar cells," *Chemical Communications*, vol. 50, no. 69, pp. 9869-9871, 2014.

[26] Y. S. Yen, H. H. Chou, Y. C. Chen, C. Y. Hsu, and J. T. Lin, "Recent developments in

molecule-based organic materials for dye-sensitized solar cells," *Journal of Materials Chemistry*, vol. 22, no. 18, pp. 8734-8747, 2012.

[27] G. Calogero, P. Calandra, A. Irrera, A. Sinopoli, I. Citro, and G. Di Marco., "A new type of transparent and low cost counter-electrode based on platinum nanoparticles for dye-sensitized solar cells," *Energy & Environmental Science*, vol. 4, no. 5, pp. 1838-1844, 2011.

[28] K. L. Chopra, P. D. Paulson, and V. Dutta, "Thin-film solar cells: An overview," *Progress in Photovoltaics: Research and Applications*, vol. 8, no. 12, pp. 69-92, 2004.

[29] M. Z. H. Khan, M. R. Al-Mamun, P. K. Halder, and M. A. Aziz, "Performance improvement of modified dye-sensitized solar cells," *Renewable and Sustainable Energy Reviews*, vol. 71, pp. 602-617, 2017.

[30] J.-Z. Chen, Y.-C. Yan, and K.-J. Lin, "Effects of carbon nanotubes on dye-sensitized solar cells," *Journal of the Chinese Chemical Society*, vol. 57, pp. 1180-1184, 2010.

[31] O. Topon, D. Matsumoto, and M. Inaguma, "Carbon nanotubes counter electrode for dye-sensitized solar cell," *Fujikura Technical Review*, pp. 47-50, 2011.

[32] P. Dai, G. Zhang, Y. Chen, H. Jiang, Z. Feng, Z. Lin and J. Zhan, "Porous copper zinc tin sulfide thin film as photocathode for double junction photoelectrochemical solar cells," *Chemical Communications*, vol. 48, no. 24, pp. 3006-3008, 2012.

[33] S. Huang, H. Sun, X. Huang, Q. Zhang, D. Li, Y. Luo and Q. Meng, "Carbon nanotube counter electrode for high-efficient fibrous dye-sensitized solar cells," *Nanoscale Research Letters*, vol. 7, no. 1, pp. 1-7, 2012.

[34] S. S. Nemala, K. Mokurala, P. Bhargava, and S. Mallick, "Cu_2ZnSnS_4/CNT composites as Pt free counter electrodes for dye sensitized solar cells with improved efficiency," *Materials Today: Proceedings*, vol. 3, no. 6, pp. 1808-1814, 2016.

[35] H. Azimi, Y. Hou, and C. J. Brabec, "Towards low-cost, environmentally friendly printed chalcopyrite and kesterite solar cells," *Energy and Environmental Science*, vol. 7, no. 6, pp. 1829-1849, 2014.

[36] V. V Tyagi, N. A. A. Rahim, N. A. Rahim, and J. A. L. Selvaraj, "Progress in solar PV technology: Research and achievement," *Renewable and Sustainable Energy Reviews*, vol. 20, pp. 443-461, 2013.

[37] M. K. S. Karuppusamy and R. S. R. Gopalakrishnan, "Synthesis of reduced graphene oxide-copper tin sulphide composites and their photoconductivity enhancement for photovoltaic applications," *Journal of Materials Science*, vol. 50, no. 24, pp. 8029-8037, 2015.

[38] Z. Pan, K. Zhao, X. Zhong, Y. Feng, J. Wang and H. Zhang, "Near infrared absorption of $CdSe_xTe_{1-x}$ alloyed quantum dot sensitized solar cells with more than 6 % efficiency and high stability," *ACS Nano*, vol. 7, no. 6, pp. 5215-5222, 2013.

[39] H. Katagiri, K. Jimbo, S. Yamada, T. Kamimura, W. S. Maw, T. Fukano, T. Ito and T. Motohiro, "Enhanced conversion efficiencies of Cu_2ZnSnS_4-based thin film solar cells by using preferential etching technique," *Applied Physics Express*, vol. 1, no. 4, pp. 0412011-0412012, 2008.

[40] S. Schorr and G. Gonzalez-Aviles, "In-situ investigation of the structural phase transition in kesterite," *Physica Status Solidi (A)*, vol. 206, no. 5, pp. 1054-1058, 2009.

[41] S. Siebentritt and S. Schorr, "Kesterites-a challenging material for solar cells," *Progress in Photovoltaics: Research and Applications*, vol. 20, pp. 512–519, 2012.

[42] S. Chen, A. Walsh, Y. Luo, J. H. Yang, X. G. Gong, and S. H. Wei, "Wurtzite-derived polytypes of kesterite and stannite quaternary chalcogenide semiconductors," *Physical Review B -Condensed Matter and Materials Physics*, vol. 82, no. 19, pp. 1-8, 2010.

[43] A. Singh, S. Singh, S. Levcenko, T. Unold, F. Laffir, and K. M. Ryan, "Compositionally tunable photoluminescence emission in $Cu_2ZnSn(S_{1-x}Se_x)_4$ nanocrystals," *Angewandte Chemie - International Edition*, vol. 52, no. 35, pp. 9121-9124, 2013.

[44] R. Ahmad, M. Brandl, M. Distaso, P. Herre, E. Spiecker, R. Hock and W. Peukert, "A comprehensive study on the mechanism behind formation and depletion of Cu_2ZnSnS_4 (CZTS) phases," *Crystal Engineering Communications*, vol. 17, no. 36, pp. 6972-6984, 2015.

[45] X. Zheng, Y. Liu, Y. Du, Y. Sun, J. Li, and R. Zhang, "P-type quaternary chalcogenides of $Cu_2ZnSn(S,Se)_4$ nanocrystals: Large-scale synthesis, bandgap engineering and their thermoelectric performances," *Journal of Alloys and Compounds*, vol. 738, pp. 484-490, 2018.

[46] H. Wang, "Progress in thin film solar cells based on Cu_2ZnSnS_4," *International Journal of Photoenergy*, vol. 2011, pp. 1-10, 2011.

[47] T. Tanaka, T. Nagatomo, D. Kawasaki, M. Nishio, Q. Guo, A. Wakahara, A. Yoshida and H. Ogawa, "Preparation of Cu_2ZnSnS_4 thin films by hybrid sputtering," *Journal of Physics and Chemistry of Solids*, vol. 66, no. 11, pp. 1978-1981, 2005.

[48] P. A. Fernandes, P. M. P. Salomé, and A. F. Da Cunha, "Precursors' order effect on the properties of sulfurized Cu_2ZnSnS_4 thin films," *Semiconductor Science and Technology*, vol. 24, no. 10, pp. 1-7, 2009.

[49] M. P. Suryawanshi, G. L. Agawane, S. M. Bhosale, S. W. Shin, P. S. Patil, J. H. Kim and A. V. Moholkar, "CZTS based thin film solar cells: A status review," *Materials Technology*, vol. 28, no. 1-2, pp. 98-109, 2012.

[50] R. Yang, E. Mazalan, and K. T. Chaudhary, "Non-vacuum deposition methods for thin film solar cell: Review," *American Institute of Physics*, vol. 030018, pp. 030018-1-030018-6,2017.

[51] J. Li, Q. Wu, and J. Wu. (2015) "Synthesis of nanoparticles via solvothermal and hydrothermal methods," Aliofkhazraei M. (eds) Handbook of nanoparticles. Springer, Chem

[52] P. K. Sarswat and M. L. Free, "Demonstration of a sol-gel synthesized bifacial CZTS photoelectrochemical cell," *Physica Status Solidi A*, vol. 2864, pp. 2861-2864, 2011.

[53] H. Zhou, W. Hsu, H. Duan, B. Bob, and W. Yang, "CZTS nanocrystals: A promising approach for next generation thin film photovoltaics," *Energy & Environmental Science*, vol. 6, pp. 2822-2838, 2013.

[54] K. Mokurala, A. Kamble, P. Bhargava, and S. Mallick, "Fabrication of dye sensitized solar cells with cost-effective quaternary sulfide counter electrode," in *2014 IEEE International Conference on Power Electronics, Drives and Energy Systems (PEDES)*, 2014, pp. 1-4.

[55] K. Ramasamy, M. A. Malik, and P. O. Brien, "Routes to copper zinc tin sulfide Cu_2ZnSnS_4 a potential material for solar cells," *Chemical Communications*, vol. 48, pp. 5703-5714, 2012.

[56] A. Eatemadi, H. Daraee, H. Karimkhanloo, M. Kouhi, and N. Zarghami, "Carbon nanotubes: Properties, synthesis, purification and medical applications," *Nanoscale Research Letters*, vol. 9, pp. 1-13, 2014.

[57] H. W. Kroto, J. R. Heath, S. C. O`Brien, R. F. Curl, and R. E. C. Smalley, "C60-The third man," *Nature*, vol. 318, pp. 162-163, 1985.

[58] A. Aqel, M. M. Kholoud, M. M. El-Nour, R. A. A. Ammar, and A. Al-Warthan, "Carbon nanotubes, science and technology part (I) structure, synthesis and characterisation," *Arabian Journal of Chemistry*, vol. 5, pp. 1-23, 2012.

[59] M. C. Bahome, L. L. Jewell, D. Hildebrandt, D. Glasser, and N. J. Coville, "Fischer-Tropsch synthesis over iron catalysts supported on carbon nanotubes," *Applied Catalysis A: General*, vol. 287, no. 1, pp. 60-67, 2005.

[60] A. Shaikjee and N. J. Coville, "The effect of copper catalyst reducibility on low temperature carbon fiber synthesis," *Materials Chemistry and Physics*, vol. 125, no. 3,

pp. 899-907, 2011.

[61] C. Liu, Y. Y. Fan, M. Liu, H. T. Cong, H. M. Cheng, and M. S. Dresselhaus, "Hydrogen storage in single-walled carbon nanotubes at room temperature.," *Science*, vol. 286, no. 5, pp. 1127-1129, 1999.

[62] V. Stefov, M. Najdoski, G. Bogoeva-Gaceva, and A. Buzarovska, "Properties assessment of multiwalled carbon nanotubes: A comparative study," *Synthetic Metals*, vol. 197, pp. 159-167, 2014.

[63] M. Eisenberg and H. P. Silverman, "Photoelectrochemical cells," *Nature*, vol. 414, pp. 338-344, 1961.

[64] M. K. Nazeeruddin, E. Baranoff, and M. Grätzel, "Dye-sensitized solar cells: A brief overview," *Solar Energy*, vol. 85, no. 6, pp. 1172-1178, 2011.

[65] J. Gong, K. Sumathy, Q. Qiao, and Z. Zhou, "Review on dye-sensitized solar cells (DSSCs): Advanced techniques and research trends," *Renewable and Sustainable Energy Reviews*, vol. 68, pp. 234-246, 2017.

[66] F. O. Otieno, "Enhancement of photo-conversion efficiency of organic solar cells by plasmon resonance effect," Thesis, 2015.

[67] S. Kambe, S. Nakade, Y. Wada, T. Kitamura, and S. Yanagida, "Effects of crystal structure, size, shape and surface structural differences on photo-induced electron transport in TiO_2 mesoporous electrodes," *Journal of Materials Chemistry*, vol. 12, no. 3, pp. 723-728, 2002.

[68] S. Ngamsinlapasathian, T. Sreethawong, Y. Suzuki, and S. Yoshikawa, "Single- and double-layered mesoporous TiO_2/P25 TiO_2 electrode for dye-sensitized solar cell," *Solar Energy Materials and Solar Cells*, vol. 86, no. 2, pp. 269-282, 2005.

[69] H. Chen, J. Wang, C. Jia, J. Mou, and L. Zhu, "Highly efficient dye-sensitized solar cell with a novel nanohybrid film of Cu_2ZnSnS_4-MWCNTs as counter electrode," *Applied Surface Science*, vol. 422, pp. 591-596, 2017.

Chapter 3 : Preparation and acid treatment of N-MWCNTs

3.1 Doped carbon nanotubes

Electronic properties and surface reaction chemistry of carbon nanotubes can be modified by either introducing atoms that have an electron more (nitrogen and sulfur) or less (boron and phosphorus) than carbon within the graphene network or incorporation of carboxylic acid or alcohol functional moieties on the surface of the tubes [1], [2]. The incorporation of heteroatoms can cause rearrangement of the carbon network resulting in a flawed system, improved electronic properties as well as improved surface reactions [3]. These properties have diversified applicability of carbon nanotubes to electro-catalysts [4], photo-catalysts [5], gas sensing materials [6] and metal support structures to improve dispersion in fuel cells [7], [8]. Nitrogen doped carbon nanotubes have particularly attracted many researchers because of nitrogen size similarity to carbon [9], and dependence of its properties on the type of nitrogen environment. Typically, four nitrogen bonding configurations are observed upon nitrogen doping of carbon nanotubes as seen in **Figure 3.1** [10], [11]. Graphitic nitrogen, otherwise referred to as quaternary nitrogen occurs when nitrogen atom replaces the graphitic carbon resulting in formation of an n-type carbon material. Nonetheless, this substitution can also cause reshuffling of neighbouring carbon atoms to form pyridinic or pyridinic oxide nitrogen environments thereby causing defects in the wall configuration [12], [13]. The lone pair in pyridine nitrogen has been shown to take part in basic Knoevenagel condensation reactions and is responsible for the high electron conductivity of the tubes [11], [14], [15].

Several routes can achieve the introduction of foreign atoms in the CNTs network. The first option involves introducing the heteroatom precursor simultaneously with the carbon source in CVD process (in-situ) while the second option entails annealing the pristine carbon nanotubes in the presence of the gaseous heteroatom source and plasma treatment (ex-situ) [16]. The former doping method will be employed in this research. Nitrogen incorporation in carbon nanotubes can be confirmed by bamboo structures in their transmission electron microscopy (TEM) images as opposed to smooth tubes observed in the pristine CNTs [17], [18]. X-ray photoelectron spectroscopy (XPS) in conjunction with elemental analysis are techniques that are employed to further prove the extent and success as well as types of nitrogen environments induced in the carbon nanotubes.

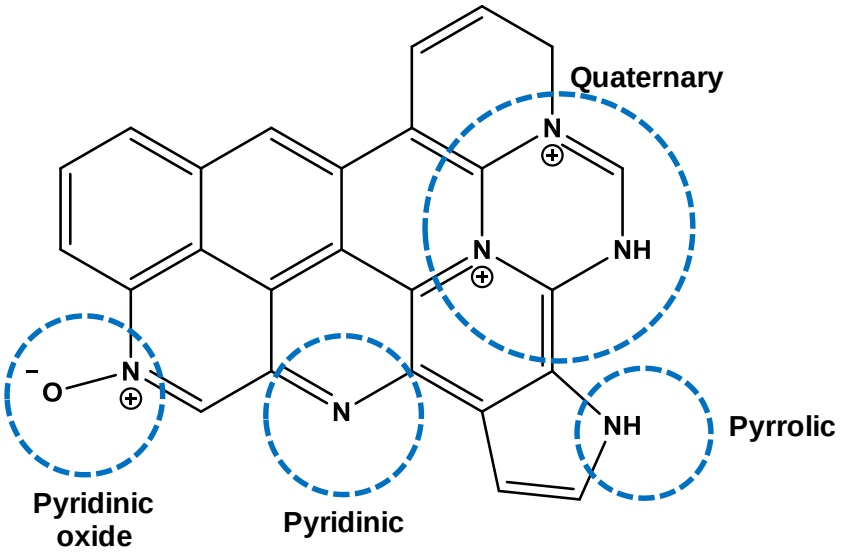


Figure 3.1: Bonding configurations of nitrogen in multi-walled carbon nanotubes post doping [10].

3.2 Synthesis methods of carbon nanotubes

Pristine and doped carbon nanotubes are produced by similar methods which include arc-discharge and laser ablation method, flame pyrolysis and chemical vapor deposition (CVD) method [19]. CVD is the most popular method and involves exposing both the carbon and nitrogen sources to high temperature ranges of 700-1000 °C in the presence of a catalyst. However, at such high temperature, metal catalysts tend to agglomerate and degrade. As such, catalysts are supported on metal oxides or carbonates that possess high surface area, are thermally stable and have electronic interactions with metal particles [12]. Metallic elements of Fe, Co, and Ni and bimetallic Fe-Co have been employed to prepare carbon nanotubes because carbon is soluble and can easily diffuse through them [1], [20], [21]. Fe-Co embedded on $CaCO_3$ has proven to produce the highest yield of MWCNTs attributed to minimal agglomeration, and a stronger metal-support contact [22] and also offers two advantages over other catalysts; high efficiency [23], and easy removal of the residual CaO produced after the reaction with mild acids [24]. Tetana et al., have demonstrated preparation of bamboo N-MWCNTs using Fe-Co/$CaCO_3$ at 800 °C using acetonitrile as carbon and nitrogen sources, and acetylene as carbon source [24].The catalyst particles are first exposed to high temperature for activation, then the hydrocarbon is introduced and decomposed to hydrogen and carbon atoms as it interacts with the catalyst. The carrier gas (N_2) drives off the low-density hydrogen, while carbon is dissolved into the metal until saturation, upon which it precipitates out as a cylindrical network.

3.3 Growth mechanism of carbon nanotubes

The growth mechanism of the nanotubes depends profoundly on the synthesis procedure in question. During the CVD process, a hydrocarbon compound decomposes on the surface of the activated catalyst into carbon and hydrogen. Carbon diffuses through the metal core and precipitates out either at the bottom of the catalyst or grows above the catalyst surface while hydrogen is driven off by the carrier gas. Whether tubes grow below the catalyst surface or above depends on the degree of interaction between the metal catalyst and support used [25], [26]. The hollow nature of the carbon nanotubes is explained by the fact that decomposition and diffusion of carbon occurs from the sides of the hemisphere rather than from the apex. As such, weak forces between the catalyst and support result in a tip growth mechanism while a stronger force of interaction produces a base growth mechanism of the nanotubes.

The tip growth mechanism is a three-step process that involves first the attachment and decomposition of hydrocarbon source on the catalyst particles (**Figure 3.2 (a), (I)**), followed by diffusion and precipitation of carbon through the catalyst particle (**Figure 3.2 (a), (II)**) and ultimately growth (**Figure 3.2 (a), (III)**) of carbon nanotubes [27]. The two latter steps impose diffusion and osmotic pressure, which initiates detachment of the catalyst from the support and causes the catalyst to be elevated off the support. As the carbon diffuses through the catalyst, a solubility saturation point is reached, and diffusion stops and the carbon deposits on the metal block the active site rendering the metal inactive for further attachment and decomposition of the hydrocarbon [19]. The base growth mechanism follows the same rationale and steps as the tip growth although the carbon source attaches on the side of metal particle, however, the strong force of interaction between the particle and support surface, causes the formation of the nanotubes to protrude outwards from the metal particle. The quantity and quality of the produced carbon nanotubes depends on several parameters, which include the size, type and concentration of metal catalyst, temperature and duration of synthesis and flow rate of the gas. In their study, Tetana et al. demonstrated that increasing temperature from 700 °C to 850 °C and 700 to 800 °C resulted in an increase in the yield of N-MWCNTs and thermal stability of the of N-MWCNTs respectively [24].

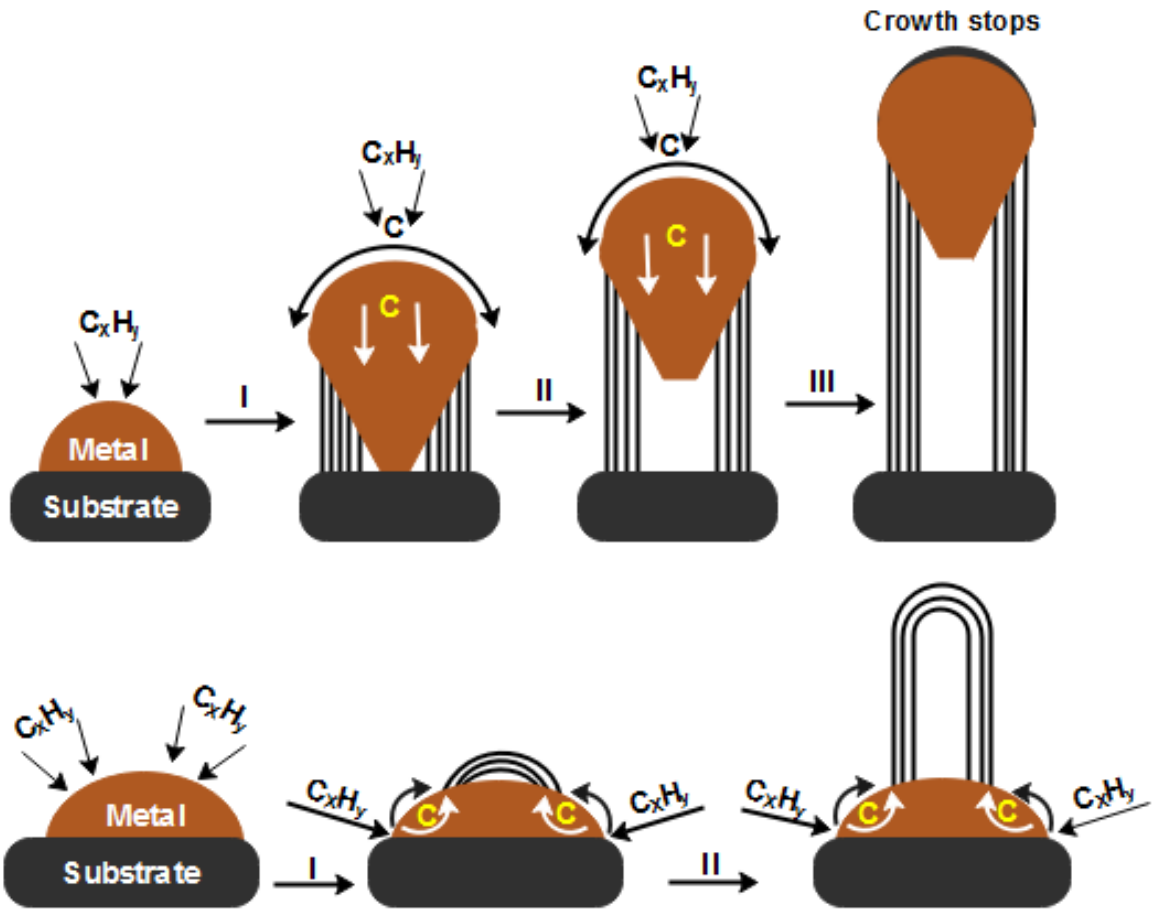


Figure 3.2: Probable growth processes for carbon nanotubes on metal particles; (a) tip and (b) base growth [27].

3.4 Materials and methods

3.4.1 Chemicals

Iron (III) nitrate nonahydrate ($Fe(NO_3)_3.9H_2O$, Sigma-Aldrich), cobalt (II) nitrate hexahydrate ($Co(NO_3)_2.6H_2O$), ethylene glycol ($(CH_2OH)_2$), calcium carbonate ($CaCO_3$, Sigma-Aldrich), acetonitrile (CH_3N, 99.9%, Sigma-Aldrich), sulfuric acid (H_2SO_4, 98%, Sigma-Aldrich), nitric acid (HNO_3, 55%, Sigma-Aldrich) were used as received, without further purification. Acetylene and nitrogen gases used were purchased from African Oxygen (AFROX).

3.4.2 Catalyst synthesis

Wet dispersion method was employed to prepare Fe-Co/$CaCO_3$ catalyst. A 50:50 w/w% of $Fe(NO_3)_3.9H_2O$ and $Co(NO_3)_2.6H_2O$ salts was mixed and ground using a mortar and pestle. The resultant mixture was dissolved in 25 mL of ethylene glycol. In a separate beaker, 9 g

$CaCO_3$ catalyst support was dissolved in 30 mL of ethylene glycol and stirred vigorously for around 30 minutes until the carbonate was well dispersed. The metal precursor mixture was then added to the support mixture dropwise while stirring. The resultant solution was transferred to four microwave tubes, which were then exposed to 500 W for 1 hour in a microwave oven. This procedure is presented in **Figure 3.3** below. Thereafter, the precipitate was filtered to separate the catalyst-support system from ethylene glycol, dried in an oven at 120 °C for 18 hours and then calcined at 400 °C for 16 hours to decompose the nitrates. The supported catalyst was passed through a 150 µm sieve and ultimately used in N-MWCNTs preparation by CVD method.

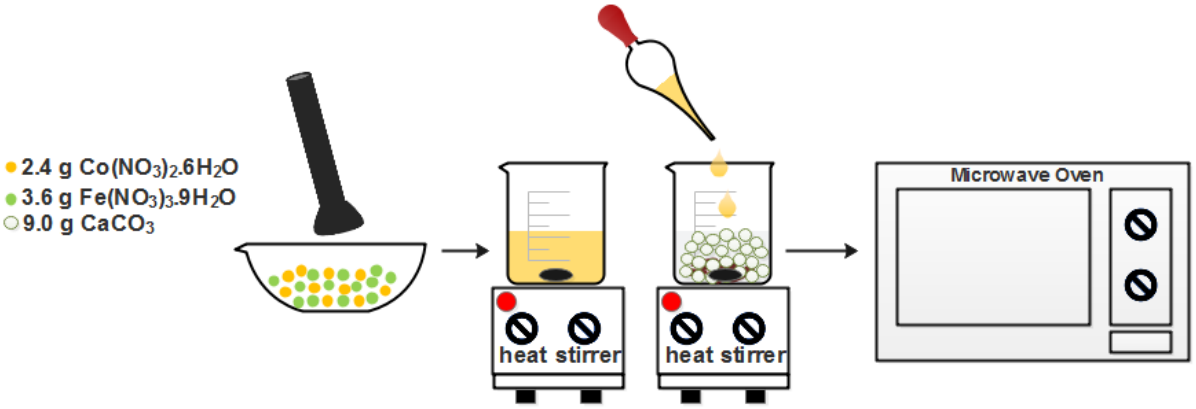


Figure 3.3: Schematic diagram depicting the microwave synthesis procedure for the catalyst.

3.4.3 Preparation and acid functionalization of N-MWCNTs

N-MWCNTs were synthesized by CVD method set-up demonstrated in **Figure 3.4**. In a typical reaction, 0.3 g of the prepared catalyst was spread in a quartz boat, which was then placed in the middle of a tubular quartz reactor in a horizontal furnace. CH_3CN was used as both a carbon and nitrogen sources while C_2H_2 was the carbon source and N_2 transporting medium. Nitrogen (40 mL/min) was initially passed through the reactor for 1 hour to remove any oxygen within the reactor while increasing temperature of the furnace to 800 °C. Then, C_2H_2 and N_2 gases were bubbled through CH_3CN concurrently at 100 mL/min and 240 mL/min respectively for 1 hour. Thereafter, bubbling of the respective gases through CH_3CN was terminated and the reactor cooled under flowing nitrogen at 40 mL/min. This reaction conditions were previously optimized by Tetana and co-workers [24]. The prepared carbon compound was weighted, and then acid treated with 3:1 98% H_2SO_4/55% HNO_3 to remove the catalyst, while oxidizing the terminal carbon atoms, filtered and washed with distilled water. The acid functionalized sample was named fN-MWCNTs. A mixture of sulfuric acid

and nitric acid produces a nitronium cation (NO_2^+) (**Equation 3.1**) which then attacks the benzene ring from the graphitic structure of the nanotubes producing nitrobenzene [28].

$$HNO_{3(aq)} + H_2SO_{4(aq)} \leftrightarrow H_2O_{(aq)} + NO_{2(aq)}^{+} + HSO_{4(aq)}^{-}$$ ----------**Equation 3.1**

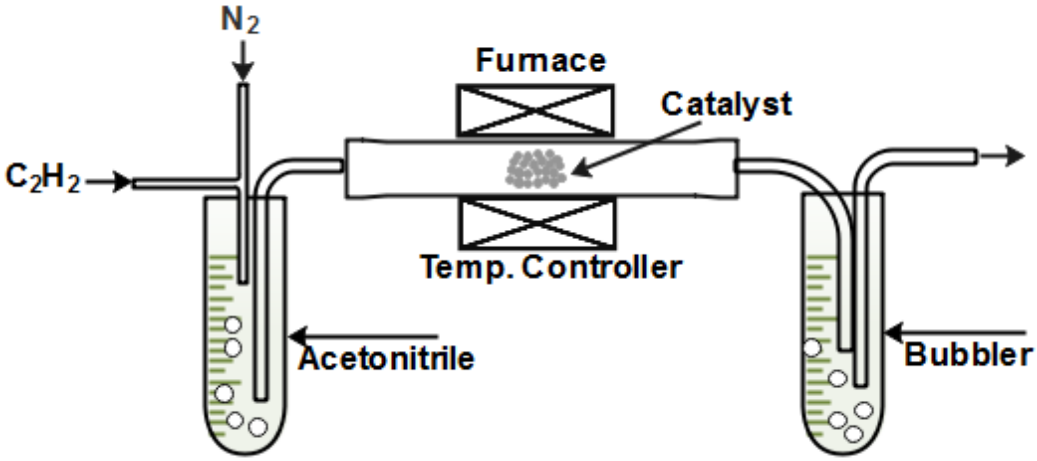


Figure 3.4: CVD method set-up used to prepare N-MWCNTs.

3.4.4 Characterization

Thermal stability and success of residual products removal by acid treatment in the prepared N-MWCNTs was determined by thermogravimetric analysis (TGA) using a Perkin Elmer Pyris 1 TGA and involved heating 10 mg of the CNTs to 900 °C at 10 °C min^{-1} heating rate under air (under nitrogen for Fe-Co/$CaCO_3$). Nitrogen concentration in the nanotubes was determined by C, N elemental analysis using a Carlo Erba NA 1500 Nitrogen Carbon Sulphur Analyzer. The morphology and structural properties of the nanotubes was evaluated by scanning electron microscopy (SEM) using FEI Nova Nanolab 600 SEM, Raman spectroscopy using a John-Yvon T6400 micron Raman spectrophotometer and transmission electron microscopy (TEM) using FEI Technai T12 electron microscope. The amount of nitrogen incorporated within the structure of the nanotubes, as well as the resulting nitrogen bonding configuration was evaluated by XPS (X-ray photoelectron spectroscopy) analysis. XPS analysis of the obtained samples was done on Thermo Scientific ESCAlab 250Xi using a 300 W Monochromatic Al kα (1486.7 eV) X-ray beam with a diameter of 900 µm.

3.5 Results and discussion

3.5.1 Phase composition and thermal stability of Fe-Co/$CaCO_3$

Phase composition of the prepared catalyst was determined by XRD as shown in **Figure 3.5(a)**. Microwave exposure as well as calcination of the Co and Fe nitrate precursors

produces a bi phasic metal oxide of $CoFe_2O_4$ as illustrated in **Equation 3.2**. XRD analysis of the prepared catalyst shows 5 major peaks at around 2θ = 29°, 36°, 44°, 57° and 62° which correspond to [220], [311], [400], [511] and [440] crystallographic planes of cubic $CoFe_2O_4$, respectively (JCPDS no. 79-1744). Presence of $CaCO_3$ support in the catalyst from the XRD analysis can be confirmed by presence of peaks at 2θ = 23°, 29°, 36°, 39°, 44°, 57° and 58° degrees due to [012], [104], [110], [113], [202], [016] and [018] planes of calcite, respectively (JCPDS no. 47-1743). These observations imply that the prepared catalyst contains both the bimetallic catalyst oxide as well as the $CaCO_3$ support. How then do we end up with Fe-Co/$CaCO_3$? During the CVD process, acetylene (carbon source) is adsorbed on $CoFe_2O_4$/$CaCO_3$ and is decomposed to carbon and hydrogen. This hydrogen then activates the catalyst material by reducing $CoFe_2O_4$ to Fe-Co. Bankole et al. demonstrated the presence of 1:1 ratio of Fe and Co metals on EDS after exposing $CoFe_2O_4$/$CaCO_3$ to acetylene, in their study on optimization of Fe-Co/$CaCO_3$ [12].

The N-MWCNTs were prepared by CVD at 800 °C (temperature optimized by Tetana et al. [24]) and to get an insight on the thermal stability of the catalyst when exposed to this temperature, the response of the catalyst as temperature is increased to 900 °C was determined by TGA **(Figure 3.5(b))**. A residual mass after TGA is around 60 % which is due to CaO as well as Co and Fe metals. The weight loss observed around 750 °C can be assigned to CO_2 loss from the thermal decomposition of $CaCO_3$ as illustrated in **Equation 3.3**. This suggests that at the synthesis temperature of N-MWCNTs employed in this study (800 ºC), the CaO. CaO is isolated from the prepared nanotubes acid washing which produces a $CaSO_4$ precipitate (**Equation 3.4**). $CaSO_4$ is partially soluble in water, so upon washing of the acid treated CNTs, the presence of the acid facilitates and improves solubility of the salt and ultimately causes it to be washed off.

$$\mathbf{Co(NO_3)_2.6H_2O_{(s)} + 2Fe(NO_3)_3.9H_2O_{(s)}}$$
$$\mathbf{\rightarrow CoFe_2O_{4(s)} + 8NO_{2(g)} + 2O_{2(g)} + 24H_2O_{(l)}} \text{----------Equation 3.2}$$

$$\mathbf{CaCO_{3(s)} \xrightarrow{\Delta} CaO_{(s)} + CO_{2\,(g)}} \text{----------Equation 3.3}$$

$$\mathbf{H_2SO_{4(aq)} + CaO_{(s)} \rightarrow CaSO_{4\,(s)} + H_2O_{(l)}} \text{----------Equation 3.4}$$

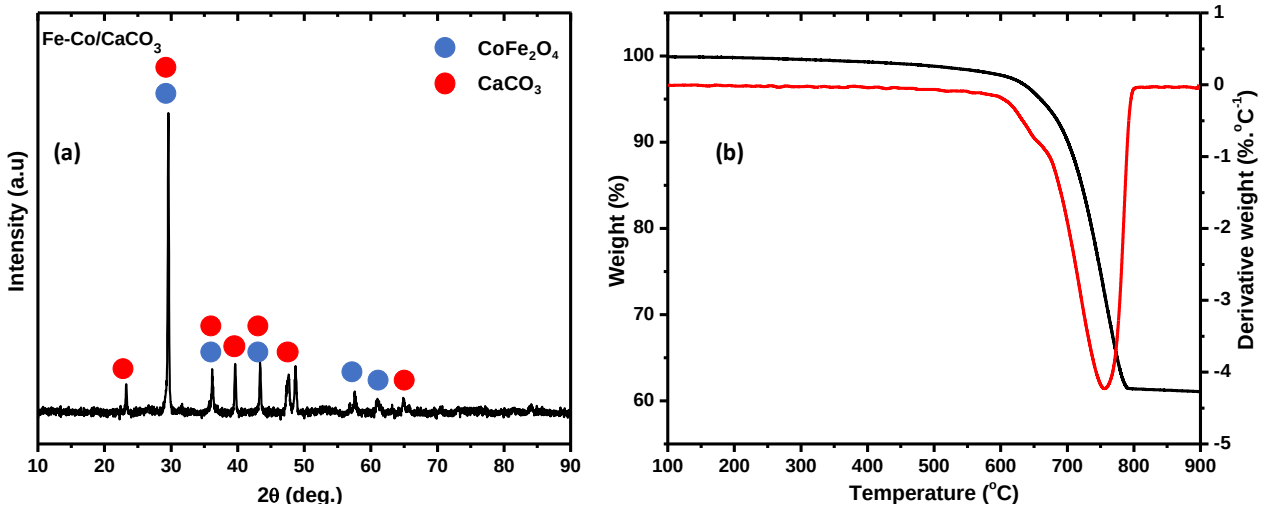


Figure 3.5: (a) X-ray diffraction pattern and (b) Thermogram of Fe-Co catalyst supported on $CaCO_3$.

3.5.2 Structural analysis of as prepared N-MWCNTs and fN-MWCNTs

Figure 3.6 shows the powder XRD patterns of the as prepared and acid treated carbon nanotubes. The most intense peak at 2θ = 28° is due to hexagonal carbon and its intensity increases upon functionalization. This observation implies that the less crystalline carbon materials that were produced alongside N-MWCNTs such as amorphous carbon were removed by acid treatment. Presence of smaller peaks (labelled as # and * in **Figure 3.6**) in the untreated tubes is due to the residual catalyst and CaO. The disappearance of these peaks after washing (XRD pattern of the fN-MWCNTs) demonstrates a significant removal of these impurities. The presence of Fe (110) peak in the pattern of purified tubes suggests that not all the iron was removed; however, significant amount of the impurities was removed by acid treatment.

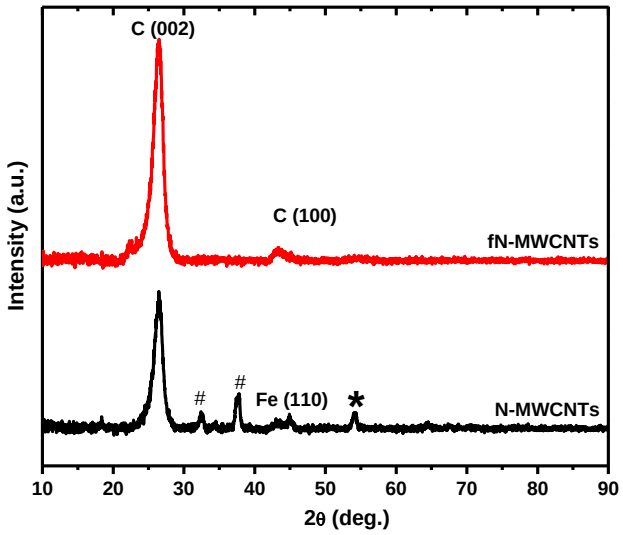


Figure 3.6: X-ray diffraction patterns of acid treated and as-synthesized N-MWCNTs.

Figure 3.7 shows the Raman spectra of both the acid treated and untreated N-MWCNTs, illustrating the presence of two main characteristic peaks of carbon at 1344-1347 cm^{-1} and 1575 cm^{-1} due to the D and G band, respectively. The area ratio of these two peaks depicts the defects in the graphitic structure of the CNTs where the ratio less than 1 shows defect free CNTs whereas the ratio greater than 1 suggests the presence of flaws [29], [30]. The D band occurs because of disorder in the graphene sheets while the G band is due to carbon atom vibrations [31]. Area ratio of the tubes increases from 1.02 to 1.36 upon functionalization, which means that the quality of the tubes decreases, and more defects exist after treatment. This could be because the other graphitic compounds that could have been produced alongside the N-MWCNTs are removed by acid treatment and only the N-MWCNTs remain which have defects due to nitrogen incorporation.

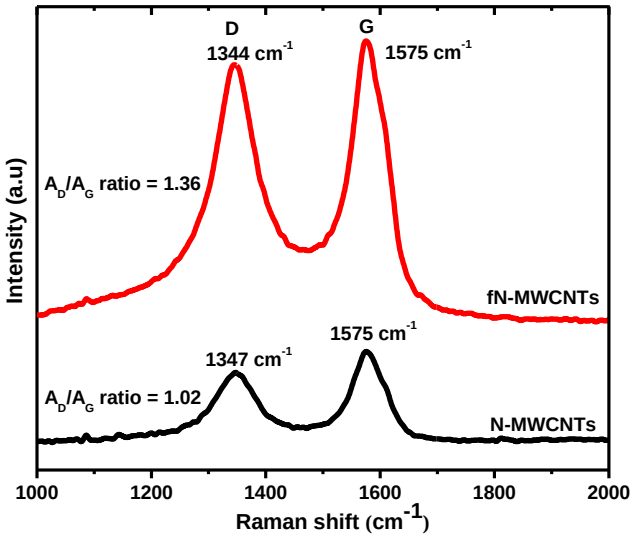


Figure 3.7: Raman spectra of acid treated and as-synthesized N-MWCNTs.

3.5.3 Thermal stability and purity analysis of N-MWCNTs and functionalized N-MWCNTs

Thermal stability and extent of purity of the nanotubes was evaluated by thermogravimetric analysis, which was carried out by heating 10 mg of the samples in air. The TGA profile of the crude N-MWCNTs (**Figure 3.8 (a)**) maintains a 100 % weight below 500 °C and result in a 10 % residual mass after exposure to 900 °C whereas the fN-MWCNTs show a 10 % weight loss in this region and around 2 % residual mass. This is attributed to the detachment of carboxylic acid functional groups that were induced on the nanotube walls during acid treatment and the fact that the N-MWCNTs still contains the catalyst residue which is ultimately removed by acid washing. However, a 2 % residual mass suggests that not all the catalyst was removed as can be seen from both XRD and TEM of fN-MWCNTS in **Figure 3.6** and **Figure 3.9 (c)**.

The presence of a small peak at 400 ºC in the derivative profile of N-MWCNTs shown in **Figure 3.8 (b)** suggests the presence of amorphous carbon which is reported to decompose at around 400 °C [32], [33]. On the other hand, the peak at 670 °C consistent with the peak observed by Mhlanga et al. and is attributed to decomposition of graphitic soot [34], [35]. The derivative weight profile of N-MWCNTs also shows a small mass increase at 450 °C, demonstrating further oxidation of the catalyst metals upon exposure to air. The derivative TGA profile of the fN-MWCNTs shows only one major peak at 650 °C, which is consistent

with results obtained by Tetana et al. for N-MWCNTs, prepared using the same conditions [24].

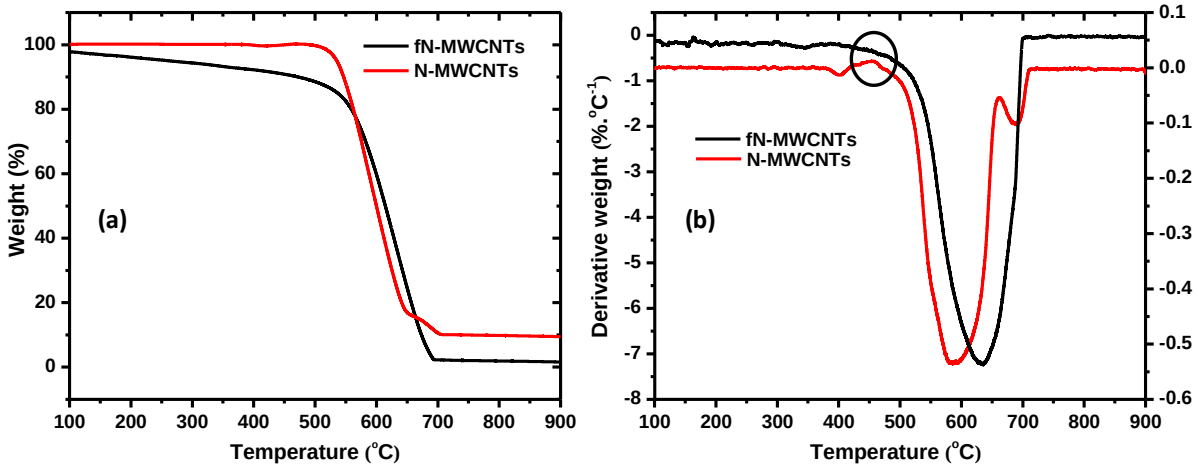


Figure 3.8: (a) Thermograms and (b) corresponding derivative profiles of acid treated and as-prepared N-MWCNTs.

3.5.4 Morphology evaluation of N-MWCNTs and functionalized N-MWCNTs

Refluxing the prepared N-MWCNTs in acid and thereby removing the residual catalyst produces tubes that are less agglomerated, suggested by the SEM images below (**Figure 3.9 (a) and (b)**). Imperfections on the walls of the carbon nanotubes and the tube tips are most prone to oxidative functionalization by acid treatment. The repulsion between these induced functional moieties causes the van der Waals forces that existed between the individual tubes to weaken resulting in less entangled nanotubes as observed on the SEM images [36]. The structure of pristine carbon nanotubes made by Mhlanga et al. using the same method but without a nitrogen source (CH_3CN) exhibits a hollow channel without any compartments [34]. Nitrogen doped CNTs, however, have partitioned tubes referred to as bamboo structures [37]. This morphology difference has been used to identify the success of doping in these materials. The acid treated nitrogen doped CNTs shown in **Figure 3.9 (c)-(e)** have bamboo shapes, various diameters and thick walls as well as open and broken ends. There is no significant difference in the TEM images of N-MWCNTs (**Figure 3.9 (c)**) and fN-MWCNTs (**Figure 3.9 (d)**) thus illustrating that the acid treatment maintains the integrity of the nanotubes. The N-MWCNTs have catalyst particles (marked by black circle in **Figure 3.9 (c)**) still imbedded within the nanotube.

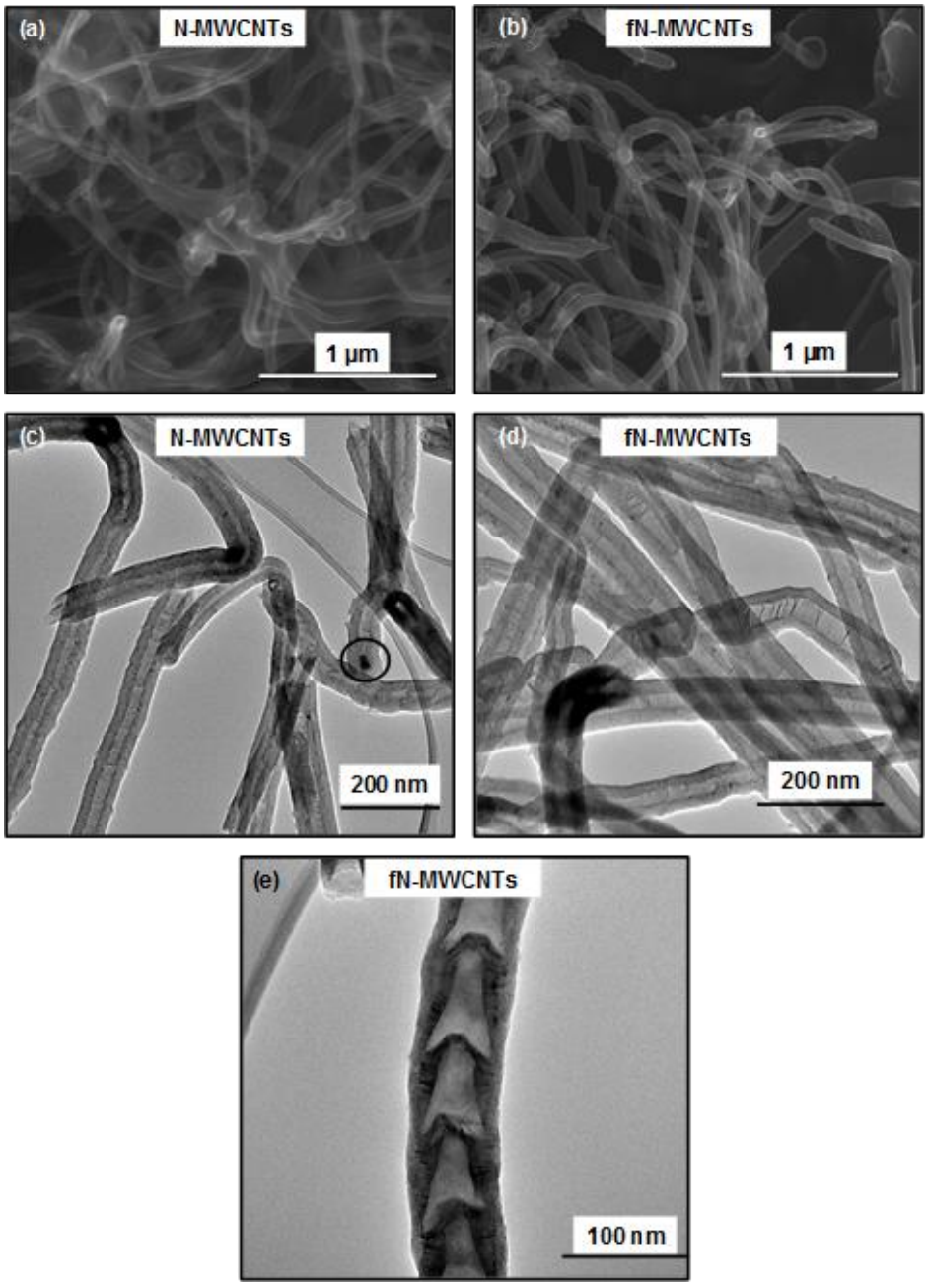


Figure 3.9: (a) and (b) SEM images and (c), (d) and (e) TEM micrographs of nitrogen doped multi-walled carbon nanotubes prior and post acid functionalization.

3.5.5 Elemental composition analysis of functionalized N-MWCNTs

XPS analysis of acid functionalized N-MWCNTs was carried out to determine the elements present in the tubes as well as the overall nitrogen concentration and types of nitrogen bonding configurations obtained upon doping. XPS survey spectrum of the N-MWCNTs is shown in **Figure 3.10 (a)** and reveals the presence of carbon (285 eV), nitrogen (400 eV), oxygen (520 eV) and calcium (350 eV). Carbon and nitrogen are due to graphitic network of sp^2 hybridized carbons that make up the carbon nanotubes and doping using acetonitrile,

respectively. Oxygen is due to the carboxylic and alcohol functional groups induced on the surface of the tubes by acid treatment while calcium may be due to residual CaO from the oxidized catalyst support used in the synthesis of the nanotubes. **Table 3.1** shows the summary of the peak analysis results obtained from XPS as well as elemental (C and N) percentage composition obtained from CN analysis. The overall carbon and nitrogen percentage in the N-MWCNTs estimated from XPS is 78.3 % and 3.8 %, respectively, which is in accordance with 79.83 % (C) and 2.75 % (N) estimated from CN elemental analysis.

Table 3.1: Summary of CN elemental and XPS data of functionalized N-MWCNTs

Elements	Atomic % (CN analysis)	Atomic % (XPS)	Binding energy (eV)	Peak assignment
		63.5	284.3	Graphitic (C-C)
C	79.83	9.6	284.8	Hydroxyl (C-O)
		5.2	288.2	Carboxylic (O-C=O)
N	2.75	1.0	405.6	Molecular nitrogen
		1.7	400.4	Quaternary nitrogen
		1.1	397.9	Pyridinic nitrogen
		6.7	531.1	Carbonyl (C=O)
O	-	10.6	532.5	Alcohol (C-O)

The XPS high-resolution spectrum **(Figure 3.10 (b) & (d))** of C 1s reveals presence of both carboxylic and hydroxyl carbon species at 288 eV and 284 eV respectively. While O 1s shows carbonyl and carboxylic oxygen species at 531 eV and 532 eV respectively. This collectively proves the presence of carboxylic and alcohol groups on the surface of the N-MWCNTs induced by acid functionalization. The carboxylic acid functionality will be exploited as an active site for the attachment of Cu_2ZnSnS_4 in the nanocomposite preparation CZTS/N-MWCNTs. The type of bonding configurations that occur when nitrogen atom integrates the graphitic layers of the nanotubes are pyridinic, quaternary and pyrrolic as shown in **Figure 3.1** and are identified by deconvolution of N 1s peak. The deconvolution of N 1s peak reveals three peaks at 405.6, 400.4, and 397.9 eV which correspond to molecular, quaternary and pyridinic nitrogen atoms respectively. This data is in line with the results previously reported by various researchers [37]. Of the three types of nitrogen detected by XPS, the quaternary nitrogen has the highest atomic percentage of 1.7 %. This suggests that

doping with nitrogen at 800 ºC produced a higher concentration of nitrogen bonded to three carbon atoms. The second highest nitrogen coordination observed is the pyridinic form at 1.1%. In this configuration, nitrogen is bonded to two carbon atoms, has a lone electron pair, and is the basis of metallic conductivity property of the N-CNTs. The presence of this type of nitrogen suggests that incorporation of nitrogen can improve the electron transport properties of the CNTs, which can ultimately improve electron conductivity of CZTS/N-MWCNTs nanocomposite. The total nitrogen atomic concentration from XPS data is 3.8 %, which is greater than that estimated by CN elemental analysis of 2.75 %. This difference may be due to non-uniform doping of the carbon nanotubes.

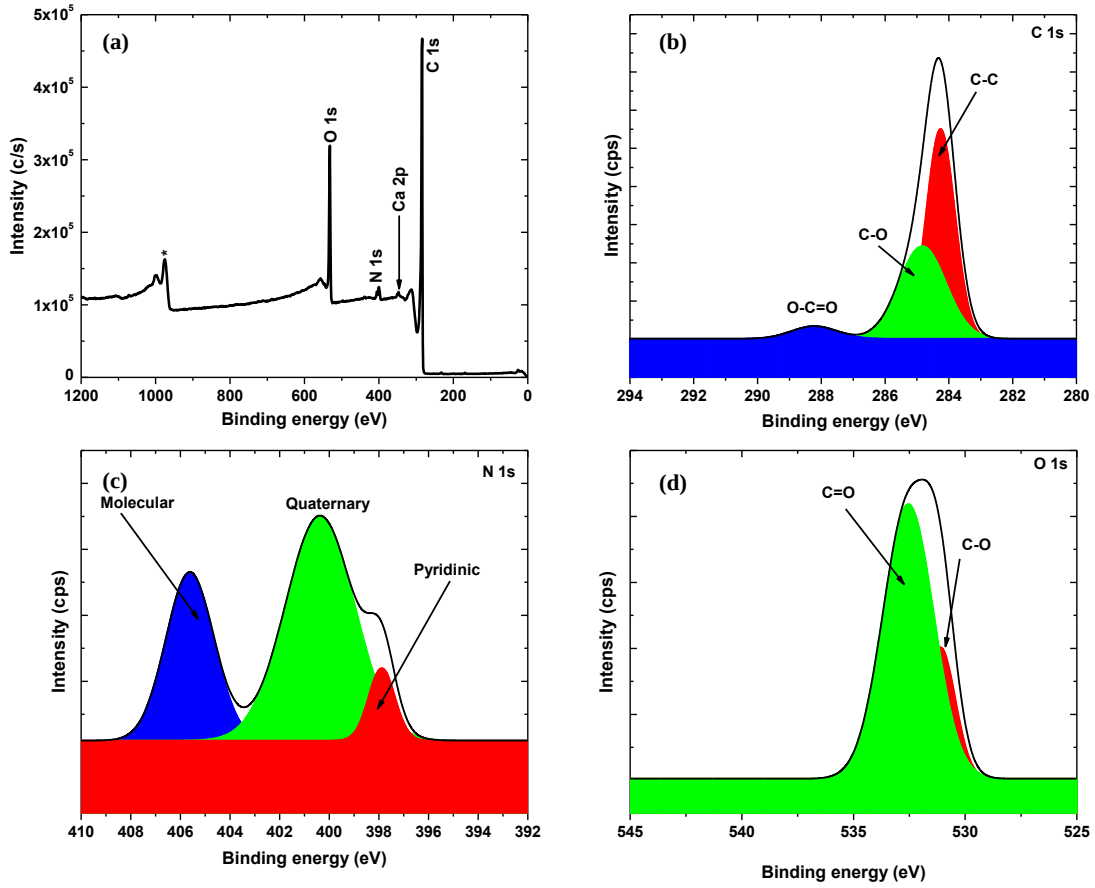


Figure 3.10: (a) XPS survey spectrum of acid treated N-MWCNTs and (b)-(d) high-resolution spectra of carbon, nitrogen and oxygen, respectively.

3.6 Conclusions

This study has shown reproducibility of the previously optimized CVD method for preparation of N-MWCNTs over Fe-Co/$CaCO_3$, efficiency of acid treatment to remove residual catalyst and the type of nitrogen bonding environments in the nitrogen doped multi-walled carbon nanotubes. Comparing the TGA profiles and XRD patterns of the nanotubes

before and after acid treatment demonstrates that the washing did remove most of the catalyst residue as well as other side products that were formed alongside the N-MWCNTs. The increase in the I_d/I_g ratio of fN-MWCNTs further supports the suggestion that other carbon materials were present in the nanotubes but were removed by acid and mostly the defected N-MWCNTs remain. Acid washing does not destroy the morphology of the nanotubes as seen from the TEM images. XPS and CN elemental analysis of the N-MWCNTs shows successful doping of the carbon nanotubes with nitrogen and the deconvoluted nitrogen 1s spectrum shows that three types of nitrogen atoms result, with the quaternary being the most abundant.

3.7 References

[1] M. A. M. Motchelaho, H. Xiong, M. Moyo, L. L. Jewell, and N. J. Coville, "Effect of acid treatment on the surface of multiwalled carbon nanotubes prepared from Fe-Co supported on $CaCO_3$: Correlation with Fischer-Tropsch catalyst activity," *Journal of Molecular Catalysis A: Chemical*, vol. 335, no. 1-2, pp. 189-198, 2011.

[2] O. Stephan, P. M. Ajayan, C. Collix, P. Redlich, J. M. Lambert, P. Bernier and P. Lefin, "Doping graphitic and carbon nanotube structures with boron and nitrogen," *Science*, vol. 266, pp. 1683-1685, 1994.

[3] V. Stefov, M. Najdoski, G. Bogoeva-Gaceva, and A. Buzarovska, "Properties assessment of multiwalled carbon nanotubes: A comparative study," *Synthetic Metals*, vol. 197, pp. 159-167, 2014.

[4] K. Gong, F. Du, Z. Xia, M. Durstock, and L. Dai, "Nitrogen-doped carbon nanotube arrays with high electrocatalytic activity for oxygen reduction," *Science*, vol. 323, pp. 760-764, 2009.

[5] Y. Wang, X. Wang, and M. Antonietti, "Polymeric graphitic carbon nitride as a heterogeneous organocatalyst: From photochemistry to multipurpose catalysis to sustainable chemistry," *Angewandte Reviews*, vol. 51, pp. 68-89, 2012.

[6] A. Abdelhalim, A. Abdellah, G. Scarpa, and P. Lugli, "Metallic nanoparticles functionalizing carbon nanotube networks for gas sensing applications," *Nanotechnology*, vol. 25, no. 5, pp. 1-10, 2014.

[7] S. M. Saha, R. Li, and X. Sun, "High loading and monodispersed Pt nanoparticles on multiwalled carbon nanotubes for high performance proton exchange membrane fuel cells," *Journal of Power Sources*, vol. 177, pp. 314-322, 2008.

[8] X. Sun, R. Li, D. Villers, and J. P. Dodelet, "Composite electrodes made of Pt nanoparticles deposited on carbon nanotubes grown on fuel cell backings," *Chemical*

Physics Letters, vol. 379, pp. 99-104, 2003.

[9] M. Scardamaglia, C. Struzzi, F. J. A. Rebollo, P. D. Marco, P. R. Mudimela, J. F. Colomer, M. Amati, L. Gregoratti, L. Petaccia, R. Snuders and C. Bittencourt, "Tuning electronic properties of carbon nanotubes by nitrogen grafting: Chemistry and chemical stability," *Carbon*, vol. 83, pp. 118-127, 2015.

[10] Q. Wei, X. Tong, G. Zhang, J. Qiao, Q. Gong, and S. Sun, "Nitrogen-doped carbon nanotube and graphene materials for oxygen reduction reactions," *Catalysts*, vol. 5, pp. 1574-1602, 2015.

[11] S. Van Dommele, K. P. De Jong, and J. H. Bitter, "Nitrogen-containing carbon nanotubes as solid base catalysts," *Chemical Communications*, no. 46, pp. 4859-4861, 2006.

[12] M. T. Bankole, I. A. Mohammed, A. S. Abdulkareem, J. O. Tijani, S. S. Ochigbo, O. K. Abubakre and A. S. Afolabi, "Optimization of supported bimetallic (Fe-Co/$CaCO_3$) catalyst synthesis parameters for carbon nanotubes growth using factorial experimental design," *Journal of Alloys and Compounds*, vol. 749, pp. 85-102, 2018.

[13] H. Liu, Y. Liu, and D. Zhu, "Chemical doping of graphene," *Journal of Materials Chemistry*, vol. 21, no. 10, pp. 3335-3345, 2011.

[14] P. Ayala, R. Arenal, M. Rümmeli, A. Rubio, and T. Pichler, "The doping of carbon nanotubes with nitrogen and their potential applications," *Carbon*, vol. 48, no. 3, pp. 575-586, 2010.

[15] C. Liu, Y. Y. Fan, M. Liu, H. T. Cong, H. M. Cheng, and M. S. Dresselhaus, "Hydrogen storage in single-walled carbon nanotubes at room temperature," *ChemInform*, vol. 31, pp. 1127-1129, 1999.

[16] X. Mathebula, "Photocatalytic degradation of methyl violet in water using TiO_2/cellulose-N-MWCNTs," Thesis, 2018.

[17] Y. Xiong, Z. Li, Q. Guo, and Y. Xie, "Synthesis of multi-walled and bamboo-like well-crystalline CN_x nanotubes with controllable nitrogen concentration (x=0.05-1.02)," *Inorganic Chemistry*, vol. 44, no. 19, pp. 6506-6508, 2005.

[18] M. Reyes-reyes, N. Grobert, R. Kamalakaran, T. Seeger, D. Golberg, and M. Ru, "Efficient encapsulation of gaseous nitrogen inside carbon nanotubes with bamboo-like structure using aerosol thermolysis," *Chemical Physics Letters*, vol. 396, pp. 167-173, 2004.

[19] R. Purohit, K. Purohit, S. Rana, R. S. Rana, and V. Patel, "Carbon nanotubes and their growth methods," *Procedia Materials Science*, vol. 6, pp. 716-728, 2014.

[20] E. Couteau, K. Hernadi, J. W. Seo, L. Thiên-Nga, Cs. Mikó, R. Gaál and L. Forró, "CVD synthesis of high-purity multiwalled carbon nanotubes using $CaCO_3$ catalyst support for large-scale production," *Chemical Physics Letters*, vol. 378, pp. 9-17, 2003.

[21] A. S. Abdulkareem, I. Kariim, M. T. Bankole, J. O. Tijani, T. F. Abodunrin, and S. C. Olu, "Synthesis and characterization of tri-metallic Fe-Co-Ni catalyst supported on $CaCO_3$ for multi-walled carbon nanotubes growth via chemical vapor deposition technique," *Arabian Journal for Science and Engineering*, vol. 42, pp. 4365-4381, 2017.

[22] A. Pander, A. Hatta, and H. Furuta, "Optimization of catalyst formation conditions for synthesis of carbon nanotubes using Taguchi method," *Applied Surface Science*, vol. 371, pp. 425-435, 2016.

[23] J. Cheng, X. Zhang, Z. Luo, F. Liu, Y. Ye, W. Yin, W. Liu and Y. Han, "Carbon nanotube synthesis and parametric study using $CaCO_3$ nanocrystals as catalyst support by CVD," *Materials Chemistry and Physics*, vol. 95, no. 1, pp. 5-11, 2006.

[24] Z. N. Tetana, S. D. Mhlanga, G. Bepete, and N. J. Coville, "The synthesis of nitrogen-doped multiwalled carbon nanotubes using an Fe-Co/$CaCO_3$ catalyst," *South African Journal of Chemistry*, vol. 65, pp. 39-49, 2012.

[25] I. K. Song, Y. S. Cho, G. S. Choi, J. B. Park, and D. J. Kim, "The growth mode change in carbon nanotube synthesis in plasma-enhanced chemical vapor deposition," *Diamond and Related Materials*, vol. 13, no. 4-8, pp. 1210-1213, 2004.

[26] L. Guo, V. Shanov, and R. N. Singh, "Nucleation and growth of carbon nanotubes by microwave plasma chemical vapor deposition," *Ceramic Transactions*, vol. 159, pp. 177-183, 2005.

[27] M. Kumar, "Carbon nanotube synthesis and growth mechanism," *Nanotechnology Perceptions*, vol. 6, no. 1, pp. 7-28, 2012.

[28] K. Kalyanasundaram, J. Kiwi, and M. Grätzel, "Hydrogen evolution from water by visible light, a homogeneous three component test system for redox catalysis," *Helvetica Chimica Acta*, vol. 61, no. 7, pp. 2720-2730, 1978.

[29] S. D. Mhlanga, E. N. Nxumalo, N. J. Coville, and V. V. Srinivasu, "Nitrogen doping of CVD multiwalled carbon nanotubes: Observation of a large g-factor shift," *Materials Chemistry and Physics*, vol. 130, pp. 1182-1186, 2011.

[30] J. Cheng, X. Zhang, F. Liu, J. Tu, H. Lu, Y. Sun and F. Chen, "Long bundles of aligned carbon nanofibers obtained by vertical floating catalyst method," *Materials*

Chemistry and Physics, vol. 87, no. 2-3, pp. 241-245, 2004.

[31] H. Hiura, T. W. Ebbesen, K. Tanigaki, and H. Takahashi, "Raman studies of carbon nanotubes," *Chemical Physics Letters*, vol. 202, no. 6, pp. 509-512, 1993.

[32] Z. Shi, Y. Lian, F. H. Liao, X. Zhou, Z. Gu, Y. Zhang, S. Lijima, H. Li, K. T. Yue and S. -L. Zhang, "Large scale synthesis of single-wall carbon nanotubes by arc-discharge method," *Journal of Physics and Chemistry of Solids*, vol. 61, no. 7, pp. 1031-1036, 2000.

[33] B. J. Landi, C. D. Cress, C. M. Evans, and R. P. Raffaelle, "Thermal oxidation profiling of single-walled carbon nanotubes," *Chemistry of Materials*, vol. 17, no. 26, pp. 6819-6834, 2005.

[34] S. D. Mhlanga, K. C. Mondal, R. Carter, M. J. Witcomb, and N. . Coville, "The effect of synthesis parameters on the catalytic synthesis of multiwalled carbon nanotubes using Fe-Co/$CaCO_3$ catalysts," *South African Journal of Chemistry*, vol. 62, pp. 67-76, 2009.

[35] "Pyrolysis of heavy oil in the presence of supercritical water: The reaction kinetics in different phases," *AICHE Journal*, vol. 61, no. 3, pp. 857-866, 2015.

[36] V. Choudhary, B. P. Singh and R. B. Mathur, (2013) "Synthesis and applications of carbon nanotubes and their composites," IntechOpen. *Science*.

[37] L. S. Panchakarla, A. Govindaraj, and C. N. R. Rao, "Boron- and nitrogen-doped carbon nanotubes and graphene," *Inorganica Chimica Acta*, vol. 363, no. 15, pp. 4163-4174, 2010.

[38] I. M. Rocha, O. S. G. P. Soares, D. M. Fernandes, C. Freire, J. L. Figueiredo, and M. F. R. Pereira, "N-doped carbon nanotubes for the oxygen reduction reaction in alkaline medium: Synergistic relationship between pyridinic and quaternary nitrogen," *ChemistrySelect*, vol. 1, pp. 2522-2530, 2016.

Chapter 4 : Colloidal synthesis, surface and structural modification of Cu_2ZnSnS_4

4.1 Introduction

4.1.1 Colloidal synthesis

Hot injection colloidal synthesis is mostly employed to prepare chalcogenides since it offers the ability to tailor the size, composition, shape and phase of the nanoparticles by manipulating the reaction time, temperature, precursor ratios and type of precursors and capping ligands [1–4]. Hot injection involves a swift injection of a cold chalcogen and transition metal precursors into the hot surfactant solution. Metal precursors that can be employed include metal chlorides, acetates and acetylacetonates and exhibit diverse dissociation degrees in the coordinating ligand [5]. Oleylamine is often used as both a reaction medium and coordinating solvent in chalcogenide colloidal synthesis because it has a relatively high boiling temperature and high coordinating affinity to chalcogenides [6]. The formation of nanoparticles using this procedure is explained by nucleation and growth processes within the hot solvent (**Figure 4.1**). When the cold precursor solution encounters the hot reaction solvent, the reactant molecules or elements dissociate into monomers from which nuclei are formed. The nuclei come together to minimize energy of the system until stable nuclei are formed. As the amount of monomers drop to form the nuclei, they deplete restricting further growth of the nuclei [7], [8].

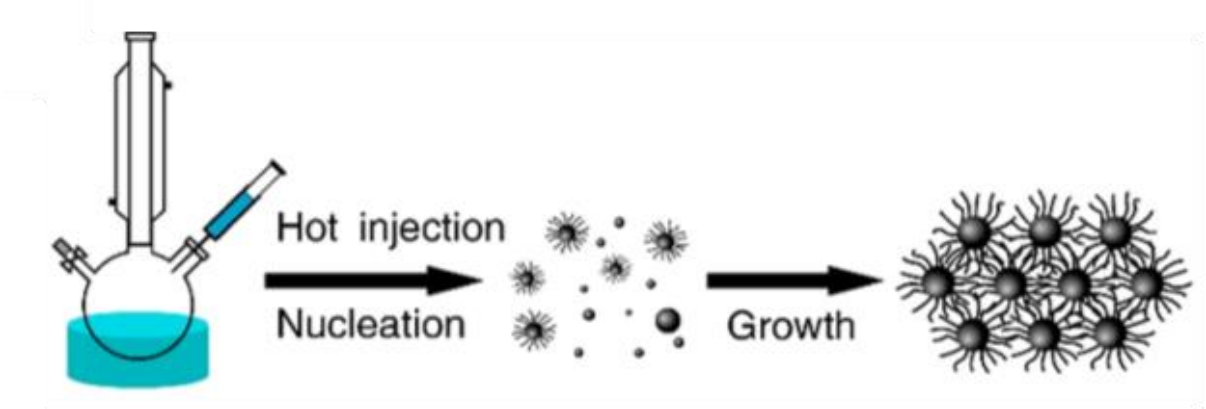


Figure 4.1: Growth mechanism of the nanoparticles during hot injection colloidal synthesis.

Many challenges regarding the morphology and size control of nanoparticles post hydrothermal nanoparticle synthesis methods have been addressed by colloidal synthesis through optimization of reaction parameters such as temperature, precursor concentration and

reaction time. Organic solvents with long alkyl chains such as oleylamine (OLA) and trioctylphosphine oxide (TOPO) are exploited in colloidal synthesis to further control particle size and prevent clustering of nanoparticles [9], [10]. However, parameter optimization is tedious and consumes a lot of time, thus, post treatment of the as-prepared poly-dispersed colloids can be carried out to manipulate the size and shape of the synthesized colloids. Digestive ripening and Ostwald ripening are some of the popular techniques that can be performed to obtain monodispersed nanoparticles [11]. Additionally, these organic capping agents can be switched with shorter, more hydrophilic/hydrophobic or bidentate ligands to afford better dispersion of the nanoparticles in preferred solvents and functionality through a procedure referred to as ligand exchange.

4.1.2 Digestive ripening

Digestive ripening is a post synthesis treatment method that involves heating a poly-dispersed colloid in an excess surfactant (digestive ripening agent, DRA) near its boing point for a specific time to obtain particles that have a small size distribution [12]–[14]. One of the theories behind this process suggests that defects in the large particles serve as micro stress points thereby reducing the lattice stabilization energy. These defects act as attachment sites, which ultimately cause the particles to dissociate in the presence of a DRA [11], [12]. Alternatively, the ligand can initiate etching out of atoms from the large particles during refluxing [15]. The etched atoms are deposited onto the smaller particles to form more thermodynamically stable nanoparticles. The blending of these two processes produces monodispersed particles with sizes transitional to the initially small and large ones [12].

The type of coordinating ligand, reflux temperature as well as the duration of the ripening process are major contributing factors to the final size distribution of the nanoparticles. Various ligands containing sulfur, phosphorus, nitrogen, oxygen and silicon functionalities such as alkyl thiols, amines, silanes, phosphines, alcohols, halides, alkanes have been studied as candidates for digestive ripening of gold nanoparticles [16]. Of these, only thiols, amines, silanes, and phosphines were found to be active ripening ligands [16] which led to the conclusion that the active group on the ligand and the extent of interaction with the nanoparticles determines the final size of the particles. Prasad et al. evaluated the applicability of alkyl thiols as DRAs and the effect of alkyl chain in alkyl thiols (1-octanethiol, 1-decanethiol, 1-hexadecanethiol) on the final size distribution of gold nanoparticles. The authors reported that these thiols are active as ripening agents and the final

size distribution of the nanoparticles is dependent on the alkyl chain in the thiol, and particle size increases with increasing chain length [13]. Reports on the temperature and duration of ripening process reveal that at elevated temperatures, Ostwald ripening dominates, and particles become highly aggregated. Refluxing at low temperatures, a narrow size distribution that was independent on increased reflux time was observed within one hour of heating [12].

4.1.3 Ligand exchange

DSSC counter electrode fabrication is executed by depositing an ink solution of the CE material on a glass substrate, by either spin coating or drop casting. The ink is prepared by dissolving the CE material in a volatile polar organic solvent. The as-synthesized CZTS nanoparticles are capped by OLA, which prevents particle agglomeration and assists in size control of the nanoparticles during synthesis. OLA binds to the CZTS nanoparticles through the amine head group leaving the long, nonpolar alkyl chain dangling. This then restricts the dissolution of OLA capped CZTS in polar solvents, particularly DMSO which will be employed in ink preparation. OLA ligand can be exchanged for polar and shorter chain bidentate ligands, a phenomenon referred to as surface modification or ligand exchange. Pyridine [17], 3-mercaptopropionic acid (3-MPA) [18] and ethanedithiol (EDT) [19] are some of the popular ligands in nanoparticle surface modification that will be explored for ligand exchange studies in this research. EDT and MPA are bifunctional ligands. The advantage of bidentate ligands in this study, particularly, is the postulation that one group binds to the metal surface while the other one binds to the N-MWCNTs in nano-hybrid preparation, thereby facilitating a better interaction between CZTS and the nanotubes. For instance, the -SH groups in MPA are reported to bind to metal atoms of the quantum dots while the carboxylic acid group attach to titania electrode [20]. On the other hand, pyridine has a shorter alkyl chain relative to OLA and a net polarity exists on this compound when it is bound to the CZTS nanoparticles. The net charge on pyridine ligand is then utilized in the preparation of the nanocomposites. The charge on pyridine initiates electrostatic interaction between the pyridine capped CZTS and the walls of the carbon nanotubes.

Surface alteration of the as-prepared nanoparticles can be achieved by two methods; solid-state and solution based ligand exchange [21]. In solid-state surface modification, the long organic chain ligand capped nanoparticles are deposited onto a substrate, followed by substrate exposure to the shorter chain ligand for a specific time period [22], [23]. The excess ligand solution is then removed by spinning the substrate on a spin coater while the

exchanged ligand is removed by passing aprotic solvent over the substrate [21], which can however also remove the short chain ligand [24]. Solution based ligand exchange entails dispersion of the long alkyl ligand capped particles in a solvent, which is then mixed with a solution of a shorter chain ligand and ligand swap facilitated by stirring. The prepared Cu_2ZnSnS_4 are capped by the long organic OLA ligand. To prepare an ink of the Cu_2ZnSnS_4 and to deposit it on FTO glass for the preparation of the counter electrode, Cu_2ZnSnS_4 must completely dissolve in polar solvents. To facilitate this dissolution, OLA ligand was exchanged for either short alkyl chain ligand of pyridine, or the polar3-MPA and EDT ligands. Different procedures for surface engineering of OLA capped CZTS were employed depending on the coordinating ability of the ligand. Ligand exchange with pyridine involved refluxing because of the weak coordinating ability of pyridine, whereas for 3-MPA and EDT ligand exchange, the mixture of ligand solution and CZTS were stirred at room temperature since these ligands are highly coordinating.

4.2 Materials and methods

4.2.1 Chemicals

The following chemicals were purchased from Sigma-Aldrich and used as is: oleylamine ($C_{18}H_{37}N$, 70%), stannic chloride ($SnCl_4.5H_2O$), zinc chloride ($ZnCl_2$, ≥ 98%), copper (I) chloride (CuCl, ≥ 98%), elemental sulfur, pyridine (C_5H_5N, ≥ 99%), 3-mercaptopropionic acid ($C_3H_6O_2S$, ≥ 99%), 1,2- ethanedithiol (EDT) ($C_2H_6S_2$, ≥ 90%), chloroform ($CHCl_3$), methanol (CH_3OH, ≥ 99.5%), deteriorated-chloroform ($CDCl_3$, ≥ 99.8% D), deteriorated-dimethyl sulfoxide (d_6-DMSO) (C_7D_6OS, ≥ 99.8% D).

4.2.2 Colloidal synthesis of CZTS

Cu_2ZnSnS_4 was prepared using colloidal hot-injection method shown in **Figure 4.2**. For a typical reaction, 24 mL of OLA in a three-neck round bottom flask connected to a Schlenck line was heated and refluxed to 100 °C. Then CuCl, $ZnCl_2$ and $SnCl_4.5H_2O$ were sequentially added. The temperature was then increased to 220 °C, upon which elemental sulfur was added. The color of the solution changed from clear to green upon addition of copper and zinc salts to orange after addition of tin chloride to a black as sulfur was added (**Figure 4.2**). The reaction was run for 45 min after which temperature was lowered to 60 °C, and ethanol added to precipitate the colloidal particles out. The nanoparticles were then isolated by centrifugation for three cycles while washing with ethanol, and then dried at room temperature. ^{1}H-NMR of pure OLA (300 MHz, d-chloroform) δ(ppm): 5.22 (t, 2H, R-

CH=**CH**-CH_2-R), 2.55 (t, 2H, NH_2-**CH_2**-R), 1.90 (d, 4H, R-C=C-**CH_2**-R), 1.18 (t, 29 H, R-(**CH_2**)$_6$-CH_3), 0.76 (m, 3H, R-(CH_2)$_6$-**CH_3**). ^{1}H-NMR as synthesized OLA-CZTS (300 MHz, d-chloroform) δ (ppm): 5.4 (t, 3H, R-CH=**CH**-CH_2-R), 2.0 (s, 4H, R-C=C-**CH_2**-R), 1.3 (s, 12 H, R-(**CH_2**)$_6$-CH_3), 0.8 (m, 3H, R-(CH_2)$_6$-**CH_3**).

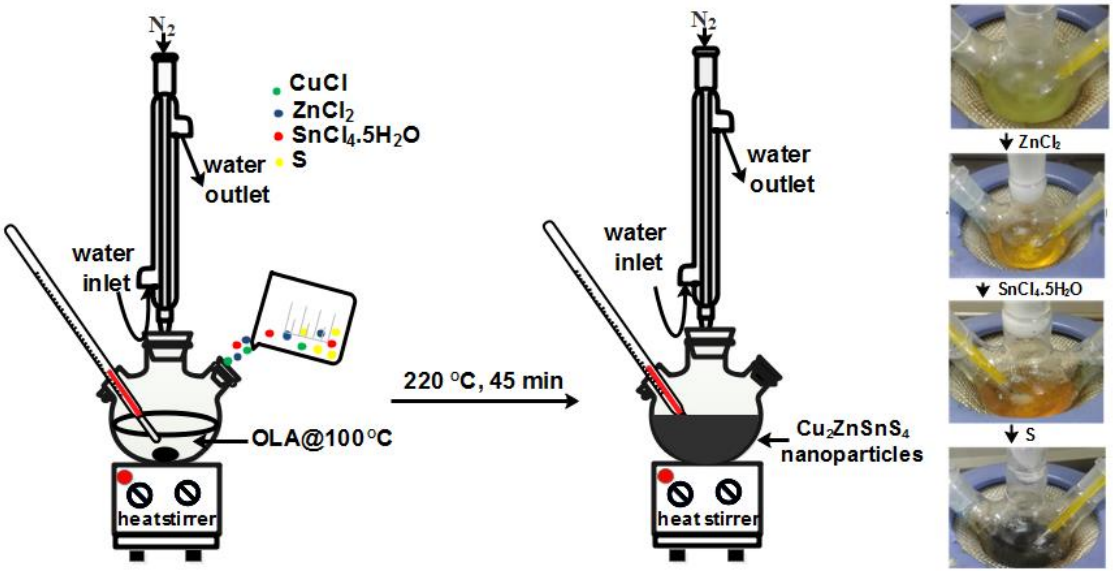


Figure 4.2: Schematic diagram depicting preparation procedure of CZTS and color change upon addition of precursors.

4.2.3 Digestive ripening of CZTS

The as-prepared Cu_2ZnSnS_4 nanoparticles are poly-dispersed and do not have a distinct morphology, therefore digestive ripening of the nanoparticles was carried out in OLA. A molar ratio of 1:30 of the nanoparticles to OLA (ripening agent) was refluxed at 80 °C under vigorous stirring for 5 hours and aliquots taken at 1, 2, 3, 4 and 5 hours. The samples were washed and centrifuged in ethanol for three cycles, and then dried in a fume hood.

4.2.4 Ligand exchange of OLA capped CZTS

Ligand exchange employed in this study involved swapping OLA for pyridine, 3-MPA and 1,2-EDT as shown in **Figure 4.3** below.

Pyridine: 0.25 g of OLA capped CZTS nanoparticles were refluxed in 10 mL of pyridine at 90 °C for 24 hours, and then the temperature dropped to 60 °C. Ethanol was added to precipitate the particles and the particles were isolated from the organic solvents by centrifugation for three cycles at 7000 rpm for 10 minutes. ^{1}H-NMR of pyridine (300 MHz, d-chloroform) δ (ppm): 8.59 (d, 2H, α-N), 7.76 (t, 1H, γ-N), 7.36 (t, 2H, β-N). ^{1}H-NMR of

py-CZTS (300 MHz, d-chloroform) δ (ppm): 8.56 (s, 2H, α-N), 7.63 (t, 1H, γ-N), 7.33 (t, 7H, β-N). This sample will be referred to as py-CZTS.

3-Mercaptopropionic acid and 1,2-ethanedithiol: this procedure was adapted from the ligand exchange procedure carried out by Huang and coworkers on oleic acid capped CdSe nanoparticles [20]. In a typical ligand exchange procedure, a basic solution of 3.44 M 3-MPA (150 μL in 0.5 mL methanol) at pH 12 (adjusted by addition of 40% NaOH) was added dropwise to a solution of OLA capped CZTS (30 mg in 0.5 mL chloroform) while stirring vigorously. The mixture was left to stir at room temperature for 1 hour. The particles were isolated and the excess MPA as well as exchanged ligand (OLA) were removed by centrifugation in acetone for three cycles and left to dry under fume hood. The same procedure was followed for CZTS surface modification with EDT. The basicity of the ligand solution serves to facilitate binding of the ligand to the quantum dots by deprotonating the thiol groups [25].^{1}H NMR of free MPA (300 MHz, d-DMSO) δ (ppm): 2.60 (q, 2H, HS-**C**$\mathbf{H_2}$-CH_2-COOH), 2.52 (t, 2H, HS-CH_2-**C**$\mathbf{H_2}$-COOH), 2.05 (t, 1H, **HS**-CH_2-COOH). ^{1}H-NMR of MPA-CZTS (300 MHz, d-DMSO) δ (ppm): 2.54 (s, 1H, HS-CH_2-**C**$\mathbf{H_2}$-COOH), 2.08 (s, 1H, **HS**-CH_2-COOH). ^{1}H-NMR of EDT (300 MHz, d-DMSO) δ (ppm): 2.73 (t, HS-CH_2-**C**$\mathbf{H_2}$-SH). ^{1}H-NMR of EDT-CZTS (300 MHz, d-DMSO) δ (ppm): 2.92 (s, HS-CH_2-**C**$\mathbf{H_2}$-SH). MPA and EDT capped CZTS will be referred to as MPA-CZTS and EDT-CZTS, respectively.

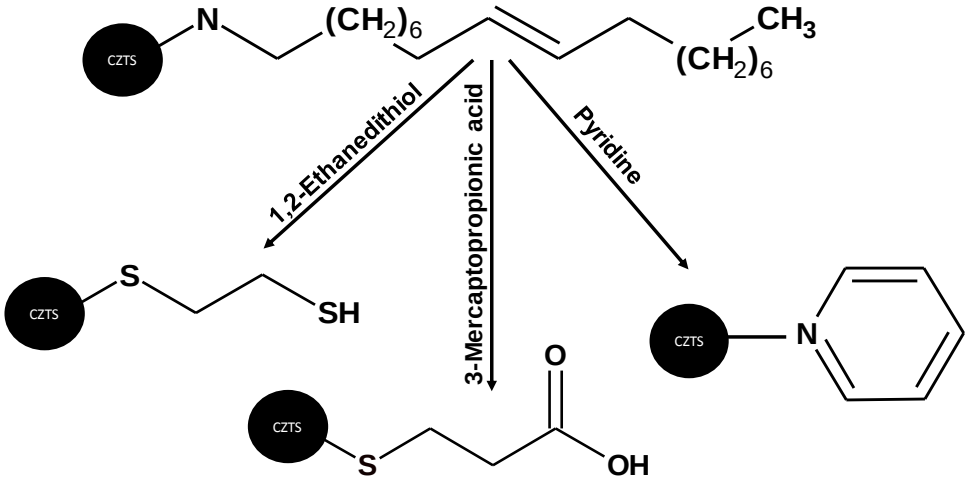


Figure 4.3: Schematic diagram depicting target ligand switching.

4.2.5 Characterization

X-ray diffraction patterns of the CZTS nanocrystals were analyzed by Bruker D2 Phaser Powder X-ray diffractometer. Raman spectroscopy using a John-Yvon T64000 micron

Raman spectrophotometer was used as to examine the phase purity of the prepared nanoparticles. Morphology of the nanoparticles was evaluated by Scanning electron microscope (SEM) analyzed using FEI Nova Nanolab 600 SEM operated at 30 kV on samples dispersed on carbon tape and coated twice with carbon, and transition electron microscopy (TEM) performed on FEI Technai T12 TEM microscope carried out at 120 kV acceleration voltage beam spot sized of 20-100 nm in TEM mode. TEM samples were prepared by refluxing the nanoparticle powder under excessive stirring at 50 °C for 30 minutes. TEM was also used to evaluate the change in morphology at increasing time intervals of the digestive ripening process. The bonding mode of the OLA on CZTS nanoparticles as well as tracking of ligand exchange was achieved by FTIR recorded on FT-IR Bruker spectrophotometer using ATR and proton NMR spectroscopy recorded on Bruker Avance 500 MHz spectrometer. NMR samples were prepared by sonicating the powders in deteriorated NMR solvents. XPS analysis of the obtained samples was done on Thermo Scientific ESCAlab 250Xi using a 300 W Monochromatic Al kα (1486.7 eV) X-ray beam with a diameter of 900 µm.

4.3 Results and discussion

4.3.1 Structural properties of CZTS

The XRD pattern of Cu_2ZnSnS_4 (**Figure 4.4**) shows three major peaks at 2θ = 28°, 47° and 56° which are attributed to the [112], [220] and [312] crystal planes respectively. All the peaks are characteristic of Cu_2ZnSnS_4 and match to kesterite Cu_2ZnSnS_4 (JCPDS no. 01-075-4122). The crystallite diameter (D) was estimated to be 23 ± 1 nm from the three most intense peaks using Scherrer`s equation below.

$$\mathbf{D = \frac{k\lambda}{\beta cos\theta}}$$ ----------**Equation 4.1**

Where D is crystallite diameter, $\boldsymbol{\lambda}$ is the XRD wavelength = 1.5406 Å, β = peak width at half maximum (in radians), k = 0.9 (shape factor) and θ = the angle of reflection.

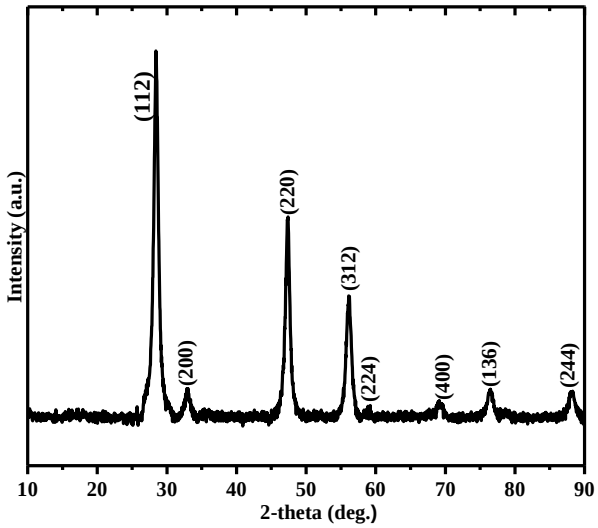


Figure 4.4: X-ray diffraction pattern of CZTS.

Raman spectroscopy is used as an identification method of CZTS and a tool to determine the phase purity of the nanoparticles. The Raman spectrum of CZTS nanoparticles is shown in Figure 4.5. The most intense peak for CZTS is reported at around 335 cm^{-1} and attributed to the breathing mode of sulfur atoms in mode A [26], [27] while the second most intense peak is around 295 cm^{-1}. This second peak occurs because of kesterite vibration mode A. Shoulder peaks at this vibration are characteristic of kesterite CZTS. The as-prepared CZTS Raman spectra shows the presence of this peaks but appear at lower Raman shifts. This shift is assigned to several factors such as presence of surfactant molecules, local variation in sulfur concentrations and strain in the material [17]. The absence of any more peaks confirms the that there is only kesterite CZTS available in the sample, otherwise common competing products peaks of Cu_3ZnS_4, Cu_2SnS_3 and ZnS would have been observed at 320 cm^{-1}, 298 cm^{-1} and 351 cm^{-1} respectively [28], [29]. Interesting also, is the presence of the carbon peaks between 400 cm^{-1} and 1800 cm^{-1} in the CZTS sample. This suggests the presence non-graphitic carbonaceous material within the CZTS sample due to the presence of oleylamine in the CZTS sample. The Raman spectra of chalcogenides prepared in a capping ligand reported in most articles only show the spectra to not more than 600 wavenumbers [30]–[33].

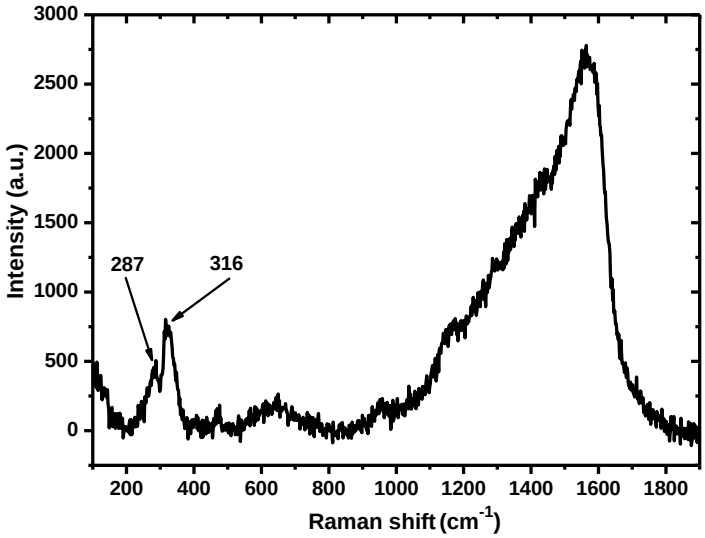


Figure 4.5: Raman spectrum of as-synthesized CZTS.

4.3.2 Surface evaluation of CTZS

The CZTS colloid is prepared in OLA, which acts as a capping agent, a solvent and a reagent to activate the precursors by donating electrons to them at high temperatures. OLA facilitates dissolution of the nanoparticles in organic solvents. The extent to which OLA capped the CZTS was evaluated by both FTIR and NMR spectroscopy. **Figure 4.6** shows the overlaid FTIR spectra of pure OLA, OLA capped CZTS and an insert of the structure of OLA. The spectrum of OLA shows the high intensity symmetric and asymmetric C-H bond stretches between 2750 cm^{-1} and 3000 cm^{-1} which result from CH_2 groups. The second most intense peak at 1500 cm^{-1} is attributed to alkane C-H bond stretches at the tail of the OLA structure. The amine functionality bond vibrations and stretches are observed at around 880 cm^{-1} (N-H) and 1100 cm^{-1} (C-N). What is evident in the spectrum of OLA-CZTS is that the intensity of the peaks has diminished immensely.

The nanoparticles have a high density and induce strain on the ligand thereby causing the vibrations in the ligand to either need a higher energy for them to occur, or their intensity to decrease. However, an overlap of the CH_2, CH_3 and C=C bond stretches of pure OLA with the spectrum of OLA-CZTS suggests that this ligand is present in the nanoparticles. What is also evident is the slight shift to higher wavenumber of the C=N bond stretch from the spectrum of uncapped OLA to that of OLA capped CZTS and could support the postulation that the nanoparticles attach on the amine head group of the ligand [34]. The observed O=C=O is due to atmospheric CO_2. To further verify the binding mode of OLA to CZTS, proton NMR of both the species was run.

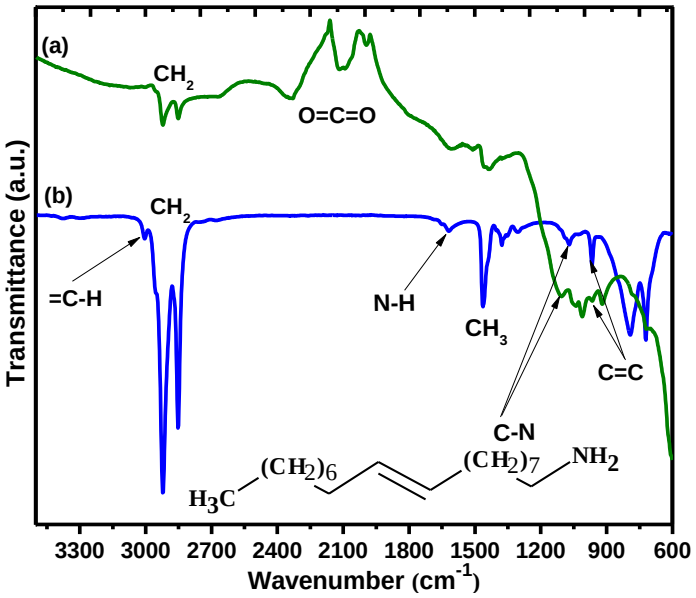


Figure 4.6: FTIR spectra of (a) OLA capped CZTS and (b) pure OLA.

The ^{1}H NMR spectra of both the OLA and OLA capped Cu_2ZnSnS_4 is shown in **Figure 4.7** below. OLA has 5 types of nitrogen environments, namely; amine ($R\text{-}NH_2$), alkyl, vinylic, allylic and carbon hydrogens α to nitrogen. However, the amine proton signal is usually either broad or does not appear in the spectrum. Amine protons can be interchanged with deuterium (^{2}H) from the deteriorated NMR solvent, thereby causing the peak due to these protons to disappear. Therefore, the signals observed in the ^{1}H spectrum of OLA were attributed to the alkyl, vinylic, allylic and hydrogen bonded to carbon α to the amine functionality. Nonetheless, there are two types of alkyl protons present in the OLA structure, the methyl and methylene protons, which then suggest that at least 5 signals can be expected in the ^{1}H NMR spectrum of OLA. The capping of nanoparticles with OLA will shield the protons from the magnetic field resulting in a peak shift or peak broadening to signals due to protons closest to the nanoparticles. The decrease in multiplicity in the ^{1}H NMR peaks of OLA-CZTS suggests an interaction between the ligand and the CZTS nanoparticles. A drastic decrease and shift from 2.55 ppm in the free OLA in the intensity of the protons α to amine group to 2.69 ppm in OLA-CZTS spectrum implies that the nanoparticles are close to this functional group and most probably attached to it. The above observations therefore confirm that OLA binds to the CZTS nanoparticles through the amine head group of OLA.

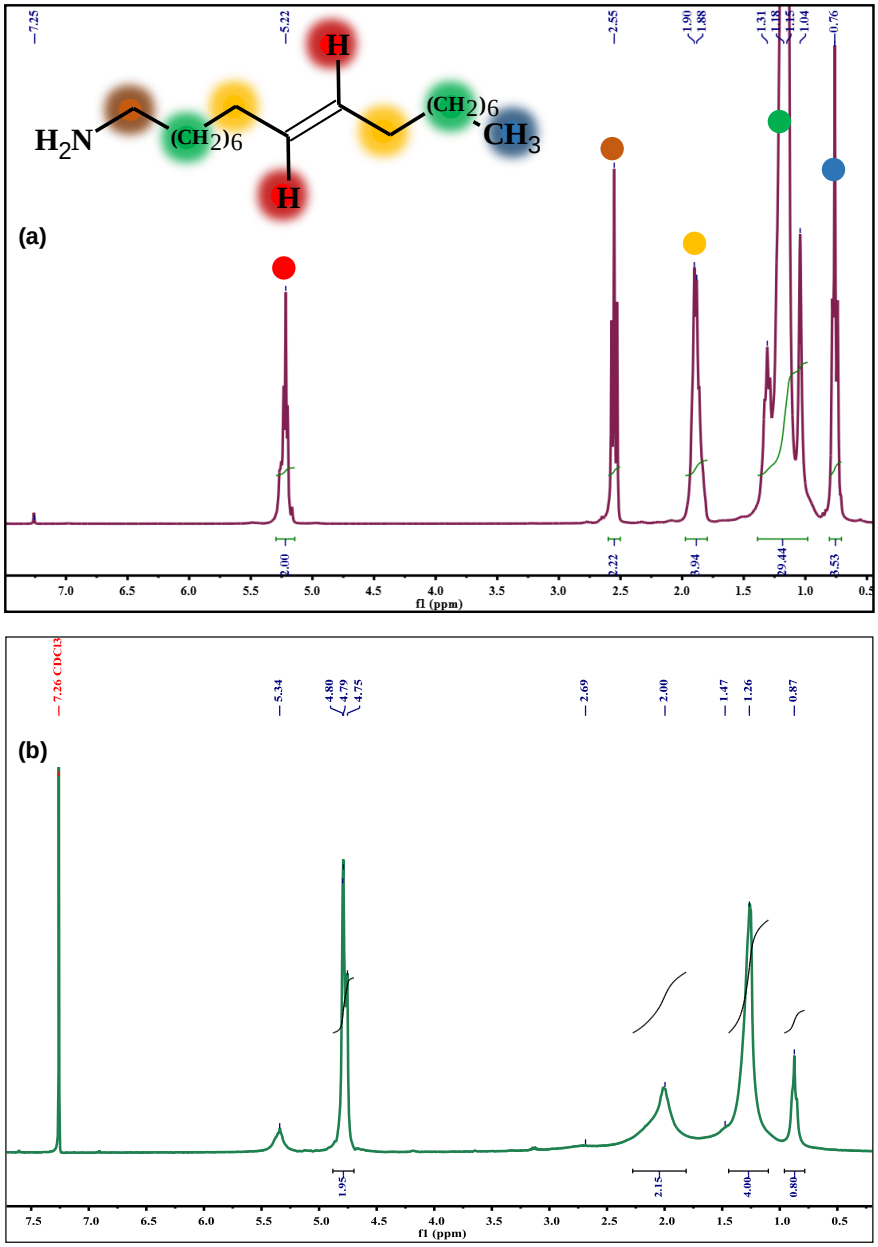


Figure 4.7: ^{1}H NMR spectrum of (a) pure OLA and (b) OLA capped CZTS.

4.3.3 Elemental composition of as-synthesized CZTS

XPS is an atomic layer evaluation technique often used as both a purity and composition tool. The survey spectrum of CZTS (**Figure 4.8**) shows presence of zinc, copper, oxygen, tin, nitrogen, carbon and sulfur atoms. Copper, zinc, tin and sulfur atoms make up the quaternary chalcogenide synthesized from the chloride salt precursors and elemental sulfur. CZTS was prepared in a coordinating organic ligand (OLA). OLA is a hydrocarbon compound with an anime functional group. The carbon and nitrogen atoms detected from the XPS survey spectrum can therefore be attributed to OLA, which is assumed to cover the inorganic core. Detection of carbon and nitrogen in the XPS survey spectrum of CZTS is further

confirmation of the successful formation of OLA capped CZTS nanoparticles. The detected oxygen is usually due to the oxidation of the organic ligand [44], [45].

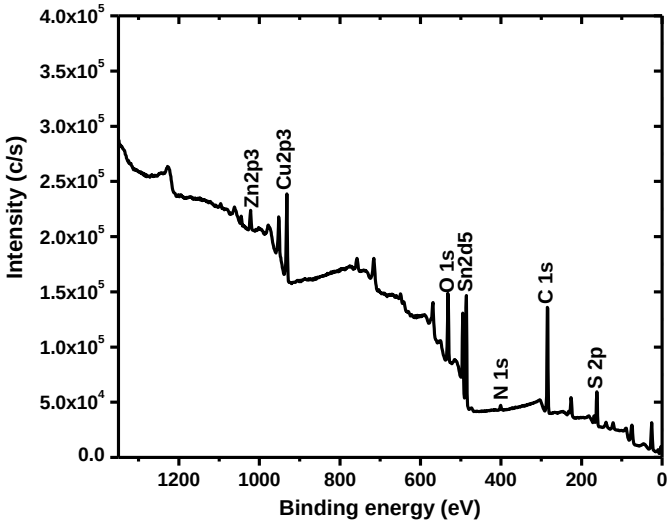


Figure 4.8: XPS survey spectrum of CZTS nanoparticles synthesized in OLA.

The high resolution XPS of the individual elements was carried out to identify the type of species present in the CZTS sample. The anticipated valence states of copper, zinc, tin and sulfur atoms in CZTS are +1, +2, +4 and -2, respectively. The Cu 2p scan (**Figure 4.9 (a)**) revealed two peaks at 931.4 eV and 952.2 eV which correspond to the Cu $2p_{3/2}$ and Cu $2p_{1/2,}$ respectively with the energy difference of 19.8 eV. This observation suggests that the copper within CZTS has an oxidation number of +1 [35], [36]. The absence of a peak at 942 eV in this spectrum allows us to rule out the presence of the common competing products for CZTS ternary Cu^{2+} compounds that would otherwise have not been detected by XRD [37]. The Zn 2p spectrum (**Figure 4.9 (b)**) also shows two distinct peaks at 1021.8 eV due to Zn $p_{3/2}$ and 1044.8 eV from Zn $2p_{1/2}$ with a peak splitting of 23.13 eV. These results are consistent with those found by Quo and coworkers and correspond to Zn^{2+}. The Sn core level spectrum (**Figure 4.9 (c)**) demonstrates the presence of a doublet Sn $3d_{5/2}$ peak at 486 eV and a doublet Sn $3d_{3/2}$ 495 eV and corresponding energy difference of 8.66 eV occur as a result of Sn^{4+} and Sn^{2+} [29], [38]. The detection of Sn^{2+} is indicative of the presence of SnO. The presence of sulfur with an oxidation number of -2 can be identified by a range of peaks with energies between 160-164 eV in the XPS high resolution spectrum of S 2p, ranging from a singlet [39] to a doublet and then a triplet [40]. **Figure 4.9 (d)** shows the presence of both sulfide and sulfate species within the prepared CZTS. The peak between 160 eV and 164 eV which can be deconvoluted to a quartet confirms the expected valence of sulfur (2-) in Cu_2ZnSnS_4. On the other hand, the doublet sulfate peak between 167 eV and 170 eV demonstrates the

availability of sulfur with a positive charge of 6 in SO_4^{2-}. Evidently from both the Sn and S core-level spectrum, some oxidation has occurred however the extent is low as no impurities were observed in the XRD [30].

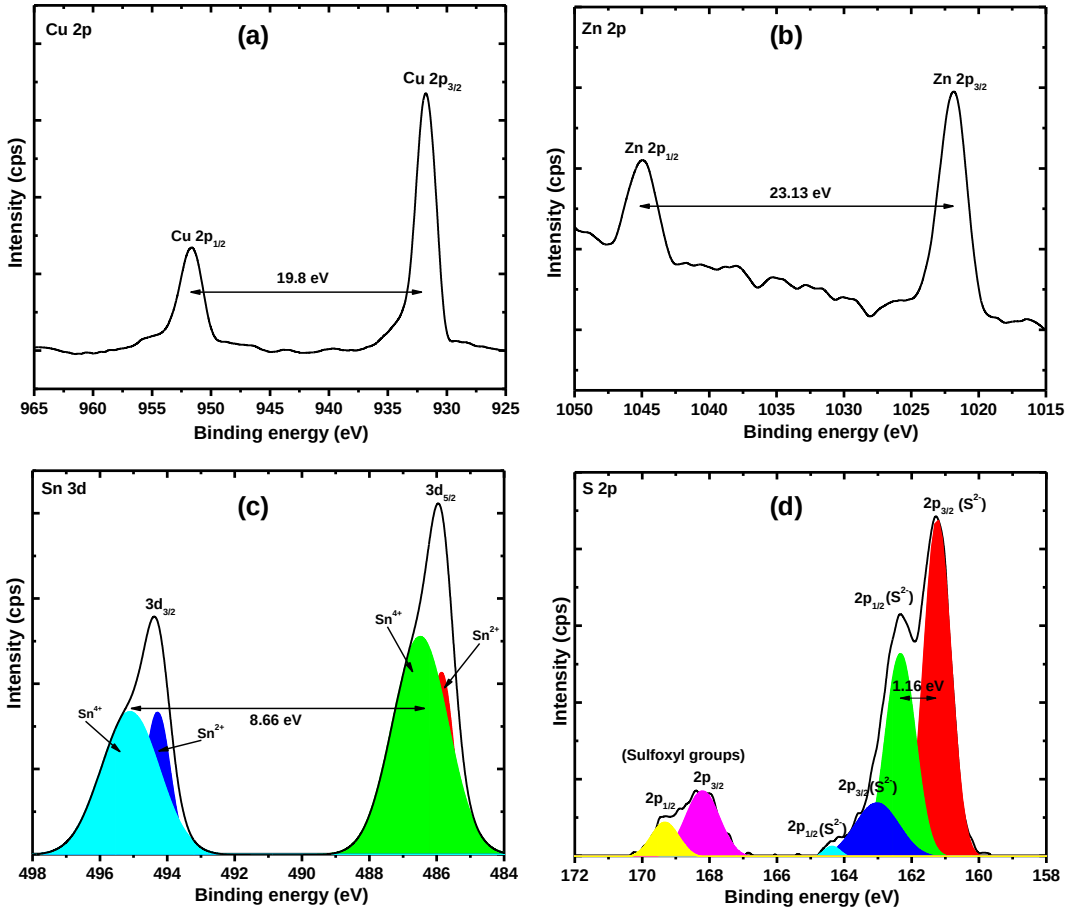


Figure 4.9: XPS high-resolution spectra of (a) copper, (b) zinc, (c) tin and (d) sulfur.

In addition to the high-resolution spectra of the constituents of CZTS, the high-resolution spectra of C 1s, O 1s and N 1s are shown in **Figure 4.10** and these shows the nature of the capping of the CZTS nanoparticles and the extent of oxidation. The C 1s spectrum shows the C-C peak at 284.3 eV attributed to the alkyl chain of the capping the capping agent. The O-C=O peak shows the oxidation of the capping agent. The O 1s spectrum has a broad peak that is centred at 531.5 eV and deconvolution of the O 1s spectrum gives rise to three peaks at 530.3 eV, 531.5 eV and 533.2 eV that are ascribed to the presence of metal oxide (MO) most likely SnO as evident in the Sn 3d spectrum, C-O and C=O respectively. The nitrogen high resolution spectrum shows one peak at 401 eV associated with the binding of OLA to the CZTS nanoparticles through the nitrogen atom.

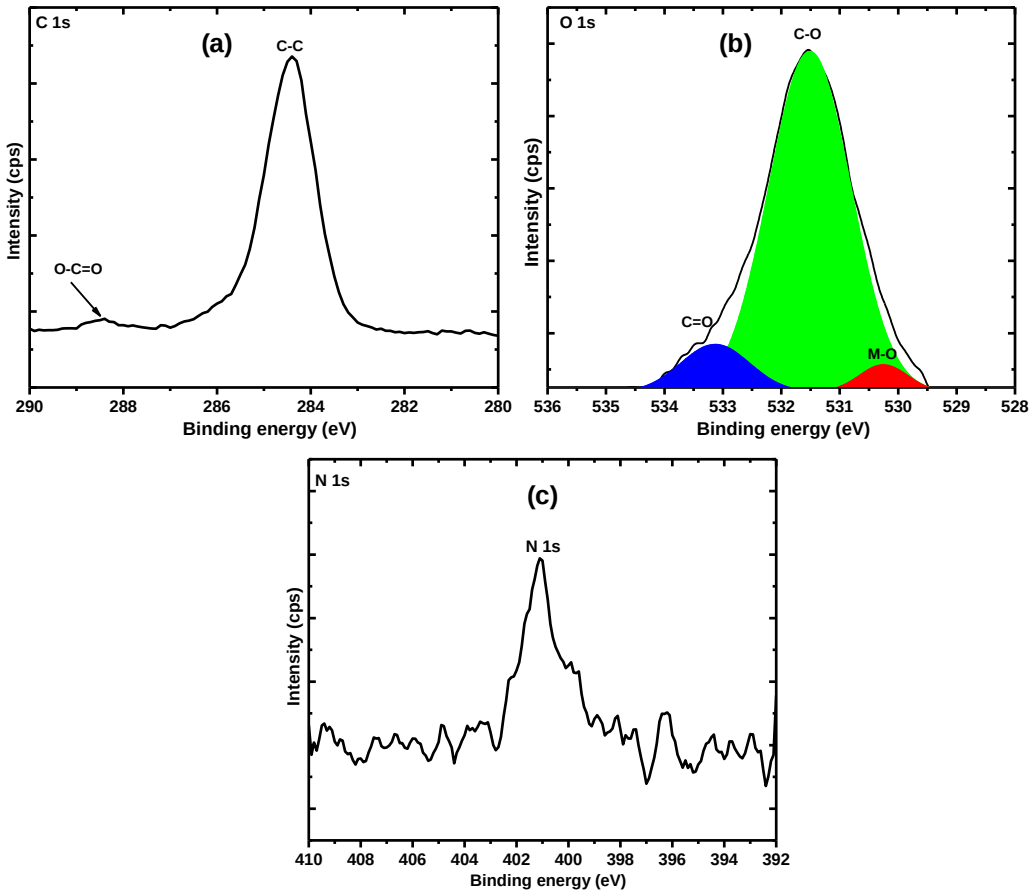


Figure 4.10: XPS high-resolution spectra of (a) carbon, (b) oxygen and (c) nitrogen.

4.3.4 Morphology evaluation of CZTS

TEM and SEM images of CZTS in **Figure 4.11** below reveal that the synthesized nanoparticles are poly-dispersed (17 ± 9 nm) with shapes ranging from circular, rectangular and triangular and agglomerated. Photovoltaic performance of nanoparticles depends on a distinct morphology, it is therefore vital to have a single shape and a narrow size distribution of the nanoparticles. This then prompted a study on digestive ripening which aims at improving the dispersity of the particles. The EDX spectrum obtained from SEM of CZTS nanoparticles is shown in **Figure 4.12**. It shows signals due to Cu, Zn, Sn and sulfur elements, which are all the elements that make up CZTS. The precise ratio of the elements was determined by high resolution XPS analysis of CZTS sample (**Figure 4.9**) and found to be 4.3:1.1:2.9:11.2 (1.5:0.4:1:3.9) which is not too far off from the expected ratio of 2:1:1:4 for Cu_2ZnSnS_4.

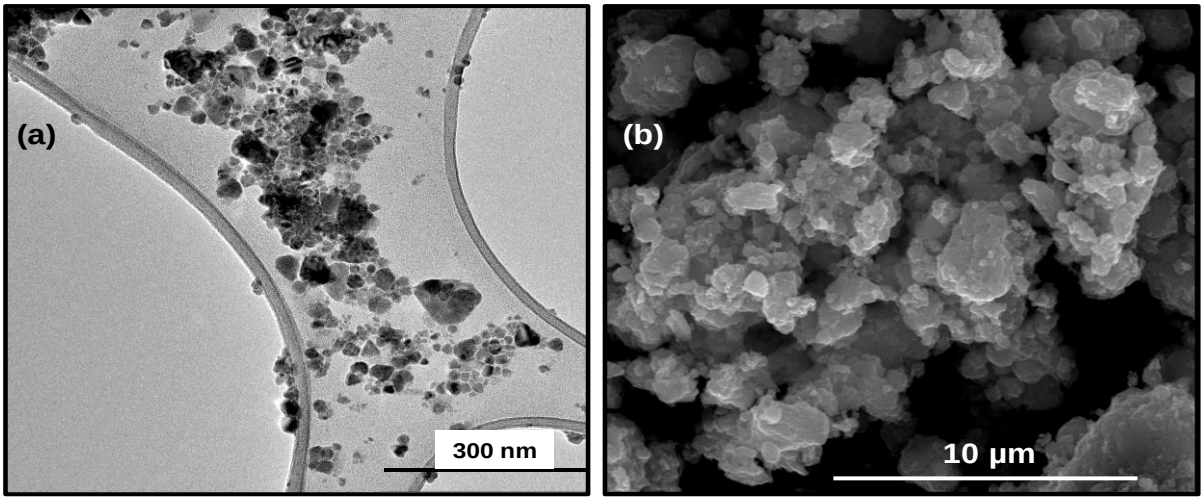


Figure 4.11: (a) TEM and (b) SEM images of the as-synthesized CZTS.

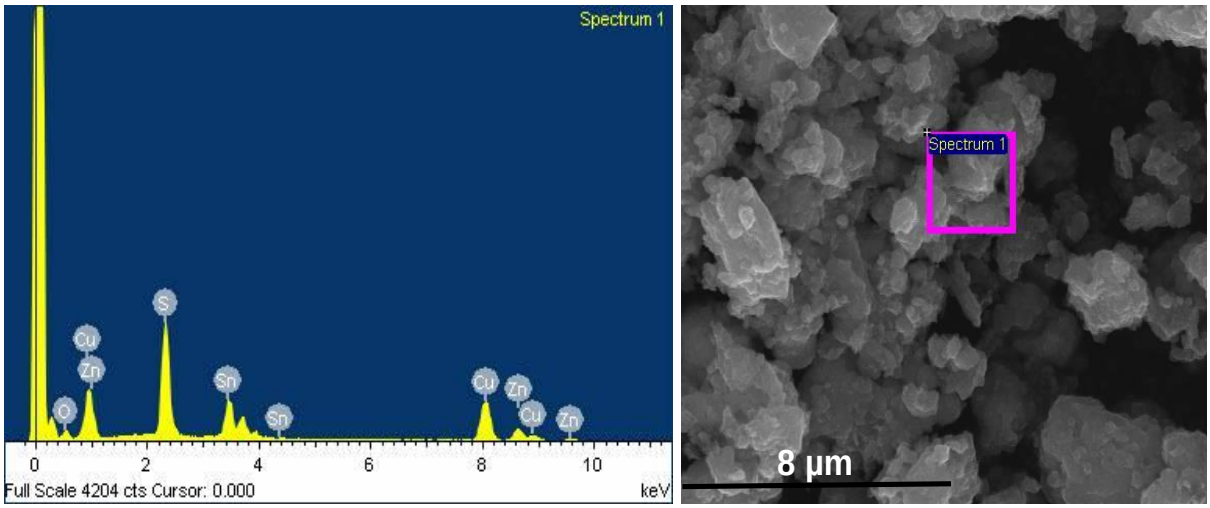


Figure 4.12: EDX spectrum and corresponding SEM image of CZTS.

4.3.5 Digestive ripening of CZTS

TEM images and corresponding size distribution curves shown in **Figure 4.13** demonstrate the change in size of CZTS nanoparticles during digestive ripening in excess OLA from 1 to 5 hours. As digestive ripening time is increased from 1 hour (16 ± 7 nm) to 2 hours (13 ± 4 nm), the particles become more spherical, smaller and monodispersed (low standard deviation). However, at 3 hours (13 ± 6 nm), triangular and circular particles exist and are poly-dispersed while at 4 hours of digestive ripening, particles are much smaller (10 ± 3 nm) and more monodispersed. At 5 hours (15 ± 4 nm), the particles become more circular but larger than at 2 hours. This observation suggests that 4 hours of refluxing the colloid in excess OLA is enough to give mono-dispersed particles. The change from mono-dispersed particles at 2 hours to highly poly-dispersed particles at 3 hours could suggest that at this point, a transition state is reached, as in 1 hour, whereby atoms start leaching out from larger

particles and deposit on much smaller ones (possibly below 10 nm), and thus resulting in reduction of size distribution. Sahu and Prasad observed that when the digestive ripening of gold nanoparticles is carried out at 60 °C and 90 °C using hexadecanethiol for 24 hours, within the first hour the size distribution becomes very narrow but as time is increased, no significant change occurs in the size of the nanoparticles occurs [11].

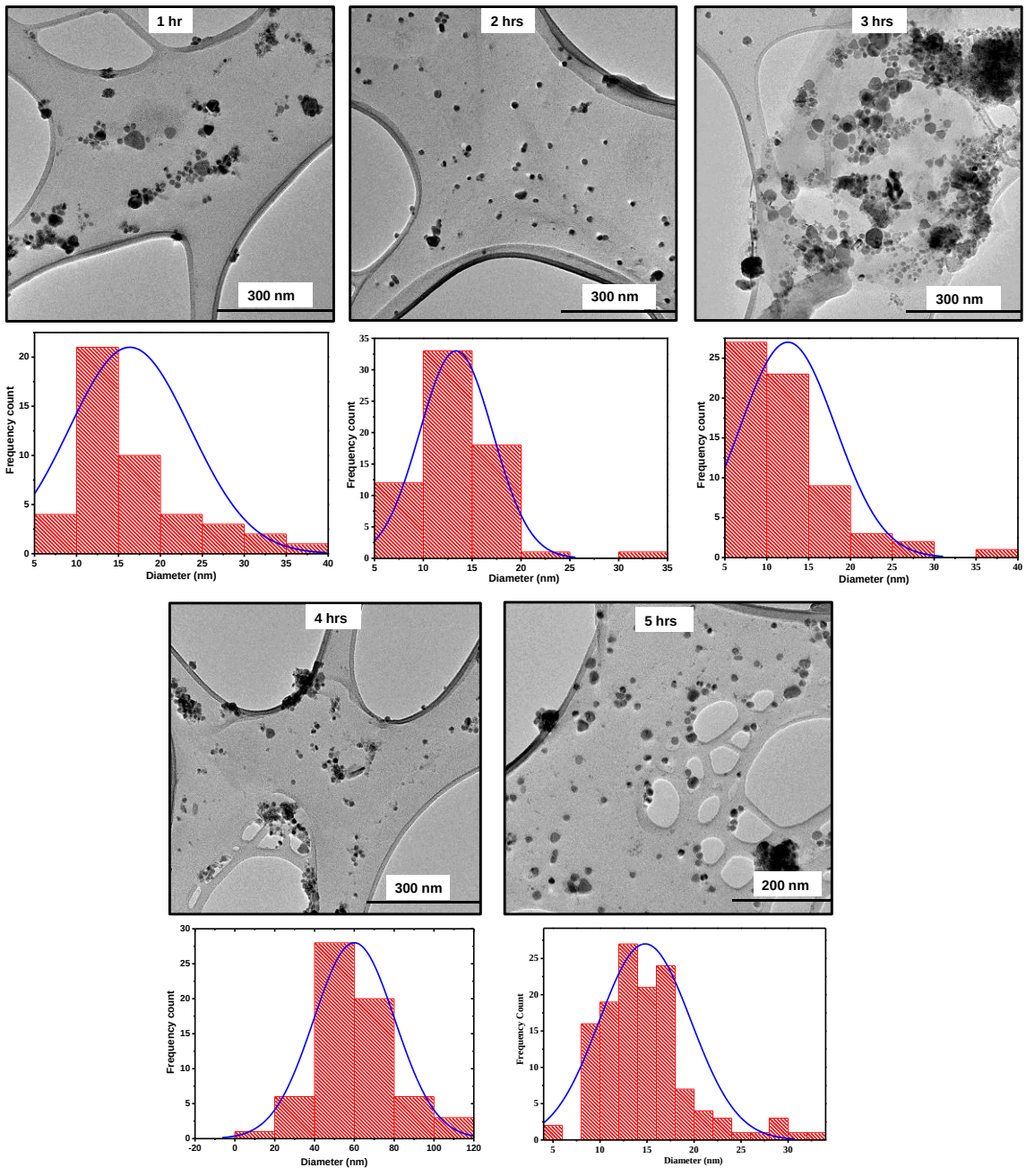


Figure 4.13: Effect of digestive ripening time on the shape and size distribution of CZTS.

4.3.6 Ligand exchange

Figure 4.14 shows the FTIR spectra of OLA capped CZTS, 3-MPA capped CZTS, EDT capped CZTS and pyridine capped CZTS. The FTIR spectra of OLA, 3-MPA and EDT capped CZTS shows peak at around 2900 cm^{-1} due to =C-H bending and stretching modes while pyridine shows a doublet at slightly higher wavenumber of 3100 cm^{-1} attributed to =C-H bond stretch. This peak appears at a higher energy in pyridine because pyridine is a cyclic compound and thus requires more energy to stretch the C-H bond. This suggests that pyridine was exchanged for OLA. For the other ligands, it is not clear from FTIR spectra whether the ligand swapping was successful or how the functional group vibrations change since the FTIR of the pure EDT and 3-MPA were not evaluated because these substances have very strong smells. Proton NMR was then used to confirm the ligand exchange process.

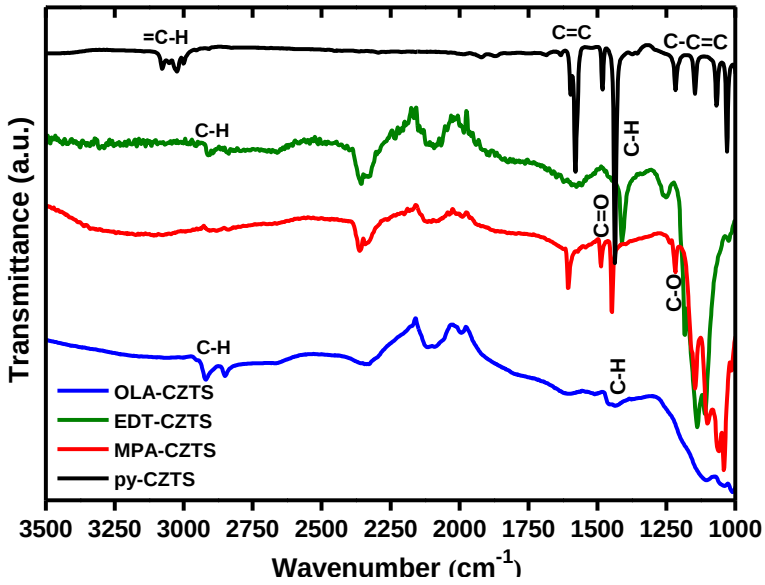


Figure 4.14: FTIR spectra of OLA capped CZTS and CZTS after ligand exchange.

^{1}H NMR spectrum of pyridine capped CZTS shows proton peaks between 7 and 9 ppm, which are also available in the spectrum of free pyridine (**Figure 4.15**). The signal of the three types of protons have downshifted and the multiplicity of the signal due to the proton α to the heteroatom has changed from a triplet to a singlet while there is no change in the multiplicity of the β-N and γ-N proton signals as seen in **Figure 4.15 (b)**. This change suggests that the nanoparticles interact with the pyridine ligand through the nitrogen. The intensity of the peaks has drastically decreased in the spectrum of the nanoparticles because the nanoparticles contain paramagnetic metal ions. In addition to this, the peaks previously seem in the ^{1}H NMR spectra of OLA and OLA capped CZTS due to protons on the alkyl chain are also observed in this spectrum (high intensity peaks between 0.1 and 2 ppm in the

full ^{1}H NMR spectrum py-CZTS (**Figure A4.1**). This indicates that not all the OLA ligands were replaced by pyridine.

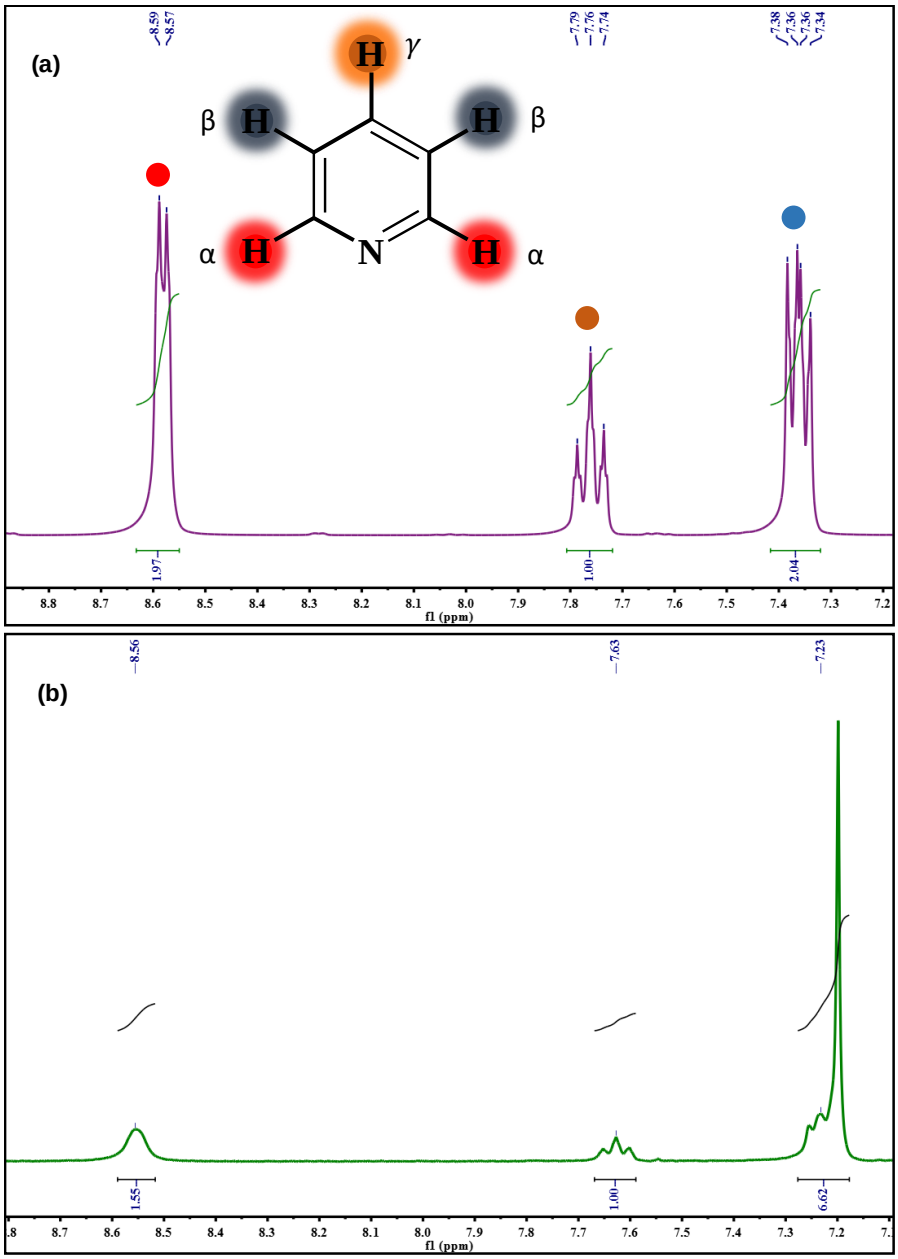


Figure 4.15: (a) ^{1}H NMR of spectra of pure pyridine and (b) corresponding pyridine capped CZTS.

The ^{1}H NMR spectra of free EDT and EDT capped CZTS is shown in **Figure 4.16**. EDT has one type of proton that has a triplet signal at around 2.75 ppm. This signal appears up field in the spectrum of the nanoparticles at 2.9 ppm and has changed from a triplet to a singlet. The protons bonded to the sulfur atoms do not show in the spectrum because sulfur is highly electronegative, it therefore has a large electron cloud covering it which shields the -SH proton from the magnetic field in NMR spectroscopy. The shifting and the broadening of the

signal suggest that the ligand has indeed coordinated to the CZTS nanoparticles. The peaks around 3.5 (#) and 2.5 (*) are due to residual water and d-DMSO, respectively.

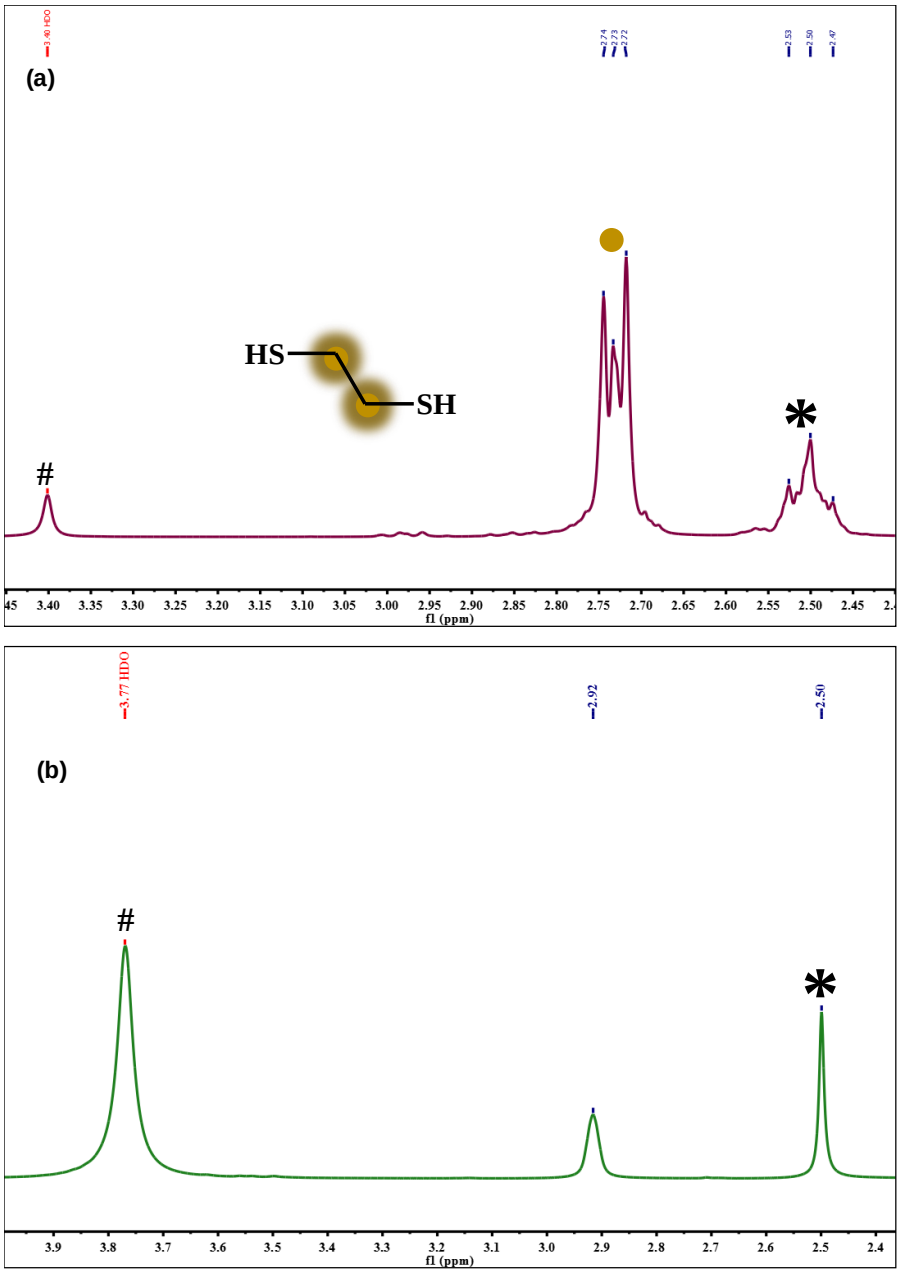


Figure 4.16: ^{1}H NMR spectra of (a) pure EDT and corresponding (b) EDT capped CZTS.

The proton NMR spectrum of free 3-MPA (**Figure 4.17 (a)**) reveals three types of hydrogens allocated to the thiol group (2.05 ppm), protons atα (2.60 ppm) and β (2.50) positions to the thiol group. On the other hand, only two proton signals at 2.54 ppm and 2.08 ppm are observed on spectrum of 3-MPA-CZTS and are assigned to the thiol proton and proton α to the thiol functional group. The disappearance of the proton signal due to protons β to the thiol

group as well as the presence of the signal due to the thiol proton after ligand exchange suggests that contrary to what was expected, the CZTS binds to MPA through the carboxylic acid functionality not the thiol head group.

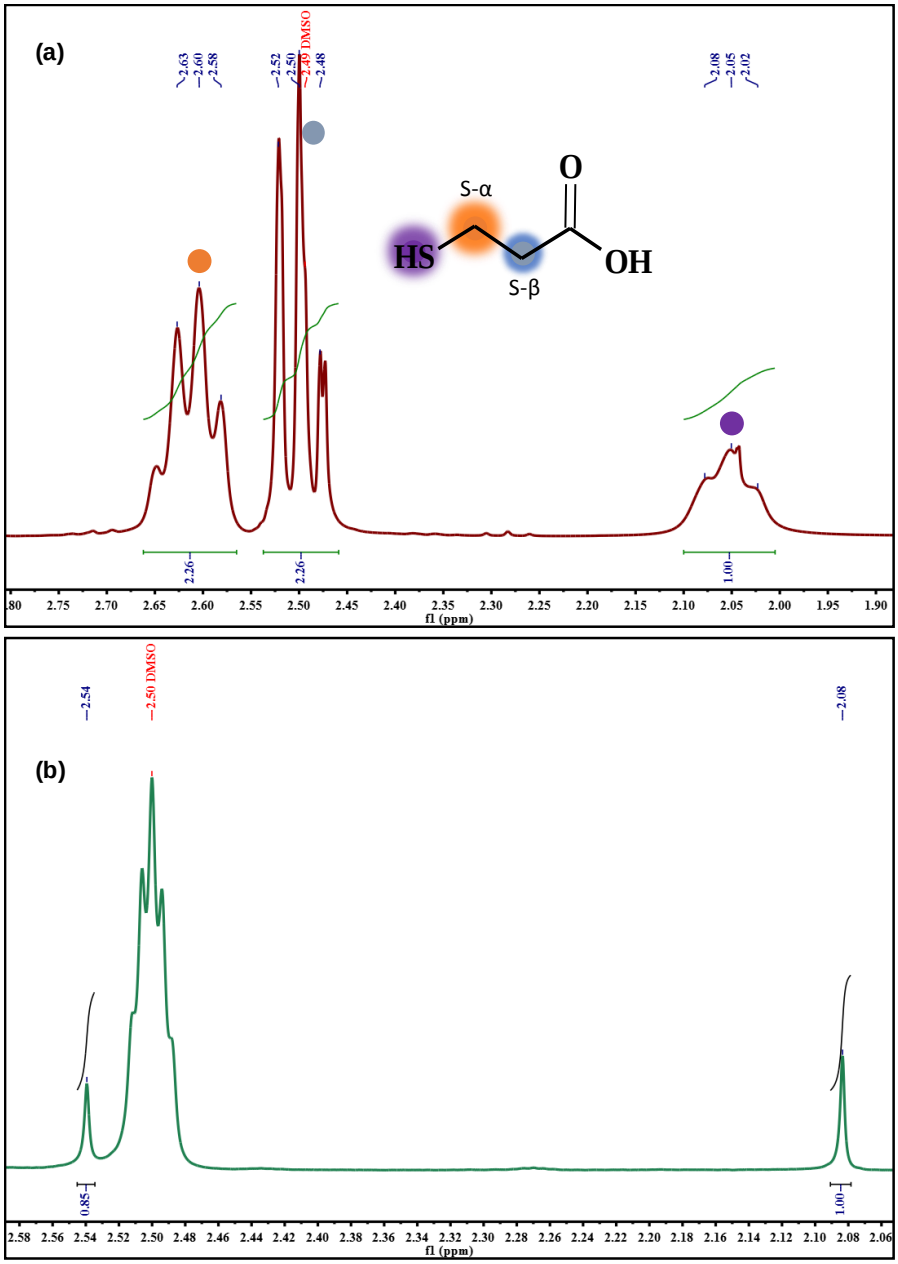


Figure 4.17: ^{1}H NMR spectra of pure MPA and MPA capped CZTS.

4.3.7 Effect of ligand exchange on the morphology and structural properties of CZTS

The impact of ligand exchange on the crystal structure of CZTS nanoparticles was evaluated by XRD, shown in **Figure 4.18** below. The XRD patterns of OLA-CZTS, MPA-CZTS, py-CZTS and EDT-CZTS nanoparticles all show three intense peaks at 2θ = 29°, 48° and 57°. These peaks were indexed to kesterite structure of CZTS (JCPDS no. 01-075-4122) and are

due to the (112), (220) and (312) crystallographic planes of CZTS. It can be noted that there is no change in the XRD spectrum CZTS nanoparticles after switching OLA ligand for MPA. This shows that exchanging OLA for MPA does not affect the structural properties of CZTS nanoparticles. However, exchanging OLA for EDT and pyridine does affect the structural properties of CZTS as more unidentified peaks are observed in the spectra of these samples.

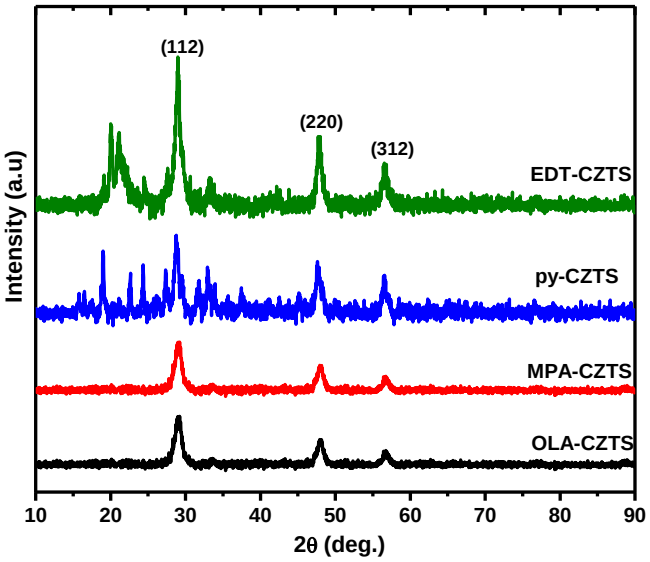


Figure 4.18: XRD patterns of CZTS nanoparticles before and after ligand exchange.

Figure 4.19 shows the effect of ligand exchange on the morphology of CZTS nanoparticles. It is evident that the CZTS nanoparticles are more agglomerated but do not lose their distinct shape when OLA is swapped for MPA ligand. This is consistent with the XRD results of the MPA-CZTS. Therefore, it can be concluded that ligand exchange from OLA to MPA does not change the crystallographic structure of CZTS, as well as its shape. The more particles are more agglomerated in the MPA-CZTS nanoparticles. This could be due to the short chain of the MPA ligand, which results in small inter-particle distance. The pyridine and EDT capped CZTS nanoparticles are also much agglomerated. In the py-CZTS TEM image, there seems to be an amorphous substance in addition to the quantum dots. This could be OLA that was exchanged for pyridine and was not removed completely upon washing, which could also explain the presence of OLA ^{1}H NMR peaks in the NMR spectrum of py-CZTS.

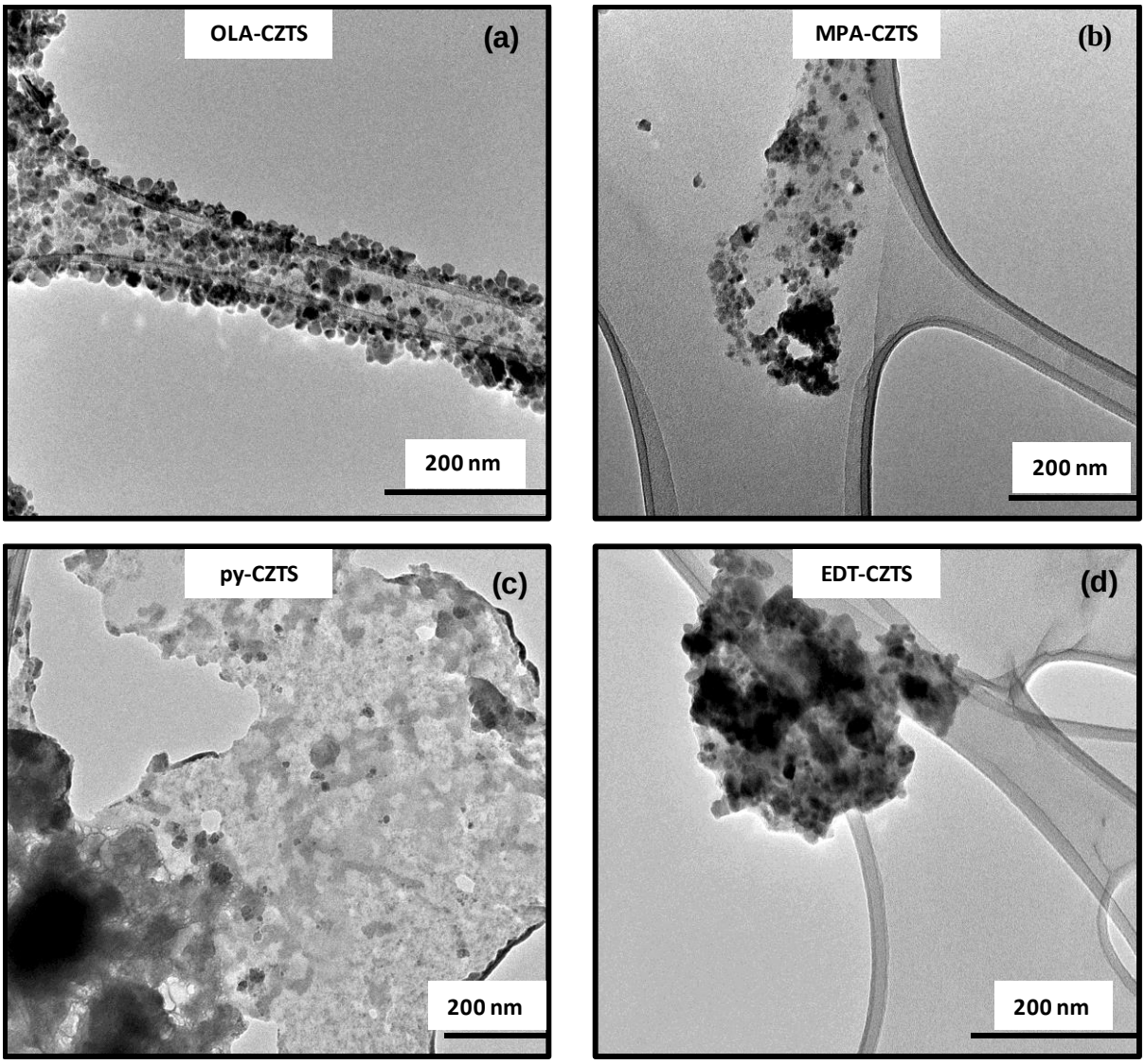


Figure 4.19: TEM images of (a) OLA-CZTS, (b) MPA-(CZTS), (c) py-CZTS and (d) EDT-CZTS.

4.4 Conclusions

Colloidal synthesis of Cu_2ZnSnS_4 nanoparticles in oleylamine at 220 °C for 45 min produced highly crystalline and poly-dispersed (17 ± 9 nm) particles that are capped by OLA through the nitrogen amine head group as confirmed by ^1H NMR spectroscopy and XPS. Surface and structural alteration of the as-synthesized Cu_2ZnSnS_4 was achieved through ligand exchange and digestive ripening respectively. Digestive ripening of CZTS at 2 and 4 hours showed the smallest particle size and lowest size distribution. Therefore, the as-synthesized poly-dispersed CZTS nanoparticles can be ripened in excess OLA for 2 hours to improve their dispersity. It was also developed that CZTS binds to pyridine, EDT and 3-MPA through interaction with nitrogen, sulfur and carboxylic acid functionalities respectively. Replacing

the OLA ligand on the CZTS with shorter chain ligands of pyridine, EDT and MPA was confirmed by ^{1}H NMR. However, the NMR of py-CZTS showed additional peaks on top of those of pyridine, therefore, this ligand only resulted in partial replacement of OLA. From the XRD and TEM results it evident that OLA capped nanoparticles were better quality than the pyridine, EDT and MPA capped CZTS.

4.5 References

[1] H. Wei, Z. Ye, M. Li, Y. Su, Z. Yang, and Y. Zhang, "Tunable band gap $Cu_2ZnSnS_{4x}Se_{4(1-x)}$ nanocrystals: Experimental and first-principles calculations," *Crystal Engineering Communications*, vol. 13, no. 7, pp. 2222-2226, 2011.

[2] M. Li, W. H. Zhou, J. Guo, Y. L. Zhou, Z. L. Hou, J. Jiao, Z. J. Zhou, J. L. Du and S. X. Wu, "Synthesis of pure metastable wurtzite CZTS nanocrystals by facile one-pot method," *Journal of Physical Chemistry C*, vol. 116, no. 50, pp. 26507-26516, 2012.

[3] T. Rath, W. Haas, P. Andreas, S. Robert, M. Eugen, K. Birgit, H. Fernidand, R. Roland andT. Gregor, "Synthesis and characterization of copper zinc tin chalcogenide nanoparticles: Influence of reactants on the chemical composition," *Solar Energy Materials and Solar Cells*, vol. 101, pp. 87-94, 2012.

[4] X. Lin, J. Kavalakkatt,K. Kornhuber, D. Abou-Ras, S. Schorr, M. C. Lux-Steiner and E. Ahmad, "Synthesis of $Cu_2Zn_xSn_ySe_{1+x+2y}$ nanocrystals with wurtzite-derived structure," *RSC Advances*, vol. 2, no. 26, pp. 9894-9898, 2012.

[5] H. Zhou, W. Hsu, H. Duan, B. Bob, and W. Yang, "CZTS nanocrystals: A promising approach for next generation thin film photovoltaics," *Energy & Environmental Science*, vol. 6, pp. 2822-2838, 2013.

[6] S. Mourdikoudis and L. M. Liz-marzan, "Oleylamine in nanoparticle synthesis," *Chemistry of Materials*, vol. 25, no.9, pp 1465-1476, 2013.

[7] U. Ghorpade, M. Suryawanshi, W. Shin, and K. Gurav, "Towards environmentally benign approaches for the synthesis of CZTSSe nanocrystals by a hot injection method : a status review," *Chemical Communications*, vol. 50, pp. 11258-11273, 2014.

[8] J. Polte, "Fundamental growth principles of colloidal metal nanoparticles-a new perspective, *"Crystal Engineering Communications,* vol. 17, no. 36, pp. 6809-6830, 2015.

[9] C. M. Evans, L. C. Cass, K. E. Knowles, D. B. Tice, R. P. H. Chang, and E. A. Weiss, "Review of the synthesis and properties of colloidal quantum dots: The evolving role of coordinating surface ligands," *Journal of Coordination Chemistry*, vol. 65, no. 13,

pp. 2391-2414, 2012.

[10] Y. Pu, F. Cai, D. Wang, J. X. Wang, and J. F. Chen, "Colloidal synthesis of semiconductor quantum dots toward large-scale production: A review," *Industrial and Engineering Chemistry Research*, vol. 57, no. 6, pp. 1790-1802, 2018.

[11] X. M. Lin, C. M. Sorensen, and K. J. Klabunde, "Digestive ripening, nanophase segregation and superlattice formation in gold nanocrystal colloids," *Journal of Nanoparticle Research*, vol. 2, no. 2, pp. 157-164, 2000.

[12] P. Sahu and B. L. V. Prasad, "Time and temperature effects on the digestive ripening of gold nanoparticles: Is there a crossover from digestive ripening to Ostwald ripening?," *Langmuir*, vol. 30, no. 34, pp. 10143-10150, 2014.

[13] B. L. V Prasad, S. I. Stoeva, C. M. Sorensen, and K. J. Klabunde, "Digestive ripening of thiolated gold nanoparticles: The effect of alkyl chain length," *Langmuir*, vol. 18, no. 20, pp. 7515-7520, 2002.

[14] P. Sahu and B. L. V. Prasad, "Effect of digestive ripening agent on nanoparticle size in the digestive ripening process," *Chemical Physics Letters*, vol. 525-526, pp. 101-104, 2012.

[15] S. I. Stoeva, V. Zaikovski, B. L. V Prasad, P. K. Stoimenov, C. M. Sorensen, and K. J. Klabunde, "Reversible transformations of gold nanoparticle morphology," *Langmuir*, vol. 21, no. 10, pp. 10280-10283, 2005.

[16] B. L. V. Prasad, S. I. Stoeva, C. M. Sorensen, and K. J. Klabunde, "Digestive-ripening agents for gold nanoparticles: Alternatives to thiols," *Chemistry of Materials*, vol. 15, no. 4, pp. 935-942, 2003.

[17] X. Zeng, D. Xiong, W. Zhang, L. Ming, Z. Xu, Z. Huang, M. Wang, W. Chen and Y. Cheng, "Spray deposition of water-soluble multiwall carbon nanotube and $Cu_2ZnSnSe_4$ nanoparticle composites as highly efficient counter electrodes in a quantum dot-sensitized solar cell system," *Nanoscale*, vol. 5, no. 15, pp. 6992-6998, 2013.

[18] C. C. Reinhart and E. Johansson, "Colloidally prepared 3−mercaptopropionic acid capped lead sulfide quantum dots," *Chemistry of Materials*, vol. 27, pp. 7313-7320, 2015.

[19] K. S. Jeong, J. Tang, H. Liu, J. Kim, A. W. Schaefer, K. Kemp, L. Levina, X. Wang, S. Hoogland, R. Debnath, L. Brzozowsk, E. H. Sargent and J. B. Asbury, "Enhanced mobility-lifetime products in PbS colloidal quantum dot photovoltaics," *ACS Nano*,

vol. 6, no. 1, pp. 89-99, 2012.

[20] J. Huang, B. Xu, C. Yuan, J. Sun, L. Sun and H. Ågren, "Improved performance of colloidal CdSe quantum dot-sensitized solar cells by hybrid passivation," *ACS Applied Materials and Interfaces*, vol. 6, no. 21, pp. 18808-18815, 2014.

[21] R. Wang, Y. Shang, P. Kanjanaboos, and W. Zhou, "Colloidal quantum dot ligand engineering for high performance solar cells," *Energy & Environmental Science*, vol. 9, pp. 26-32, 2016.

[22] J. Shi, P. Zhao, and X. Wang, "Piezoelectric-polarization-enhanced photovoltaic performance in depleted-heterojunction quantum-dot solar cells," *Advanced Materials*, vol. 25, no. 6, pp. 916-921, 2013.

[23] J. M. Luther, M. Law, Q. Song, C. L. Perkins, M. C. Beard, and A. J. Nozik, "Structural, optical, and electrical properties of self-assembled films of PbSe nanocrystals treated with 1,2-ethanedithiol.," *ACS Nano*, vol. 2, no. 2, pp. 271-80, 2008.

[24] Z. Ning, O. Voznyy, J. Pan, S. Hoogland, V. Adinolf, J. Xu, M. Li, A. R. Kirmani, J. Sun, J. Minor, K. W. Kemp, H. Dong, L. Rollny, A. Labelle, G. Carey, B. Sutherland, I. Hill, A. Amassian, H. Liu, J. Tang, O. M. Bakr and E. H. Sargent, "Air-stable n-type colloidal quantum dot solids," *Nature Materials*, vol. 13, pp. 4-10, 2014.

[25] J. B. Sambur, S. C. Riha, D. Choi, and B. A. Parkinson, "Influence of surface chemistry on the binding and electronic coupling of CdSe quantum dots to single crystal TiO_2 surfaces," *Langmuir*, vol. 26, no. 7, pp. 4839-4847, 2010.

[26] K. S. Andrikopoulos, A. G. Kalampounias, O. Falagara, and S. N. Yannopoulos, "The glassy and supercooled state of elemental sulfur: Vibrational modes, structure metastability, and polymer content," *The Journal of Chemical Physics*, vol. 139, pp.124501-1-124501-11, 2013.

[27] M. Himmrich and Haeuseler, "Far infrared studies on stannite and wurtzstannite type compounds," *Spectrochimica Acta*, vol. 47A, no. 7, pp. 933-942, 1991.

[28] B. Bai, D. Kou, W. Zhou, Z. Zhou, Q. Tian, Y. Meng and S. Wu, "Quaternary Cu_2ZnSnS_4 quantum dot-sensitized solar cells: Synthesis, passivation and ligand exchange," *Journal of Power Sources*, vol. 318, pp. 35-40, 2016.

[29] J. M. R. Tan, Y. H. Lee, S. Pedireddy, T. Baikie, X. Y. Ling, and L. H. Wong, "Understanding the synthetic pathway of a single-phase quarternary semiconductor using surface-enhanced Raman scattering: A case of wurtzite Cu_2ZnSnS_4 nanoparticles," *Journal of the American Chemical Society*, vol. 136, no. 18, pp. 6684-

6692, 2014.

[30] Z. Tong, Z. Su, F. Liu, L. Jiang, Y. Lai, J. Li and Y. Liu, "In situ prepared Cu_2ZnSnS_4 ultrathin film counter electrode in dye-sensitized solar cells," *Materials Letters*, vol. 121, pp. 241-243, 2014.

[31] P. K. Sarswat and M. L. Free, "Demonstration of a sol-gel synthesized bifacial CZTS photoelectrochemical cell," *Physica Status Solidi A*, vol. 2864, pp. 2861-2864, 2011.

[32] S. S. Nemala, K. Mokurala, P. Bhargava, and S. Mallick, "Titania nanobelts as a scattering layer with Cu_2ZnSnS_4 as a counter electrode for DSSC with improved efficiency," *Materials Today: Proceedings*, vol. 5, no. 11, pp. 23351-23357, 2018.

[33] S. S. Nemala, K. Mokurala, P. Bhargava, and S. Mallick, "Cu_2ZnSnS_4/CNT composites as Pt free counter electrodes for dye sensitized solar cells with improved efficiency," *Materials Today: Proceedings*, vol. 3, no. 6, pp. 1808-1814, 2016.

[34] R. A. Sperling and W. J. Parak, "Surface modification, functionalization and bioconjugation of colloidal Inorganic nanoparticles," *Philosophical Transactions of the Royal Society A: Mathematical, Physical and Engineering Sciences*, vol. 368, pp. 1333-1383, 2010.

[35] P. Dai, X. Shen, Z. Lin, Z. Feng, H. Xu, and J. Zhan, "Band-gap tunable $(Cu_2Sn)_{x/3}Zn_{1-x}S$ nanoparticles for solar cells," *Chemical Communications*, vol. 46, no. 31, pp. 5749-5751, 2010.

[36] C. Chory, F. Zutz, F. Witt, H. Borchert, and J. Parisi, "Synthesis and characterization of Cu_2ZnSnS_4," *Physica Status Solidi (c)*, vol. 7, no. 6, pp. 1486-1488, 2010.

[37] B. Li, Y. Xie, J. Huang, and Y. Qian, "Synthesis by a solvothermal route and characterization of $CuInSe_2$ nanowhiskers and nanoparticles," *Advanced Materials*, vol. 11, no. 17, pp. 1456-1459, 1999.

[38] C. Jin, P. Ramasamy, and J. Kim, "Facile hot-injection synthesis of stoichiometric $Cu_2ZnSnSe_4$ nanocrystals using bis(triethylsilyl) selenide," *Dalton Transactions*, vol. 43, pp. 9481-9485, 2014.

[39] S. Cingarapu, Z. Yang, C. M. Sorensen, and K. J. Klabunde, "Synthesis of CdSe/ZnS and CdTe/ZnS quantum dots: Refined digestive ripening," *Journal of Nanomaterials*, vol. 2012, pp. 1-12, 2012.

[40] M. Fantauzzi, B. Elsener, D. Atzei, A. Rigoldi, and A. Rossi, "Exploiting XPS for the identification of sulfides and polysulfides," *RSC Advances*, vol. 5, no. 93, pp. 75953-75963, 2015.

[41] A. Singh, C. Coughlan, D. J. Milliron, and K. M. Ryan, "Solution synthesis and

assembly of wurtzite-derived Cu-In-Zn-S nanorods with tunable composition and band gap," *Chemistry of Materials*, vol. 27, pp. 1517-1523, 2015.

[42] F. Liu, J. Sun, L. Zhu, X. Meng, C. Qi, and F. Xiao, "Sulfated graphene as an efficient solid catalyst for acid-catalyzed liquid," *Journal of Materials Chemistry*, vol. 22, pp. 5495-5502, 2012.

[43] A. Hassinen, I. Moreels, C. De Mello Donegá, J. C. Martins, and Z. Hens, "Nuclear magnetic resonance spectroscopy demonstrating dynamic stabilization of CdSe quantum dots by alkylamines," *Journal of Physical Chemistry Letters*, vol. 1, no. 17, pp. 2577-2581, 2010.

[44] R.K. Sithole, L.F.E. Machogo, M.A. Airo, S.S. Gqoba, M.J. Moloto, P. Shumbula, J. Van Wyk, N. Moloto, "Synthesis and characterization of Cu_3N nanoparticles using pyrrole-2-carbaldpropyliminato Cu(II) complex and $Cu(NO_3)_2$ as single-source precursors: the search for an ideal precursor, " *New Journal of Chemistry*, vol. 42, no. 4, pp. 3042-3049.

[45] L.F.E. Machogo, P. Tetyana, R. Sithole, S.S. Gqoba, N. Phao, M. Airo, P.M. Shumbula, M.J. Moloto, N. Moloto, "Unravelling the structural properties of mixed-valence α- and β-AuSe nanostructures using XRD, TEM and XPS," *Applied Surface Science*, vol. 456, pp. 973-979, 2019.

Chapter 5 : Preparation of Cu_2ZnSnS_4/fN-MWCNTs nanocomposites and their electrochemical properties

5.1 Introduction

5.1.1 Hybrid materials

Reducing the size of materials to nanoscale levels has improved their efficiency, surface area sensitivity as well as response time in various industrial applications. However, no one material possesses all the required properties for a specific application without showing any shortcomings. Combining materials can counteract the shortcomings of one material by another material, or rather completely distinct properties can be obtained through material combinations [1]. These systems are referred to as hybrid materials and can either be categorized based on the strength of interaction between the individual components (classes), or by the number of phases observed in the hybrid material [2]. Class I hybrid materials embody a physical mode of interaction between the constituent phases (van deer Waals forces of attraction, hydrogen bonding and electrostatic interaction) while in class II hybrids, a chemical bond as a result of a chemical reaction between the functional groups of the elements exists [3], [4]. Alternatively, the phase composition of the hybrid can be utilized to classify them as nanocomposites, metal-organic frameworks and carbon nanotube-inorganic hybrids. Nanocomposite materials possess at least one inorganic phase scattered in or over an organic phase. The nanocomposite properties are an accumulation of the individual properties of the constituent elements. On the other hand, metal-organic frameworks comprise of one phase made from an inorganic and organic system and their properties are distinctive from those of their constituent materials [2]. Carbon nanotube-inorganic hybrids are nanocomposites that substitute the organic phase in the nanocomposite with purely CNTs. The high aspect ratio, high surface area and mechanical stability, good electron transport and optical properties have subjected CNTs as excellent hybrid material [2]. Various CNT-inorganic hybrids have been prepared and exploited in photovoltaics [5], [6] and energy storage [7] devices, catalysis and in antimicrobial activities [8].

Generally, inorganic nanoparticles are spread on the wall surface of the nanotubes and this can be achieved by either in-situ or ex-situ preparation methods. In ex-situ synthesis, the nanoparticles are prepared and then added to the CNTs by techniques such as sonication, milling or stirring, whereas in in-situ synthesis, the CNT walls act as nucleation sites for the growth of the nanoparticles. Ex-situ synthesis offers the advantage of size and shape control

of the nanoparticles by altering reaction conditions and for colloidally prepared nanoparticles, an organic ligand covers the surface of the nanoparticles. A physical or chemical reaction between the nanoparticle ligand and the functional groups on the surface of the CNTs is then utilized in the hybrid formation. Raman spectroscopy analysis of the CNTs and the CNTs-inorganic hybrid is often used to determine the type of interaction that exists in the nanocomposite material. CNT-chalcogenide hybrid systems have been employed as counter electrodes in dye-sensitized solar cells and the increased surface area and electron conductivity due to CNTs improved the catalytic activity of the CE towards the electrolyte. The performance of a material as an efficient alternative CE to Pt is evaluated by cyclic voltammetry studies carried out in a DSSC electrolyte.

5.1.2 Cyclic voltammetry

Cyclic voltammetry (CV) is an electrochemical measurement technique that comprises of three electrodes; the working electrode (WE), counter electrode (CE) and a reference electrode (RE) all dipped in an electrolyte. Potential is applied on the working electrode in a specific direction, switched at any potential and the direction of the potential reversed, all while measuring the amount of current released. The current produced is subject to diffusion rate of the analyte in the electrolyte to the electrode surface as well as the oxidation-reduction reaction. CV is used to study oxidation-reduction reactions and a peak is observed when enough potential is applied for electron transfer. Reduction occurs when the potential energy of the electrons in the electrode is higher than the potential energy of the empty orbital of the analyte. Generally, when a potential in the positive direction is applied to the modified glassy carbon electrode, the reduced half of the I^- ions diffuse to the electrode surface where they get oxidized to I_3^-. When the direction of the potential is changed, the oxidized species are reduced back to I^-. The potential energy corresponding to the highest current measured for this reduction process relates to the amount of minimum energy required to drive the reduction reaction whereas the magnitude of the reduction peak relates to the electro-catalytic properties of the working electrode [9]. In hindsight, this generally informs the performance of the CE material when employed in DSSCs.

Platinum is a state-of-the-art DSSC counter electrode material that has shown exceptional reduction activity and a low overpotential for the reduction reaction of $I_3^-$to occur.Pt is a rare and noble metal and is oxidized in I^-/I_3^- electrolyte upon extended exposure to form PtI_4

[10]. The reduction activity of the best performing CZTS/N-MWCNTs nanocomposite material was evaluated by cyclic voltammetry and compared with Pt. During the measurement, after a voltage is applied (-1.2 – 1.2 V), I_3^- ions migrate to the surface of the working electrode were they receive electrons from it to produce $3I^-$ions until such a point where a depletion zone is created near the electrode, causing the current measured to reach a maxima and thereafter decrease [11]. Vital information can be deduced from the CV spectrum. The cathodic peak(s) correspond to the two-electron reduction of triiodide (**Equation 5.6**) while the anodic peak(s) occur due to oxidation of iodide ion (**Equation 5.7**) [12]. Of utmost importance is the reduction peak at the more negative potential. The current density magnitude (J_m) and area of this peak indicates electro-catalytic activity and adsorption sites of the CE material respectively [13]. Another important parameter from the CV spectrum is open circuit voltage (V_{oc}) which indicates the ease or the amount of energy required for the reduction reaction to occur [14].

$$\mathbf{I_3^- + 2e^- \rightarrow 3I^-}$$ **----------Equation 5.1**

$$\mathbf{I_3^- \rightarrow 3I^- + 2e^-}$$ **----------Equation 5.2**

5.2 Materials and methods

5.2.1 Chemicals

The following chemicals were used as received from the supplier: Acetonitrile (C2H3N, ≥ 99.9%), lithium iodide (LiI, 99.9%), lithium perchlorate (LiClO4, ≥ 95.0%), nafion (C7HF13O5S.C2F4, 5 wt%), iodine (I2, ≥ 99%) N, N-dimethyl formamide (DMF) (C3H7NO, > 99.5%), 1-methyl-2-pyrrolidinone (NMP) (C5H9NO, 99.5%), dimethyl sulfoxide (DMSO) (C6H6OS, 99.5%).

5.2.2 Preparation of Cu_2ZnSnS_4/fN-MWCNTs nanocomposites

A sonication procedure in DMF for nanocomposite preparation was adapted from Das and co-workers` article on CZTS and fMWCNTs hybrid synthesis [15], [16]. The CZTS samples obtained after 2 hours of digestive ripening (**Chapter 4**) and functionalized N-MWCNTs denoted fN-MWCNTs, were used for the preparation of nanocomposites. In a typical reaction, CZTS/fN-MWCNTs (15 w %) (denoted as CZTS/N-MWCNTs (0.15)) was prepared by from 85 mg of CZTS and 15 mg of fN-MWCNTs. The composite precursors were each sonicated in 4 mL of DMF at 40 °C for 1 hour. The composite precursor solutions were then mixed and sonicated further for 1 hour at the same temperature. Thereafter, the

composite material was isolated by centrifuging for three cycles while washing with ethanol, air dried and ground to a fine powder. Composite materials with 20, 25 and 30 weight % of fN-MWCNTs (denoted as CZTS/N-MWCNTs (0.2), CZTS/N-MWCNTs (0.25) and CZTS/N-MWCNTs (0.3), respectively) in CZTS/fN-MWCNTs were prepared in a similar manner. Calculation for CZTS/fN-MWCNTs (0.15) is shown below.

For CZTS/fN-MWCNTs (0.15):

⇒ CZTS: fN-MWCNTs

0.85: 0.15

Therefore, for 100 mg total mass (CZTS + fN-MWCNTs):

CZTS (mg) = 0.85 * 100 mg = 85 mg ----------Equation 5.3

CZTS weight % = $\frac{85}{100} * 100$ **% = 85 % ----------Equation 5.4**

fN-MWCNTs (mg) = 0.15 * 100 mg = 15 mg----------Equation 5.5

fN-MWCNTs w/w % = $\frac{15}{100} * 100$ **% = 15 %----------Equation 5.6**

5.2.3 Counter electrode fabrication

To prepare the ink for CE fabrication, firstly, the dissolving solution was prepared by mixing 1 mL of nafion with 2 mL of DMSO, and then 1 mL of this solution was mixed with 1 mL of NMP. Thereafter, 20 mg of the composite samples were added to 0.25 mL of the prepared solution and sonicated at 40 ºC for 1 hour. The resulting ink was drop casted on a glassy carbon electrode as illustrated in **Figure 5.1 (a)** and dried in an oven at 80 °C.

5.2.4 Electrochemical measurements

The I^-/I_3^- electrolyte was prepared by adding 0.27 g of LiI (0.01 M), 0.1 g of I_2 (0.001 M) and 2.1 g of $LiClO_4$ (0.1 M) to 40 mL of acetonitrile and the mixture was stirred until all the salts were dissolved. The redox reaction of the modified glassy carbon electrode was studied in the electrolyte using cyclic voltammetry, a three-electrode half-cell illustrated in **Figure 5.1 (b)**. In cyclic voltammetry, a potential of -1.2 to 1.6 V was applied to the working and reference electrodes and current response between the working and counter electrode recorded at increasing scan rates of 25, 50, 75 and 100 mV/s. The stability of the working electrode in the electrolyte was evaluated by running 60 scans at the maximum scan rate of 100 mV/s.

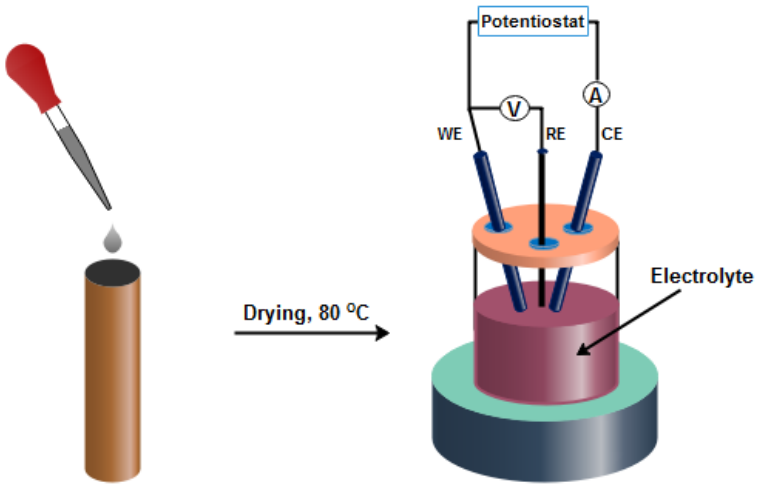


Figure 5.1: (a) Electrode fabrication by drop casting and (b) electrochemical measurement set up.

5.2.5 Characterization

The crystallographic parameters of CZTS and the presence of carbon nanotubes in the CZTS sample matrix were determined by Bruker D2 Phaser Powder X-ray diffractometer using Cu Kα light source with 2-theta scan from 5- 90°. The extent of interaction between the CZTS nanoparticles and fN-MWCNTs was evaluated by TEM, Raman spectroscopy and XPS performed on FEI Technai T12 TEM, John-Yvon T64000 micron Raman spectrophotometer and Thermo Scientific ESCAlab 250Xi, respectively. Electrochemical measurements for the prepared composites were carried out by cyclic voltammetry on BASi epsilon E2 (1231) potentiostat at scan rates ranging from 25 mV/s to 100 mV/s. The glassy carbon electrode was first cleaned by scrubbing it against alumina paste, followed by rinsing with distilled water. The composite ink deposited on glassy carbon was used as the working electrode (WE), Pt wire was used as a counter electrode (CE) and Ag/Ag^{+} ion electrode as reference electrode (RE) while I^{-}/I_3^{-} in acetonitrile was employed as an electrolyte.

5.3 Results and discussion

5.3.1 Structural, morphology and elemental composition of nanocomposites

The XRD patterns of the prepared CZTS/fN-MWCNTs nanocomposites (**Figure 5.2**) shows 3 intense peaks at 2θ = 29°, 48° and 57° and two low intensity peaks at 2θ = 27° (*) and 33° (#). The major peaks were indexed to kesterite structure of CZTS (JCPDS no. 01-075-4122) in **Figure 4.4** (**Chapter 4**) while the one at 27° is due to fN-MWCNTs. The intensity of the carbon peak in the XRD patterns of the nanocomposites does not follow any trend as the

amount of carbon nanotubes in the composite material is increased from 15% to 30%. This could be attributed to the uneven distribution of the tubes in the CZTS matrix within the CZTS/fN-MWCNTs composites. A very low intensity peak also appears at 33° (#) in the XRD spectra of the composites. As already seen from the XRD pattern of functionalized fN-MWCNTs (**Figure 3.6**), this peak appears because of residual catalyst employed in the preparation of the doped nanotubes.

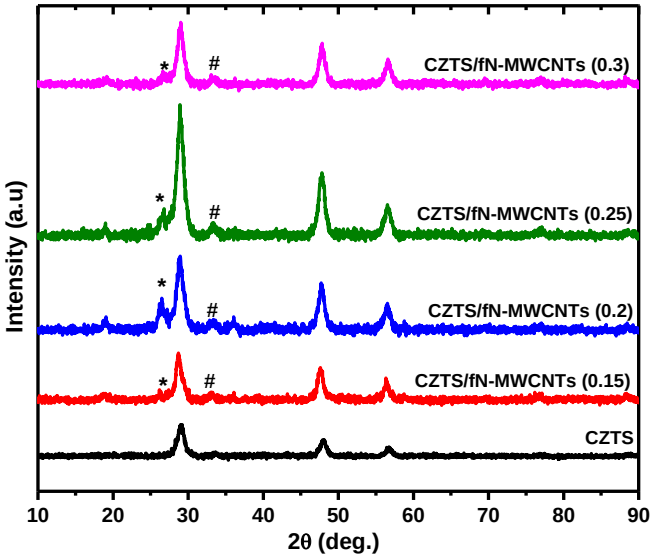


Figure 5.2: X-ray diffraction patterns of CZTS and CZTS/fN-MWCNTs with increasing fN-MWCNT concentration.

TEM images of the prepared nanocomposites are shown in **Figure 5.3** below. It can be observed that the carbon nanotubes have open ends, are entangled and have a wide diameter size distribution of 41 ± 15 nm. The CZTS nanoparticles are spherical, poly-dispersed, agglomerated and scattered unevenly on the surface of the carbon nanotubes. Additionally, the presence of bamboo compartments clearly observed in the structure of the nanotubes implies the incorporation of nitrogen within the graphene layers of the nanotubes [17], [18]. No significant change in dispersity of the CZTS nanoparticles is observed as the amount of fN-MWCNTs was increased. The TEM images do not indicate clearly, whether there is an interaction, be it physical or chemical between the CZTS nanoparticles and the fN-MWCNTs. To develop whether any interaction exists between the two composite constituent materials, Raman spectroscopy analysis was carried out.

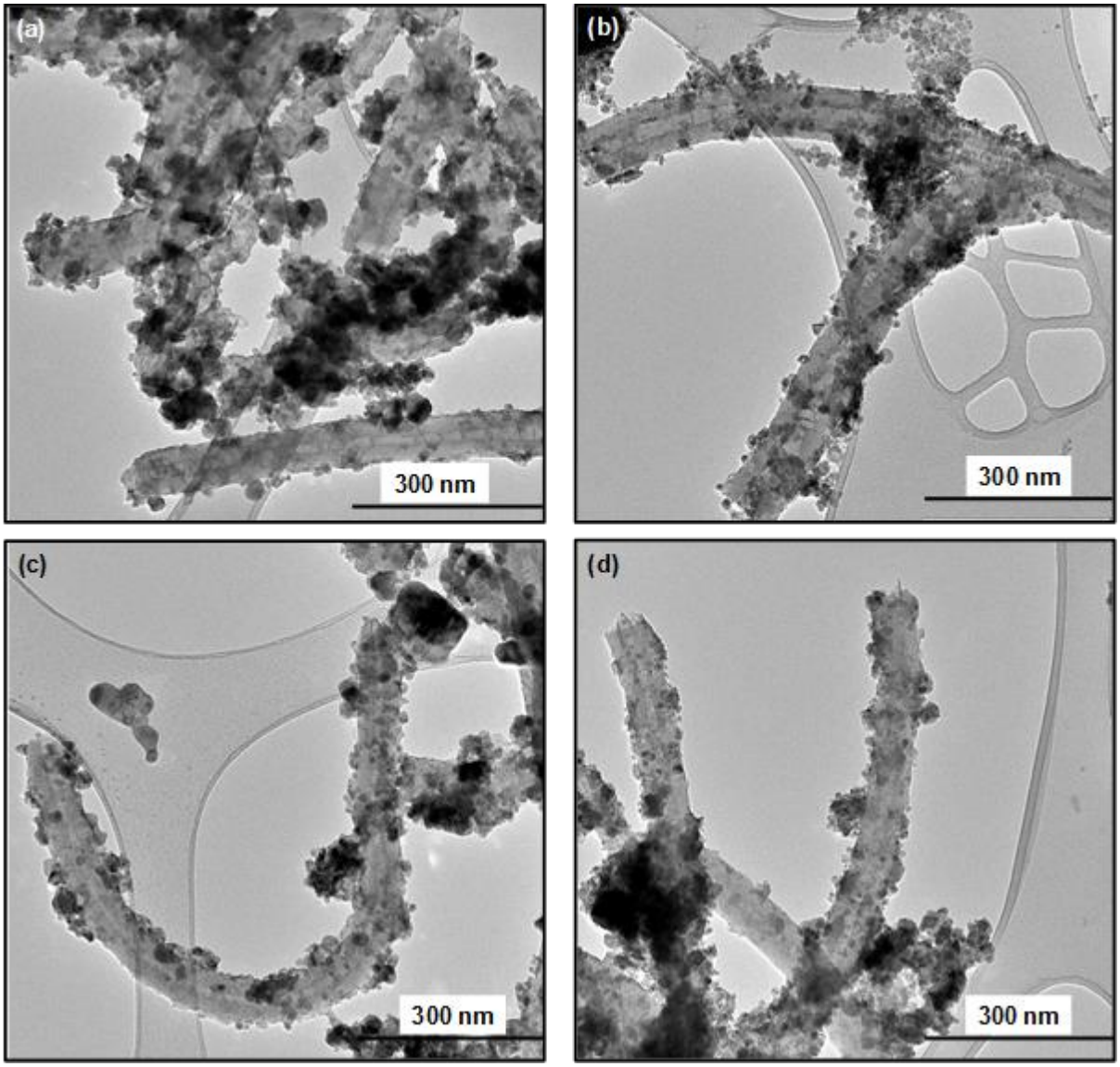


Figure 5.3: TEM micrographs of CZTS/fN-MWCNTs with increasing carbon nanotube mass ratio of (a) 0.15, (b) 0.2 (c) 0.25 and (d) 0.3.

Raman spectra of the prepared CZTS, fN-MWCNTs and CZTS/fN-MWCNTs are shown in **Figure 5.4**. The spectrum of CZTS shows two main peaks at 316 cm^{-1} and 1573 cm^{-1} attributed to kesterite CZTS and OLA ligand attached to the CZTS nanoparticles (**Chapter 4**). The CZTS peak at 316 cm^{-1} occurs because of the sulfur vibrations in the crystal structure of CZTS [19] whereas the other peaks (1402 cm^{-1} and 1573 cm^{-1}) are due to OLA, which is the capping agent employed in the synthesis of CZTS. Relative to the Raman spectrum of the CZTS/fN-MWCNTs the CZTS peak appears at higher wavenumber of 327 cm^{-1} which serves as confirmation that an interaction between the nanoparticles and carbon nanotubes exists causing the energy of sulfur vibration to increase.

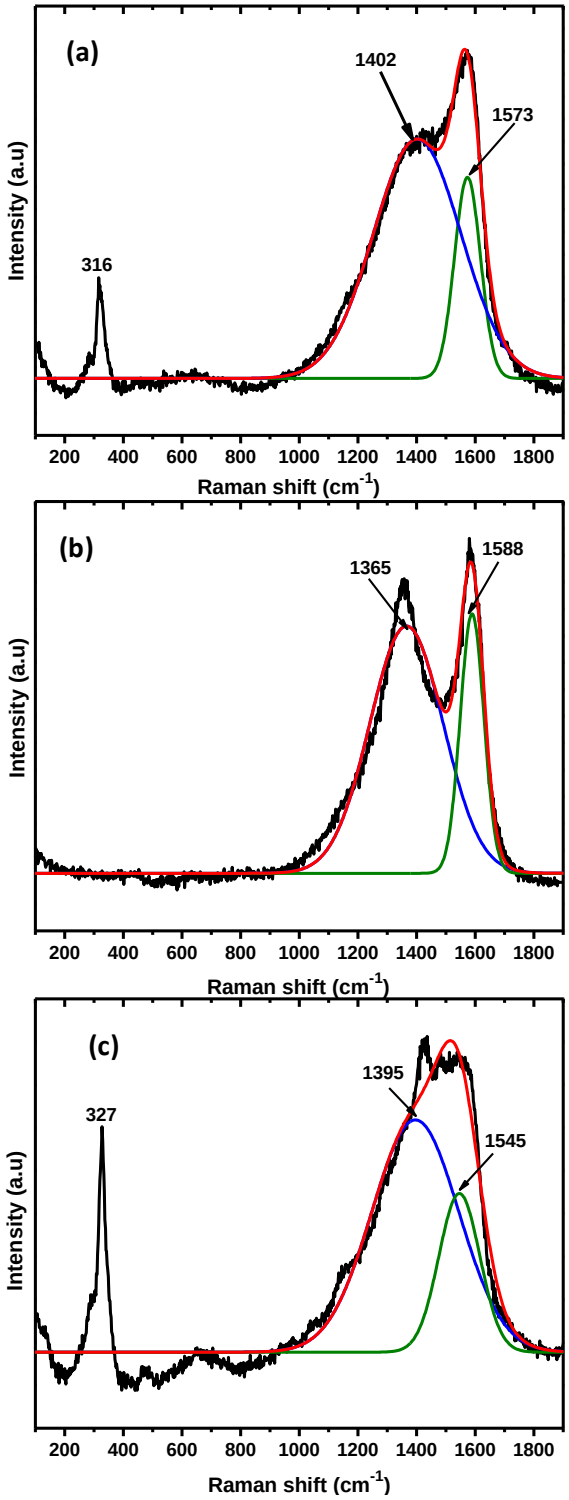


Figure 5.4: Raman spectra of as synthesized (a) CZTS, (b) fN-MWCNTs and (c) CZTS/fN-MWCNTs (0.15) nanocomposite.

The Raman spectrum of fN-MWCNTs has two high intensity peaks at 1365 cm^{-1} (D-band) due to graphene sheet flaws in a carbon structure while the peak that occurs around 1588 cm^{-1} (G-band) is from the carbon-carbon bond stretches. The shift in the G-band peak position or

the peak width change can assist in developing whether the CZTS nanoparticles interact with the walls of the carbon nanotubes in the N-MWCNTs [20]. The shift in the G-band peak to lower wavenumber of 1545 cm^{-1} in the composite material suggests that the energy of vibration of the carbon-carbon bond has decreased due to the interaction of the nanotube walls with the CZTS nanoparticles [21]. The importance of determining whether a nanocomposite is indeed formed arises from the fact that the aim of this study is to combine the catalytic properties of CZTS and the high electron conductivity of fN-MWCNTs, which can only be achieved if a nanocomposite is formed.

To further evaluate the presence of both CZTS and fN-MWCNTs in the prepared composites, XPS analysis of the samples was carried out. **Figure 5.5** and **Figure 5.6** show the XPS survey spectrum of CZTS/fN-MWCNTs (0.15) and the high-resolution spectra of copper, zinc, tin and sulfur, respectively. All atoms present in the constituent materials of the composite are present in the XPS survey scan and this provides concrete evidence of the success of hybrid formation. The Cu, Zn, Sn, and sulfur atoms are from the CZTS while both the carbon and nitrogen are present in both CZTS and fN-MWCNTs samples. fN-MWCNTs consist of a rolled-up graphene sheets with sp^2 hybridised carbons and nitrogen atoms as evidenced by the bamboo structure observed in the TEM images of the nanotubes (**Chapter 3**). CZTS on the other hand, is stabilized by an organic ligand it was synthesised in, oleylamine which binds to the CZTS core through the nitrogen head group as evidenced by proton NMR of both the pure oleylamine and OLA capped CZTS. These organic structures are both responsible for the carbon detected in the XPS survey spectrum of the composite.

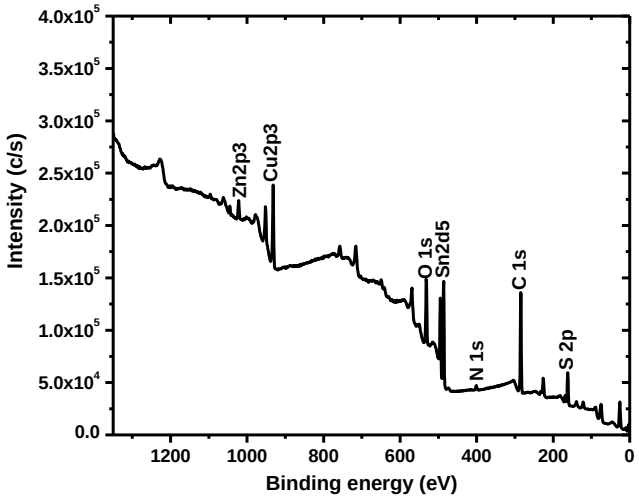


Figure 5.5: XPS survey spectrum of CZTS/fN-MWCNTs (0.15).

The atomic percentage of nitrogen in CZTS and N-MWCNTs was found to be 2.0 % and 3.6 %, respectively whereas the atomic percentage of nitrogen in CZTS/N-MWCNTs (0.15) was found to be 1.4 %. This shows a decline in the nitrogen content from 3.6 % in carbon nanotubes and 2.0 % in CZTS. Also, the nitrogen high resolution spectrum of N-MWCNTs (**Chapter 3**) could be deconvoluted to three peaks due to molecular, quaternary and pyridinic nitrogen. These nitrogen environments could not be detected in the nitrogen high resolution spectrum of the nanocomposite (**Figure 5.7**). It is possible that the CZTS nanoparticles interact with the nanotubes through the nitrogen atoms. As such, the decline in atomic percentage of nitrogen in the nanocomposites could be due to the inaccessibility of the nitrogen atoms since XPS is a surface analysis [22]. The C 1s and O1s also suggest surface oxidation of the nanocomposites.

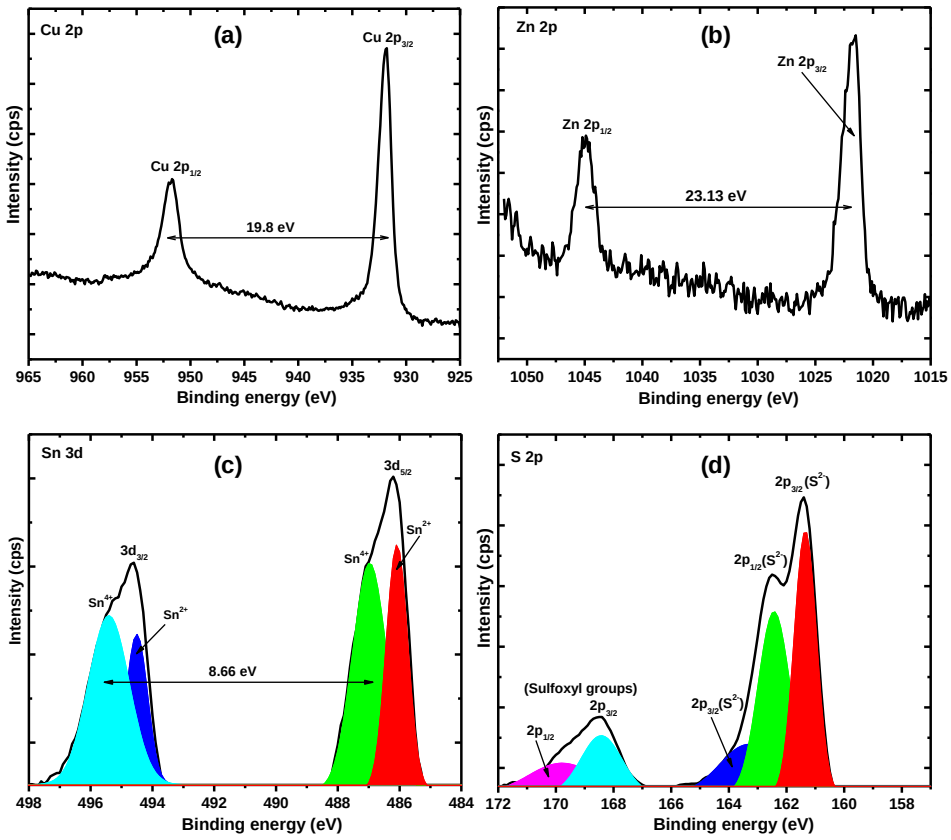


Figure 5.6: XPS high-resolution spectra of (a) copper, (b) zinc, (c) tin and (d) sulfur.

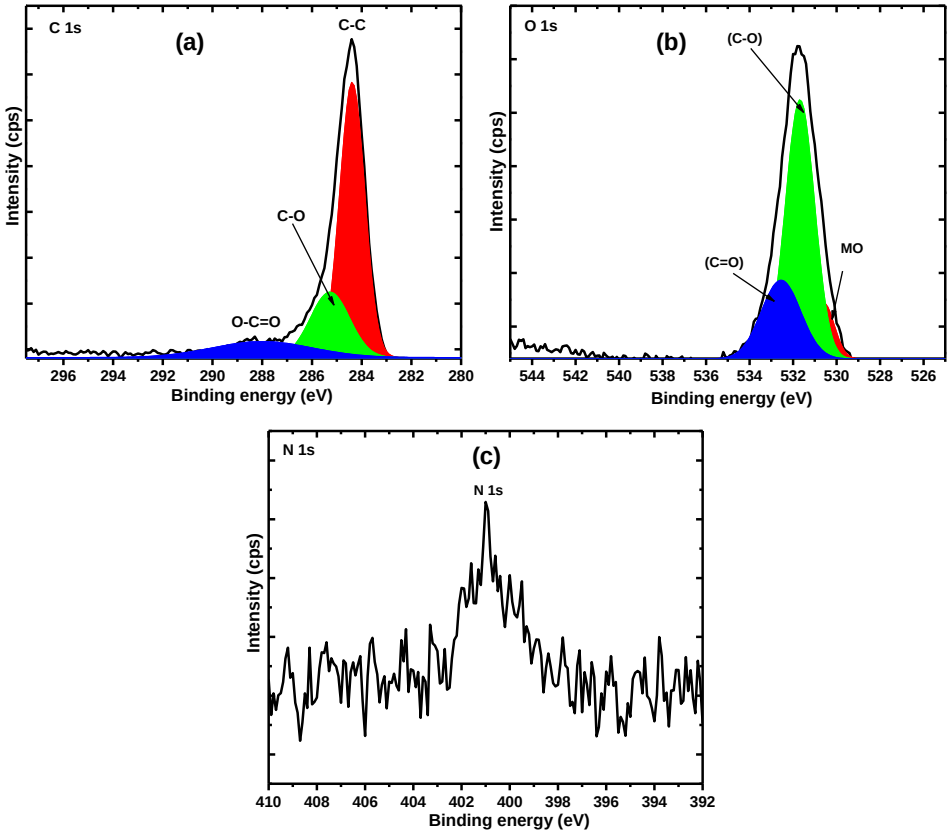


Figure 5.7: XPS high-resolution spectra of (a) carbon, (b) oxygen and (c) nitrogen.

5.3.2 Proposed mechanism for interaction of fN-MWCNTs and CZTS

It was developed in **Chapter 3** that carboxylic acid functional groups and quaternary as well as pyridinic nitrogen atoms are present on the walls and within the graphitic network of the carbon nanotubes. These induced functionalities and defects were assumed to be the reaction sites for the chemical interaction between the nanotubes and the CZTS nanoparticles. From **Chapter 4**, it was concluded that CZTS nanoparticles are stabilized by OLA and the nitrogen head group binds directly to the nanoparticles. Therefore, the alkene and alkane groups on the tail of OLA can be utilized as reaction sites on CZTS. As has been mentioned, the both the CZTS and N-MWCNTs were sonicated in DMF at 50 °C for 1 hour before mixing the solutions to prepare the nanocomposites. DMF is reported to facilitate reactions that undergo polar mechanisms. It is assumed that, on mixing CZTS and N-MWCNTs solutions, the hydroxyl group on the carboxylic acid group undergoes nucleophilic attack by the alkene group on the OLA, followed by addition of the hydroxyl oxygen to the now positively charged carbon of the alkene group. This follows an S_N2 reaction mechanism and is depicted in **Equation 5.5** below. Alternatively, it can be assumed that a physical electrostatic

interaction exists between the positively charged sites on the quaternary nitrogen atoms on the walls of the nanotubes and the slightly negative site of the alkene functional group.

$$\mathbf{R-COOH+R=R \rightarrow R-COO-C-R_2H}$$ **----------Equation 5.7**

Where **R** represents the carbon backbone of the nanotubes.

5.3.3 Electrochemical properties of CE materials

Cyclic voltammetry of platinum electrode (area = $1.767 \times 10^{-2}\ cm^{-2}$) at increasing scan rates is shown in **Figure 5.8**. Current density and therefore electro-catalytic activity are elevated when scan rate is increased since more current is produced within a short time. Scan rate gives an indication of the reversibility of the reaction of the redox couple at the electrode surface. For reversible reactions, peak current intensity is proportional to the square root of the scan rate [11]. As such, the I^-/I_3^- redox reaction on the Pt electrode is reversible.

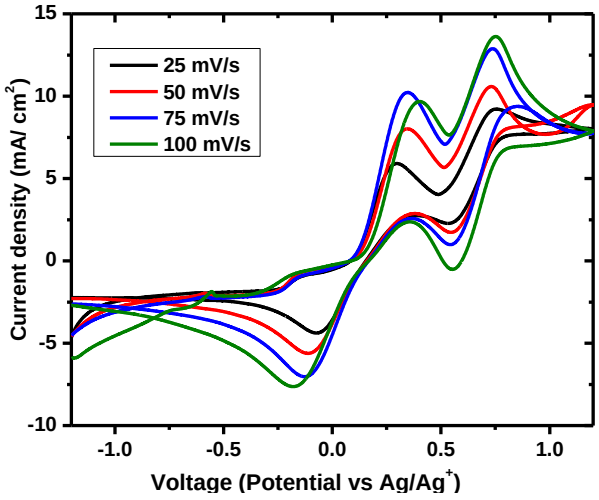


Figure 5.8: Cyclic voltammograms of Pt at increasing scan rate.

The cyclic voltammograms of CZTS/fN-MWCNTs hybrid materials at scan rates of 25, 50, 75 and 100 mV/s are shown below (**Figure 5.9**). Current density (J_c) is observed to increase with scan rate for all the samples although much higher current densities are produced for CZTS/fN-MWCNTs (0.25) and CZTS/fN-MWCNT (0.3). Improved J_c with increasing N-MWCNTs concentration implies that the incorporation of the tubular structures within the CZTS matrix improves the CZTS performance as a CE material. The CZTS/fN-MWCNTs (0.2) CE shows a very small area reduction peak relative to the other prepared composite CE materials.

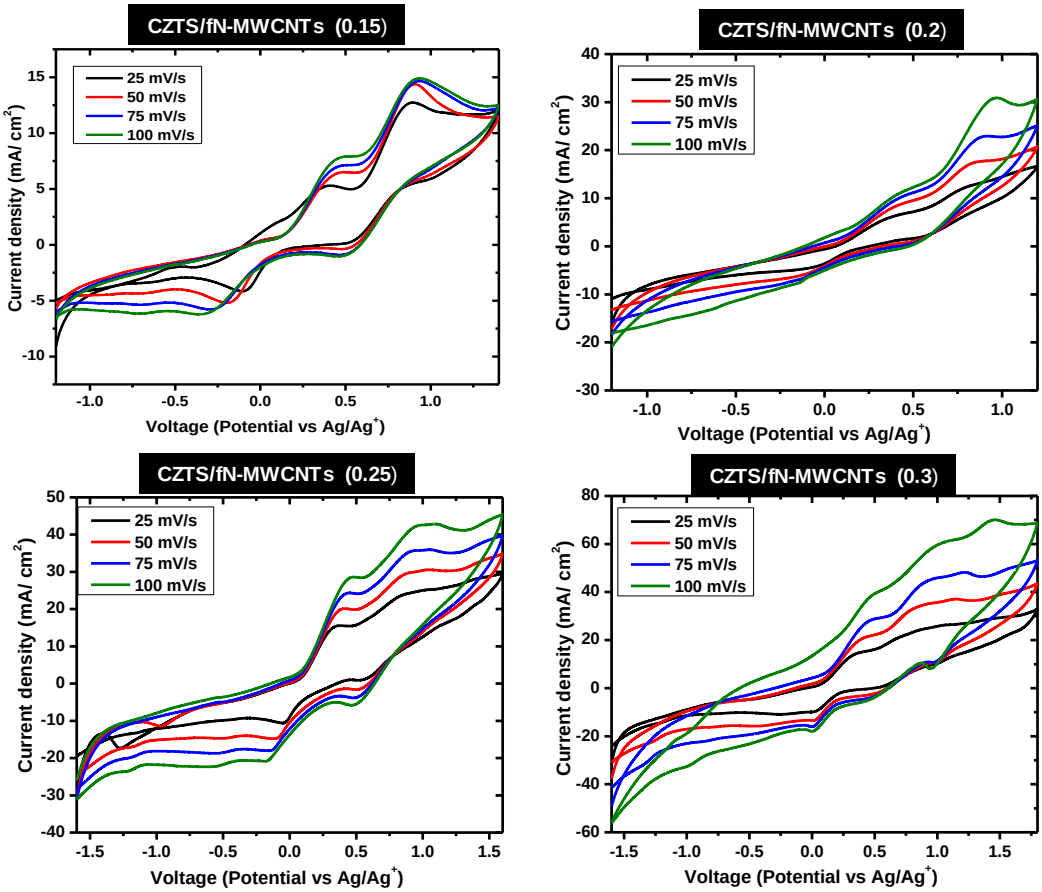


Figure 5.9: Cyclic voltammograms of CZTS/fN-MWCNTs nanocomposites at increasing scan rates.

The properties of a good CE material include, but are not limited to good chemical stability in the electrolyte, high electro-catalytic activity, low overpotential and low-cost [23].To evaluate the stability of the prepared CE materials in the I^-/I_3^- electrolyte using CV. Usually, many CV cycles are run at a chosen scan rate [24]. **Figure 5.10** below shows the stability evaluation of the composites at 100 mV/s after 30 scan cycles. The results show that the current density drastically declined after 30 cycles suggesting poor stability of the CEs. The plot of maximum reduction peak current density and the number of scans is then used to ascertain whether the CE are stable (**Figure 5.10**). It is evident from the stability study that the prepared nanocomposite materials were not stable since the current densities decline as the number of scan cycles in increased. Poor interaction of the prepared ink solution with the glassy carbon electrode could mean that after some time, the deposited composites are washed off from the electrode surface.

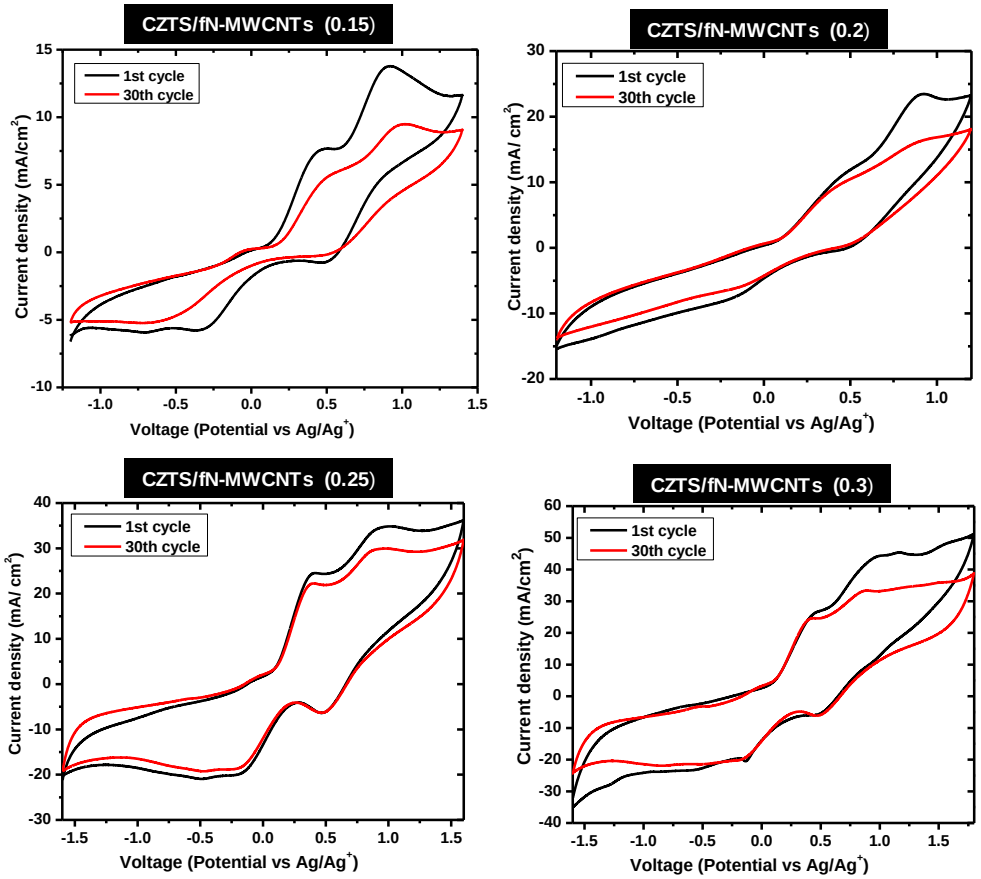


Figure 5.10: Stability evaluation of the prepared composites in iodide/triiodide-based electrolyte after 60 cycles at 100 mV/s.

It can also be deduced from the comparison of the number of scan cycles and the current density (**Figure 5.11**) that as the mass percentage of fN-MWCNTs in the nanocomposites was increased from 15 % to 30 %, the current density and therefore the catalytic activity increased. However, CZTS/fN-MWCNTs (0.25) and CZTS/fN-MWCNTs (0.3) based CE produced the highest current densities and could serve as alternative DSSC CE materials.

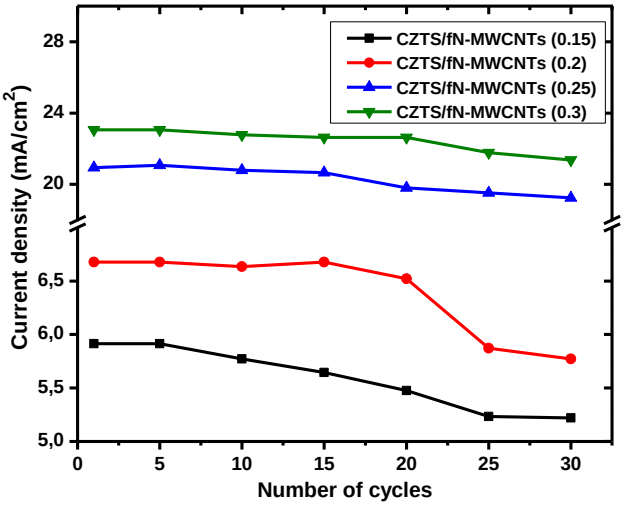


Figure 5.11: Relationship between the number of CV scans of the composites at the obtained current density.

The CV spectra obtained at 50 mV/s of the CZTS/fN-MWCNTs CE on glassy carbon electrode were compared with each other to find the best performing one (**Figure 5.12**). Increasing the concentration of N-MWCNTs from 15 to 30 w/w %in the nanocomposites showed an increase in the current density of the nanocomposite materials. The J_c values of CZTS/fN-MWCNTs (0.25) and CZTS/fN-MWCNTs (0.3) were 14.7 and 15.7 $mAcm^{-1}$ and their V_{oc} values were -0.492 V and -0.394 V, respectively (**Table 5.1**). The CZTS/fN-MWCNTs (0.3) shows both a high J_c and a small overpotential which means that of the three prepared CE materials, this is the best performing CE. It is therefore necessary to compare CZTS/fN-MWCNTs (0.3) to Pt, bare glassy carbon electrode, CZTS as well as fN-MWCNTs to establish whether the composite material outperforms its constituent materials.

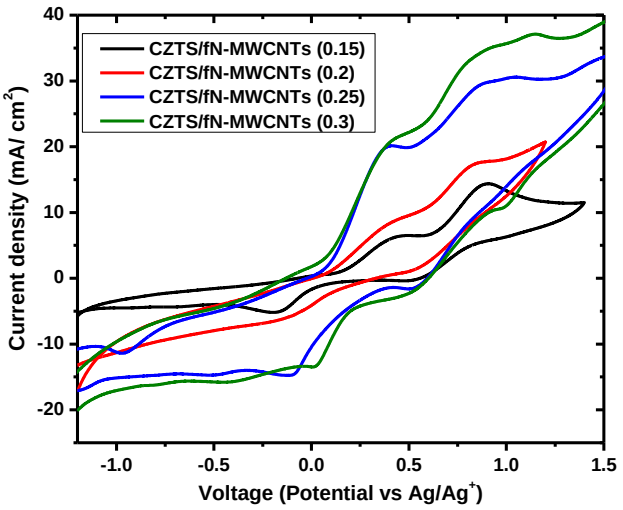


Figure 5.12: Change in reducing ability of the CZTS/fN-MWCNTs with increasing carbon nanotube concentration at 50 mV/s.

Table 5.1: Dependence of current density and open circuit voltage on the concentration of carbon nanotubes in the nanocomposites

CE	J_c/ $mAcm^{-2}$	V_{oc}/V
CZTS/fN-MWCNTs (0.15)	5.1	-0.165
CZTS/fN-MWCNTs (0.2)	6.1	-0.145
CZTS/fN-MWCNTs (0.25)	14.7	-0.492
CZTS/fN-MWCNTs (0.3)	15.7	-0.394

Comparison of the CV of the best performing composite material (CZTS/fN-MWCNTs (0.3)) to the CV spectra of the composite constituent elements was carried out and is shown in **Figure 5.13 (a)**. It is worth noting that CZTS as a working electrode in CV results in a high current density (15.2 $mAcm^{-2}$) and high reduction peak area. This implies that CZTS has a high number of catalytic sites available and a good reduction activity of the I_3^- electrolyte species. This observation is in line with Tong and co-workers' results [25] and suggests that indeed CZTS has a reduction activity and relative to fN-MWCNTs, it has a faster reduction reaction rate [26] and can therefore be applied as a CE material in dye-sensitized solar cells. However, CZTS based CE give the most negative potential, which suggests that this electrode requires the most amount of energy to reduce the electrolyte. Incorporation of 30 weight % fN-MWCNTs within the matrix of CZTS results in a more positive potential without compromising the current density (-0.394). This could be due to improved surface area and better electron mobility from the nanotubes. Generally, the catalytic activity is observed to be lowest in fN-MWCNTs, followed by CZTS and Pt, and highest in CZTS/fN-MWCNTs based CE materials. This trend was also observed in the work done by Chen H. and co-workers on CZTS/fMWCNTs CE materials for dye-sensitized solar cells [27].

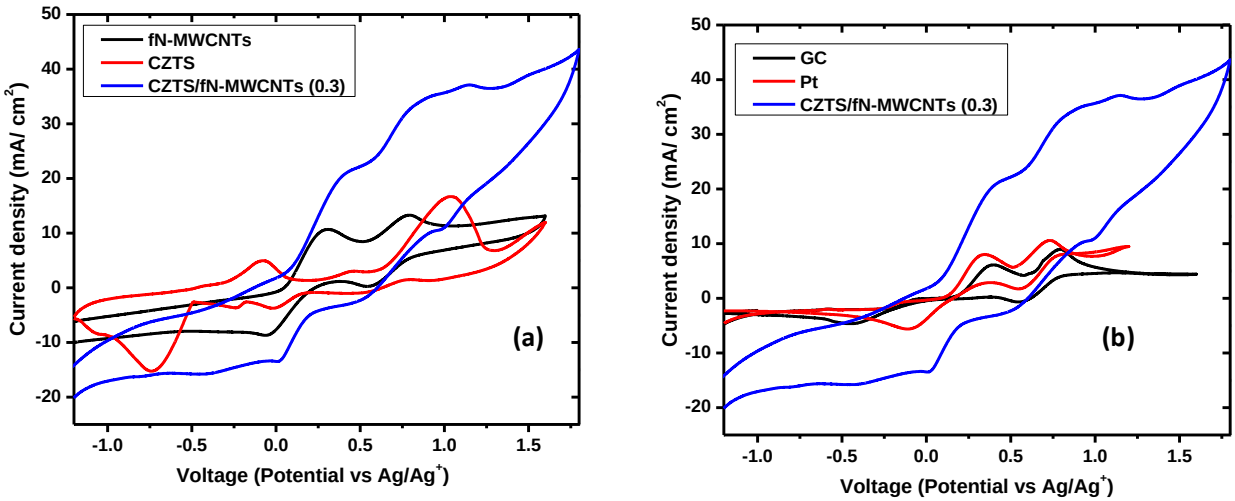


Figure 5.13: Electrochemical performance comparison of CZTS/fN-MWCNTs (0.3) with (a) CZTS and fN-MWCNTs and (b) bare-GC and Pt.

The Pt electrode exhibits the lowest open circuit voltage of -0.102 V, which indicates that Pt requires the least amount of energy to reduce the I^-/I_3^- electrolyte. **Table 5.2** shows a summary of the performance of these CE materials. CZTS/fN-MWCNTs (0.3) produced the highest reduction peak current density as compared to its constituent materials (CZTS and fN-MWCNTs), as well as the GC and Pt. The shift towards positive voltage of -0.394 from -0.728 in the CZTS suggest that combining the nanoparticles and the carbon nanotubes results in a better performing CE.

Table 5.2: Summary of electrochemical parameters of CE materials obtained from CV

CE	J_c/ mAcm^{-2}	V_{oc}/V
CZTS	15.2	-0.728
fN-MWCNTs	8.7	-0.061
Pt	5.6	-0.102
Bare-GC	4.6	-0.435
CZTS/fN-MWCNTs (0.3)	15.7	-0.394
CZTS/N-MWCNTs	4.1	-0.255

N.B: CZTS/N-MWCNTs CV conditions were not the same as for the other CE materials obtained from the work by Chen and co-workers [27].

5.3.4 Composite charge transmission model

The CE material as shown in **Figure 5.14** constitutes a conducting surface (glassy carbon) upon which the CZTS/N-MWCNTs nanocomposite is deposited, submerged in an electrolyte solution (I^-/I_3^-). During cyclic voltammetry, electrons travel through the glassy carbon and the nanocomposite. On the electrolyte and composite material interface, the electrons reduce I^- to I_3^-. CZTS catalyses the reduction reaction [28] whereas the N-MWCNTs are highly conductive [29]. Three possible electron transport routes in the nanocomposite can be proposed. Firstly, the electron can travel from the contact surface to the catalytic sites on CZTS where upon the reduction reaction occurs. The electron movement via this route is slow because CZTS is a semi-conductor. Secondly, the electron can move through the CZTS nanoparticles and laterally through the nanotubes. Lastly, the electrons can be shuttled through the core of the nanotubes to the CZTS. The two latter processes occur faster since the nanotubes are better electron conductors. Nitrogen doping of the nanotubes, bringing about defects on the tubes could also mean a faster electron mobility through the tubes to the CZTS as they manoeuvre through these defects. As such, a higher current density is observed for CZTS/N-MWCNTs composite CE as opposed to that of CZTS and N-MWCNTs CEs.

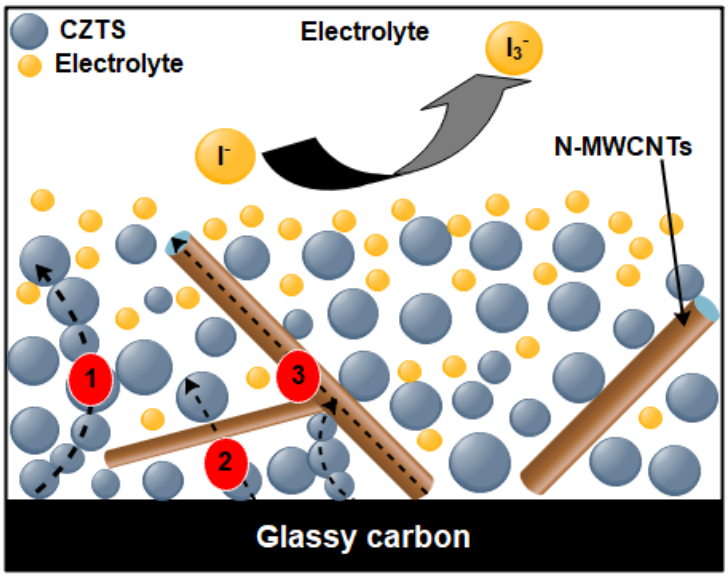


Figure 5.14: A schematic diagram depicting the possible electron transport route in the CZTS/N-MWCNTs nanocomposite CE [30].

5.4 Conclusions

The TEM images and the Raman spectra of the prepared CZTS/fN-MWCNTs hybrid systems demonstrated successful preparation of the nanocomposite materials. A nanocomposite combines the individual properties of the elements it comprises of. For this study, the

incorporation of the N-MWCNTs in the CZTS matrix was aimed at improving the surface area and the electron transport properties of CZTS. Generally, 70 w/w % CZTS and 30 w/w % fN-MWCNTs (CZTS/fN-MWCNTs (0.3)) produced a high current density, which implies that it is reasonably electro-catalytic compared to CZTS and fN-MWCNTs CE as well as Pt. As such, it can be concluded that of the prepared composites, CZTS/fN-MWCNTs (0.3) is a promising DSSC CE material and should therefore be evaluated further in a DSSC set-up.

5.5 References

[1] U. Schubert, N. Hiising, and A. Lorenz, "Hybrid inorganic-organic materials by sol-gel processing of organofunctional metal alkoxides," *Chemistry of Materials*, vol. 7, no. 11, pp. 2010-2027, 1995.

[2] D. Eder, "Carbon nanotube-inorganic hybrids," *Chemical Reviews*, vol. 110, pp. 1348-1385, 2010.

[3] C. Sanchez, B. Julián, P. Belleville, and M. Popall, "Applications of hybrid organic-inorganic nanocomposites," *Journal of Materials Chemistry*, vol. 15, no. 35-36, pp. 3559-3592, 2005.

[4] P. Judeinstein and C. Sanchez, "Hybrid organic-inorganic materials: A land of multidisciplinarity," *Journal of Materials Chemistry*, vol. 6, no. 4, pp. 511-525, 1996.

[5] J. M. Bell, R. G. S. Goh, E. R. Waclawik, M. Giulianini, and N. Motta, "Polymer-carbon nanotube composites: Basic science and applications," *Materials Forum*, vol. 32, pp. 144-152, 2007.

[6] G. Yue, J. Wu, J. Lin, Y. Xiao, S. Tai, J. Lin, M. Huang and Z. Lan, "A counter electrode of multi-wall carbon nanotubes decorated with tungsten sulfide used in dye-sensitized solar cells," *Carbon*, vol. 55, pp. 1-9, 2013.

[7] C. V. V. M. Gopi, S. Ravi, S. S. Rao, A. E. Reddy, and H. Kim, "Carbon nanotube/metal-sulfide composite flexible electrodes for high-performance quantum dot-sensitized solar cells and supercapacitors," Nature Publishing Group, 2017.

[8] A. J. Haider, M. R. Mohammed, E. A. J. Al-Mulla, and D. S. Ahmed, "Synthesis of silver nanoparticle decorated carbon nanotubes and its antimicrobial activity against growth of bacteria," *Rendiconti Lincei*, vol. 25, no. 3, pp. 403-407, 2014.

[9] J. Y. Lin, C. H. Lien, and S. W. Chou, "Multi-wall carbon nanotube counter electrodes for dye-sensitized solar cells prepared by electrophoretic deposition," *Journal of Solid State Electrochemistry*, vol. 16, no. 4, pp. 1415-1421, 2012.

[10] X. Fang, T. Ma, G. Guan, M. Akiyama, T. Kida, and E. Abe, "Effect of the thickness of

the Pt film coated on a counter electrode on the performance of a dye-sensitized solar cell," *Journal of Electroanalytical Chemistry*, vol. 570, no. 2, pp. 257-263, 2004.

[11] G. A. Mabbott, "An introduction to cyclic voltammetry," *Journal of Chemical Education*, vol. 60, no. 9, pp. 697-702, 1983.

[12] G. Yue, X. Zhang, L. Wang, F. Tan, J. Wu, Q. Jiang, J. Lin, M. Huang and Z. Lan, "Highly efficient and stable dye-sensitized solar cells based on nanographite/polypyrrole counter electrode," *Electrochimica Acta*, vol. 129, pp. 229-236, 2014.

[13] G. Yue, X. Ma, W. Zhang, F. Li, J. Wu, and G. Li, "A highly efficient flexible dye-sensitized solar cell based on nickel sulfide/platinum/titanium counter electrode," *Nanoscale Research Letters*, vol. 10, no. 1, pp. 1-9, 2015.

[14] S. S. Nemala, K. Mokurala, P. Bhargava, and S. Mallick, "Cu_2ZnSnS_4/CNT composites as Pt free counter electrodes for dye sensitized solar cells with improved efficiency," *Materials Today: Proceedings*, vol. 3, no. 6, pp. 1808-1814, 2016.

[15] S. Das, K. Sa, I. Alam, P. C. Mahakul, J. Raiguru, B. V. R. S. Subramanyam and P. Mahanandia, "Synthesis and characterizations of Cu_2ZnSnS_4 nanoparticles/carbon nanotube composite as an efficient absorber material for solar cell application," *AIP Conference Proceedings*, vol. 1961, pp. 020006-1-020006-6, 2018.

[16] S. Das, K. Sa, I. Alam and P. Mahanandia, "Enhancement of photocurrent in Cu_2ZnSnS_4 quantum dot-anchored multi-walled carbon nanotube for solar cell application," *Journal of Materials Science*, vol. 54, pp. 8542-8555, 2019.

[17] E. N. Nxumalo, V. O. Nyamari and N. J. Coville, "CVD synthesis of nitrogen doped carbon nanotubes using ferrocene/aniline mixtures," *Journal of Organometallic Chemistry*, vol. 693, pp. 2942-2948, 2008.

[18] X. X. Zhang, Z. Q. Li, G. H. Wen, K. K. Fung, J. Chen and Y. Li, "Microstructure and growth of bamboo-shaped carbon nanotubes," *Chemical Physics Letters*, vol. 333, pp. 509-514, 2001.

[19] R. Ahmad, M. Distaso, and W. Peukert, "Facile synthesis and post-processing of eco-friendly, highly conductive copper zinc tin sulphide nanoparticles," *Journal of Nanoparticle Research*, vol. 15, pp. 1-16, 2013.

[20] Q. Zhao and H. D. Wagner, "Raman spectroscopy of carbon-nanotube-based composites," *Philosophical Transactions of the Royal Society A: Mathematical, Physical and Engineering Sciences*, vol. 362, pp. 2407-2424, 2004.

[21] E. T. Thostenson, Z. Ren and T. Chou, "Advances in the science and technology of

carbon nanotubes and their composites: A review," *Composites Science and Technology*, vol. 61, pp. 1899-1912, 2001.

[22] K. A. Wapasnick, B. A. Smith, J. L. Bitter and D. Howard Fairbrother, " Chemical and structural characterization od carbon nanotube surfaces," *Analytical and Biological Chemistry*, vol. 3, no. 396, pp. 1003-1004, 2010.

[23] G. Yue, F. Li, F. Tan, G. Li, C. Chen, and J. Wu, "Nickel sulfide films with significantly enhanced electrochemical performance induced by self-assembly of 4-aminothiophenol and their application in dye-sensitized solar cells," *RSC Advances*, vol. 4, no. 109, pp. 64068-64074, 2014.

[24] G. Yue, X. Ma, W. Zhang, F. Li, J. Wu and G. Li, "A highly efficient flexible dye-sensitized solar cell based on nickel sulfide/platinum/titanium counter electrode,", *Nanoscale Research Letters*, vol. 10, no. 1, pp. 1-9, 2015.

[25] Z. Tong, Z. Su, F. Liu, L. Jiang, Y. Lai, J. Li, and Y. Liu,"In situ prepared Cu_2ZnSnS_4 ultrathin film counter electrode in dye-sensitized solar cells," *Materials Letters*, vol. 121, pp. 241-243, 2014.

[26] L. Zhu, Y. H. Qiang, Y. L. Zhao, and X. Q. Gu, "Double junction photoelectrochemical solar cells based on Cu_2ZnSnS_4/$Cu_2ZnSnSe_4$ thin film as composite photocathode," *Applied Surface Science*, vol. 292, pp. 55-62, 2014.

[27] H. Chen, J. Wang, C. Jia, J. Mou, and L. Zhu, "Highly efficient dye-sensitized solar cell with a novel nanohybrid film of Cu_2ZnSnS_4-MWCNTs as counter electrode," *Applied Surface Science*, vol. 422, pp. 591-596, 2017.

[28] P. Dai, G. Zhang, Y. Chen, H. Jiang, Z. Feng, Z. Lin and J. Zhan, "Porous copper zinc tin sulfide thin film as photocathode for double junction photoelectrochemical solar cells," *Chemical Communications*, vol. 48, no. 24, pp. 3006-3008, 2012.

[29] J. M. Nudent, K. V. S. Santhanam, A. Rubio and P. M. Ajayan, "Fast electron transfer kinetics of multiwalled carbon nanotube microbundle electrodes, " *Nano Letters*, vol. 1, pp. 87-91, 2001.

[30] X. Zeng, D. Xiong, W. Zhang, L. Ming, Z. Xu, Z. Huang, M. Wang, W. Chen and Y. Cheng, "Spray deposition of water-soluble multiwall carbon nanotube and $Cu_2ZnSnSe_4$ nanoparticle composites as highly efficient counter electrodes in a quantum dot-sensitized solar cell system," *Nanoscale*, vol. 5, no. 15, pp. 6992-6998, 2013.

Chapter 6 : Conclusions and future work

In this research work, chemical vapor deposition method was utilised to prepare N-MWCNTs using bimetallic Fe-Co/$CaCO_3$ catalyst at 800 °C for 1 hour using acetylene and acetonitrile as carbon and nitrogen sources, respectively. The nanotubes obtained had open ends, were entangled and had diameter size distribution of 40 ± 15 nm. Acid washing the nanotubes in 98% H_2SO_4/55% HNO_3 removed most of the catalyst residue, resulted in less agglomerated nanotubes and introduced carboxylic acid functional groups on the walls and tips of the N-MWCNTs. The nitrogen atom percentage composition of the N-MWCNTs was found to be 3.8 %, of which the largest portion of 1.7 % was due to quaternary nitrogen. Both the acid functionalities and nitrogen induced flaws within the graphitic structure on the nanotubes were assumed to take part in the interaction of the tubes with OLA capped CZTS when forming nanocomposites. Structural modification of the as-synthesized poly-dispersed OLA capped CZTS was carried out by digestive ripening in excess ligand. Ripening for two hours gave the best results. Ligand exchange of the OLA ligand for pyridine, EDT and MPA were carried out. MPA had no effect on the morphology and the crystallographic structure of CZTS while EDT and pyridine resulted in poor quality nanoparticles with impurities. As a result, ligand exchange was ruled out and OLA capped ripened nanoparticles were used for composite formation.

The nanocomposites were prepared by sonicating the OLA capped CZTS and fN-MWCNTs in DMF for 1 hour. This procedure resulted in composites that had uneven distribution of the CZTS nanoparticles on the walls of the nanotubes. One of the major challenges in this research work was finding an appropriate solvent to disperse the nanotubes in to prepare the nanocomposite ink for fabrication on FTO glass. Most of the employed solvents produced FTO based CEs that peel off and thus we opted to drop cast the inks on glassy carbon electrode. The challenge with using this route is because carbon materials have reducing activity towards the I^-/I_3^- as can be seen from **Figure 5.11 (b)** (**Chapter 5**). It therefore becomes difficult to remove the effect of the glassy carbon on the reduction activity of the nanocomposites. Using FTO to fabricate the CEs is still the best option; however, a lot of time needs to be invested in finding a suitable solvent for the CZTS and fN-MWCNTs hybrid materials. A solvent study can be carried out to find the best solution to dissolve the CZTS/fN-MWCNTs hybrids. Additionally, binding agents employed in the ink can be optimized to find the most suitable one for these hybrid materials. Nonetheless, the reduction

peak current densities increased drastically with increasing percentage composition of the N-MWCNTs in the nanocomposites from 15 w/w % to 30 w/w%. Also, the open circuit voltage shifted to the positive side as more of the nanotubes were used. Therefore, using fN-MWCNTs does improve the electro-catalytic activity of CZTS nanoparticles and the CZTS/fN-MWCNTs (0.3) has potential to be employed as an alternative counter electrode material to Pt in DSSCs. For future work, a DSSC using CZTS/fN-MWCNTs (0.3) CE can be constructed and analysed using EIS to obtain the resistance of the cell. Additionally, the power conversion efficiency of the cell can be determined by using a solar simulator (AM 1.5 G) which gives the *I-V* curve from which the max power can be determined.

Appendix

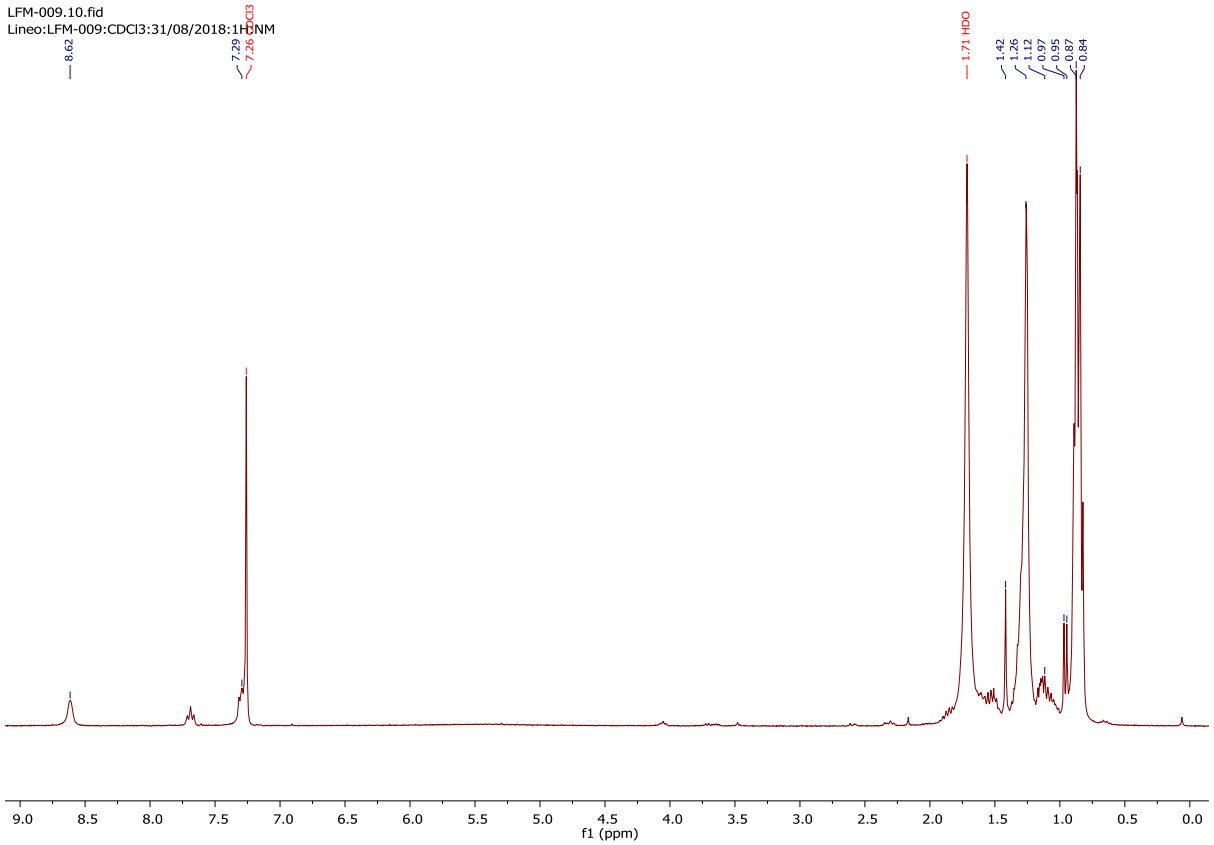


Figure A4.1: Full ^{1}H NMR spectrum of pyridine capped CZTS.